Dynamic loading of journal bearings

T. E. Brown

Dynamic Loading of Journal Bearings

by

T.E. Brown

Thesis submitted for the degree
of Doctor of Philosophy
in the University of Durham
1976

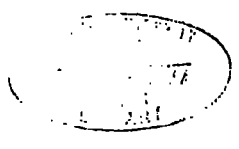

Acknowledgements

The research described in this dissertation was carried out at the Department of Engineering Science, Durham University between October 1973 and September 1976. The author would like to thank Professor Harry Marsh, who supervised this project, for his enthusiasm and for the valuable advice which he has given.

The research project has been financed by the Science Research Council, to whom the author is extremely grateful.

The author would like to express his appreciation for the assistance given by the workshop staff, who manufactured the experimental apparatus, and also to Dr. V.G. Endean for his help with the electronics.

Except where stated otherwise this dissertation describes the original work of the author, and no part of it has been submitted to any other university.

September 1976 T.E. Brown.

CONTENTS

Page No.

Summary

The prediction of the performance of a dynamically loaded journal bearing is usually based on the assumption that the lubricant film behaves similarly to that in a steadily loaded bearing. Experimental evidence has been collected which questions this assumption. White (2) carried out work on a squeeze film bearing which suggested that the present theoretical approach to the prediction of the load carrying capacity of dynamically loaded bearings may be incorrect, and that the load carrying capacity of such bearings may be over estimated by a factor of at least four.

This dissertation describes an investigation into the load carrying capacity of a dynamically loaded bearing comprising a vertical rotating shaft supporting a non-rotating bearing which was subjected to a constant rotating load.

Reynolds' equation is derived for the bearing subjected to a constant rotating load, assuming the oil film to be similar to that in a steadily loaded bearing. The experimental results are compared with the theoretical predictions, which were obtained using conventional boundary conditions. In all cases the experimental results showed good agreement with the theoretical predictions.

Nomenclature

c	radial clearance.
$\frac{D}{Dt}$	Stokesian operator. $\frac{\partial}{\partial t} + u\frac{\partial}{\partial x} + v\frac{\partial}{\partial y} + w\frac{\partial}{\partial z}$
e	eccentricity.
f	non-dimensional film force, $\left\|\frac{Wc^2}{6\mu U_{eff} R^2 L}\right\|$
Fr	radial component of film force.
Fs	tangential component of film force.
h	local clearance, $c(1+\varepsilon\cos\phi_r)$.
H	non-dimensional local clearance, $\frac{h}{c}$
L	bearing length.
M	variable used in numerical analysis, $\bar{p}H^{3/2}$.
N_L	load speed, r.p.m.
Ns	shaft speed, r.p.m.
p	gauge pressure, P - Pa.
p_{cav}	cavitation pressure.
p_{end}	supply pressure.
$\bar{p}$	non-dimensional pressure, $\frac{pc^2}{6\mu U_{eff} R}$
P	absolute pressure.
Pa	atmospheric pressure.
R	bearing radius.
t	time.
u, v, w	x, y and z components of velocity.
U_1	surface velocity of shaft.
U_2	surface velocity of bearing.
U_{eff}	effective velocity.
W	bearing load, film force.

$\bar{W}$	non-dimensional film force used by White, $\frac{Wc^2}{\mu R^3 L \dot{\theta}}$
x, y, z	co-ordinate system.
x_r, y, z	cc-ordinate system for relative (rotating) co-ordinates.
X, Y, Z	external body forces in x, y, z directions.
$\bar{z}$	non-dimensional co-ordinate, $\frac{z}{L}$.
α	ratio, $\frac{R}{L}$.
Δt	time increment.
ε	eccentricity ratio, $\frac{e}{c}$.
θ	angle between fixed datum and line of centres.
$\dot{\theta}$	angular velocity of load, $\frac{d\theta}{dt}$
μ	absolute viscosity.
ρ	density.
ϕ	angular co-ordinate in fixed co-ordinate system.
ϕr	angular co-ordinate in relative (rotating) co-ordinate system.
ω_1	angular velocity of shaft.
ω_2	angular velocity of bearing.
ω_{eff}	effective angular velocity, $\omega_1 + \omega_2 - 2\dot{\theta}$.

CHAPTER 1

Introduction

There has been a great deal of research into the steadily loaded bearing, in which the shaft alone rotates. Extensive experimental work has been carried out on the performance of such bearings, and several authors have photographed the lubricant film. The photographs have shown that the oil film ruptures in the low pressure region of the bearing to form long cavities separated by oil filaments. The research has concentrated on the boundary conditions at film breakdown and reformation, which determine the region of film rupture, the cavitated region. The performance of such a system can now be predicted accurately.

By comparison very little work has been reported on the performance of dynamically loaded bearings. The majority of bearings in service come under the general description of dynamically loaded, yet there is very little information on the design and operation of these bearings. The prediction of the performance of dynamically loaded journal bearings is usually based on the assumption that the oil film has a similar behaviour to that in a steadily loaded bearing. However, experimental work has been carried out which indicates that this assumption may not be valid.

Some early experiments were carried out by Cole and Hughes (1), who photographed the cavitation region in a glass bearing subjected to a constant rotating load.

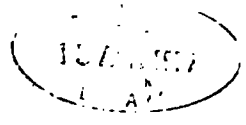

The visual techniques used led them to the conclusion that the cavitation region moved around the bearing synchronously with the load and was similar to that observed in a steadily loaded bearing. This suggested that the behaviour of a dynamically loaded bearing may be predicted by applying conventional, steadily loaded boundary conditions. Quantitative results were not taken in this investigation.

More recent work by White (2) with a squeeze film bearing cast doubt on Cole and Hughes' conclusions. White's apparatus was a rigid, vertical, non-rotating shaft supporting a bearing which was subjected to a constant rotating load. When operating at low eccentricities the load carrying capacity of the bearing was in good agreement with conventional, theoretical predictions, but at high eccentricity ratios the load carrying capacity was only between six and twenty-five per cent of the predicted value. White also photographed the cavitation region and found that it exhibited a very different appearance from that in a steadily loaded bearing.

The results of the investigations carried out by Cole and Hughes (1) and White (2) may appear contradictory, but when the two sets of photographic evidence are compared great similarity can be seen in the state of the oil film.

If White's quantitative results are typical of the dynamically loaded bearing it is clear that the operation of an oil lubricated bearing under dynamic loading is not

fully understood. If the load capacity can drop to between six and twenty-five per cent of the predicted value there is need to re-examine the method of design for dynamically loaded bearings.

The simplest form of dynamic loading is the constant rotating load, as investigated by Cole and Hughes (1) and White (2). Before complex loading regimes, such as those encountered in internal combustion engines, can be tackled with confidence, it is necessary to understand the simple loading forms. This work will detail the design of an experimental rig in which a vertical, rotating shaft supports a non-rotating bearing which may be subjected to a constant, rotating load. The performance of the bearing will be compared with conventional theoretical predictions.

CHAPTER 2

Previous Work

Harrison (3) in 1919 was probably the first person to discuss dynamic loading and bearing instability. Reynolds' equation was modified for the case of an infinitely long bearing supporting a steady load together with a small dynamic load. Hummel (26) examined the onset of whirl in a rigid shaft by considering the stability of the journal equilibrium position. Stability was tested by considering the equations of motion for small displacements about the steadily loaded equilibrium point. This approach was not a true dynamic analysis of the system, but was a 'quasi-static' method.

In 1937 Swift (4) solved Reynolds' equation for an infinitely long bearing to produce analytical expressions for the response of the bearing to simple forms of dynamic loading. Burwell (5), (6) and (7) repeated and extended the work of Swift. The first two papers (5) and (6) deal with the infinitely long and infinitely short bearing respectively and indicate the numerical calculation of the response of a bearing to dynamic loading. The second paper also describes the application of the theory to the problem of an engine bearing. The third paper (7) considers the short bearing subjected to various simple cyclic loading forms and serves as an illustration of the techniques used in (6).

The papers mentioned previously did not take account of the effect of cavitation within the lubricant film.

A complete film had normally been assumed, possibly on the grounds that it was difficult to envisage cyclic rupture and reformation of the oil film. In steadily loaded bearings the cavitation region had normally been assumed to coincide with the region of predicted negative pressures. A representation of the cavitation region had been achieved by assuming that negative gauge pressures could not occur without causing film rupture. The cavitation region was modelled by assuming that pressures below atmospheric pressure could not occur within a bearing, and all predicted negative pressures were set to a constant value, normally atmospheric pressure.

In 1948 Ott (8) included the effect of cavitation in an analysis of a dynamically loaded, infinitely long bearing by setting predicted negative pressures to atmospheric, as in the steadily loaded bearing. The predicted lubricant film, therefore, spread over only half of the circumference of the bearing. Journal loci were found for fluctuating loads of small amplitude. The analysis was valid for small eccentricity ratios only.

Cavitation within a bearing produces a two phase region of air and lubricant. Reynolds' equation is a statement of the continuity of flow within the bearing and is violated in the region of cavitation. Previously the cavitation region had been modelled by assuming that the film could not sustain negative gauge pressures. The predicted negative pressures were set to atmospheric pressure. The region of cavitation also imposes boundary

conditions on the region of complete lubricant film. These boundary conditions had not been extensively investigated until Jakobsson and Floberg (10) carried out experimental and theoretical work on the cavitation region within a steadily loaded bearing. They showed that for such a bearing the pressure gradient at the oil film breakdown boundary was zero, and was finite at the reformation boundary. These boundary conditions are now widely accepted as a first approximation, and are used together with the assumption of constant pressure within the cavitation region to predict the performance of the steadily loaded bearing.

Hahn (9) carried out a numerical solution of the full Reynolds' equation for dynamic loading. Reynolds equation was solved for a rotating shaft alone, and also for motion of the shaft centre alone. Any proportion of the two pressure distributions could be added, and cavitation could be included by setting the predicted negative pressures to atmospheric. Hahn showed how these results could be used to obtain the polar load diagram from a given journal locus, and conversely the locus form from a given load diagram.

Horsnell and McCallion (11) applied the Jakobsson and Floberg boundary conditions for a steadily loaded bearing to obtain a relaxation solution for a finite, dynamically loaded bearing.

The papers described above have been concerned with the theoretical analysis of a dynamically loaded journal bearing. Only a small amount of experimental work has

been carried out, however, perhaps due to the complexities of the apparatus required.

Stone and Underwood (12) described the theory for a bearing subjected to a constant, rotating load. The performance of such a bearing was said to vary with an effective speed, Ns - $2N_L$, where Ns was the shaft speed and N_L the load speed. The effective speed could be substituted into Reynolds' equation to predict the performance of the bearing.

Stone and Underwood also carried out some experimental work on an apparatus comprising a rotating shaft subjected to a constant rotating load, which was supported within a stationary bearing. They observed the effect of the value of the effective velocity on the load carrying capacity of the bearing by measuring the change in eccentricity ratio caused by varying the load speed, N_L, while maintaining a constant shaft speed Ns, and a constant load. The load speed was increased from rest in the same direction as the shaft. As the effective velocity decreased the eccentricity ratio increased, showing a fall in load carrying capacity. When the effective velocity was zero, the eccentricity ratio was 1.0, showing the complete loss of load carrying capacity predicted by Reynolds' equation. Further increase in load speed caused the effective velocity to go negative, i.e. an increase in $|Ns - 2N_L|$, and the load capacity was restored as the eccentricity ratio decreased. The work was mainly qualitative and a detailed description of the performance of the bearing was not given. Measurement of load angle

did not come within the scope of their work.

Simons (13) carried out work on an apparatus which investigated the performance of a bearing which supported a shaft which could be subjected to a constant rotating load. It was found that with a constant rotating load the shaft described a circular orbit. An investigation similar to that undertaken by Stone and Underwood (12) was carried out. Simons' work confirmed that of Stone and Underwood and showed that when the load speed was one half of the shaft speed a dramatic loss of load carrying capacity occurred. Again detailed work on the load capacity of the bearing was not carried out, and the load angle was not investigated.

Shawki and Freeman (14) developed an apparatus to investigate the motion of the journal centre of a bearing subjected to unidirectional, sinusoidal loading, and showed that at a cyclic frequency of one half of the shaft speed the load carrying capacity of the bearing disappeared.

Cole and Hughes (1) were interested in determining the form and extent of the cavitation region in a dynamically loaded journal bearing. The theoretical analyses of the dynamically loaded, complete journal bearing had normally assumed a long bearing and a 360° oil film. Cole and Hughes carried out a visual study of the oil film in a system composed of a shaft rotating inside a glass bearing, which was subjected to a constant rotating load. The cavitation region was photographed and it was concluded that the film rupture in a dynamically loaded bearing was similar to that in a

steadily loaded bearing, and rotated synchronously with the load as the low pressure region travelled around the bearing. At any point in the lubricant film the lubricant ruptured and reformed at the frequency of the rotating load. A more detailed description of their results is given in Chapter 4.

White (2) carried out experimental work on a squeeze film bearing supporting a constant rotating load. White's experiments are the starting point for the work described in this thesis and his investigation will be detailed in the following section.

2.1. The results of D.C. White (2)

White constructed an apparatus for investigating squeeze film bearings, as used in aero engines. The apparatus comprised a vertical, rigid, non-rotating shaft supporting a non-rotating bearing which could be subjected to a constant rotating load. The bearings used varied in length between 12.7 mm and 38.1 mm to allow the investigation of bearings with length to diameter ratios of 0.125 to 0.375. The bearings were loaded by two hydraulic exciters mounted at right angles, and producing equal, sinusoidally varying loads to give a resultant which was a constant rotating load. The frequency of the applied load was between 5Hz and 50Hz.

Figures 2.1 to 2.3 show typical examples of White's results compared with the conventionally predicted performance of the bearing, based on the equivalent velocity method described by Stone and Underwood, and

generally accepted as applicable to a bearing subjected to a constant rotating load. The performance is shown as a graph of non-dimensional film force W against eccentricity ratios, where

$$W = \frac{Wc^2}{\mu R^3 L \dot{\theta}}$$

W being the bearing load and $\dot{\theta}$ the angular velocity of the load.

In each example shown the behaviour of the bearing is closely predicted by theory up to an eccentricity ratio of 0.3, but at higher eccentricity ratios the film force is far less than that predicted by conventional theory. Figure 2.1 shows results taken for a length to diameter ratio of 0.125, and it can be seen that at high eccentricity ratios the results follow a line which corresponds to one quarter of the predicted load carrying capacity of the bearing. Figure 2.2 shows the results taken for a length to diameter ratios of 0.375 which shows experimental results approximately one eighth of the predicted values. Figure 2.3 show results taken for a length to diameter ratio of 0.375 which are approximately one fifteenth of the predicted values at high eccentricity ratios.

White measured the load angle in his experiments and surprisingly found good agreement with theory. A perspex bearing was then substituted for the test bearing and the cavitation region was filmed with a high speed ciné camera. White reported the existence of a cavitation region very different from that seen in a

steadily loaded bearing, and it was felt that the change in cavitation may have been responsible for the dramatic loss in load carrying capacity which had been observed. The observations of the cavitation region are described at length in Chapter 4.

If White's results are typical for a bearing subjected to a constant rotating load, it is clear that the conventional prediction of the load carrying capacity of such bearings is grossly in error. The validity of White's results must be confirmed, and a valuable extension of the work would be to consider a bearing system subjected to a constant rotating load, in which the shaft may also rotate.

CHAPTER 3

Conventional Theory

In 1919 Harrison (3) extended Reynolds' equation to include the case of dynamic loading. Reynolds' equation will be derived here for a journal bearing supplied with a compressible lubricant and subjected to dynamic loading. The resulting equation will then be modified to give the incompressible form of Reynolds' equation for a bearing subjected to a constant rotating load.

3.1. Reynolds' equation in a fixed co-ordinate system

Reynolds' equation will first be derived for a co-ordinate system which is fixed in space.

If a co-ordinate system consisting of three orthogonal axes x, y, z is considered, and the velocities in the three directions x, y, z are u, v, w respectively, then the Navier-Stokes' equations for a compressible fluid are given by

$$\rho\frac{Du}{Dt} = X - \frac{\partial P}{\partial x} - \frac{2}{3}\frac{\partial}{\partial x}\left[\mu\left(\frac{\partial u}{\partial x}+\frac{\partial v}{\partial y}+\frac{\partial w}{\partial z}\right)\right] + 2\frac{\partial}{\partial x}\left[\mu\frac{\partial u}{\partial x}\right] + \frac{\partial}{\partial y}\left[\mu\left(\frac{\partial u}{\partial y}+\frac{\partial v}{\partial x}\right)\right] + \frac{\partial}{\partial z}\left[\mu\left(\frac{\partial u}{\partial z}+\frac{\partial w}{\partial x}\right)\right] \tag{3.1}$$

$$\rho\frac{Dv}{Dt} = Y - \frac{\partial P}{\partial y} - \frac{2}{3}\frac{\partial}{\partial y}\left[\mu\left(\frac{\partial u}{\partial x}+\frac{\partial v}{\partial y}+\frac{\partial w}{\partial z}\right)\right] + 2\frac{\partial}{\partial y}\left[\mu\frac{\partial v}{\partial y}\right] + \frac{\partial}{\partial z}\left[\mu\left(\frac{\partial v}{\partial x}+\frac{\partial w}{\partial y}\right)\right] + \frac{\partial}{\partial x}\left[\mu\left(\frac{\partial v}{\partial x}+\frac{\partial u}{\partial y}\right)\right]$$

$$\rho\frac{Dw}{Dt} = Z - \frac{\partial P}{\partial z} - \frac{2}{3}\frac{\partial}{\partial z}\left[\mu\left(\frac{\partial u}{\partial x} + \frac{\partial v}{\partial y} + \frac{\partial w}{\partial z}\right)\right] + 2\frac{\partial}{\partial z}\left[\mu\frac{\partial w}{\partial z}\right]$$
$$+ \frac{\partial}{\partial x}\left[\mu\left(\frac{\partial w}{\partial x} + \frac{\partial u}{\partial z}\right)\right] + \frac{\partial}{\partial y}\left[\mu\left(\frac{\partial w}{\partial y} + \frac{\partial v}{\partial z}\right)\right]$$

where X, Y, Z are the x, y, z components of the external forces. These equations are too complex to solve for the problem of bearing lubrication and may be simplified by employing various assumptions.

The flow within the bearing is assumed to be fully laminar, and if the external body forces are small compared to the viscous shearing forces, equation 3.1 reduces to

$$\frac{\partial P}{\partial x} = -\frac{2}{3}\frac{\partial}{\partial x}\left[\mu\left(\frac{\partial u}{\partial x} + \frac{\partial v}{\partial y} + \frac{\partial w}{\partial z}\right)\right] + 2\frac{\partial}{\partial x}\left[\mu\frac{\partial u}{\partial x}\right]$$
$$+ \frac{\partial}{\partial y}\left[\mu\left(\frac{\partial u}{\partial y} + \frac{\partial v}{\partial x}\right)\right] + \frac{\partial}{\partial z}\left[\mu\left(\frac{\partial u}{\partial z} + \frac{\partial w}{\partial x}\right)\right]$$
$$\frac{\partial P}{\partial y} = -\frac{2}{3}\frac{\partial}{\partial y}\left[\mu\left(\frac{\partial u}{\partial x} + \frac{\partial v}{\partial y} + \frac{\partial w}{\partial z}\right)\right] + 2\frac{\partial}{\partial y}\left[\mu\frac{\partial v}{\partial y}\right] \qquad (3.2)$$
$$+ \frac{\partial}{\partial z}\left[\mu\left(\frac{\partial v}{\partial z} + \frac{\partial w}{\partial y}\right)\right] + \frac{\partial}{\partial x}\left[\mu\left(\frac{\partial v}{\partial x} + \frac{\partial u}{\partial y}\right)\right]$$
$$\frac{\partial P}{\partial z} = -\frac{2}{3}\frac{\partial}{\partial z}\left[\mu\left(\frac{\partial u}{\partial x} + \frac{\partial v}{\partial y} + \frac{\partial w}{\partial z}\right)\right] + 2\frac{\partial}{\partial z}\left[\mu\frac{\partial w}{\partial z}\right]$$
$$+ \frac{\partial}{\partial x}\left[\mu\left(\frac{\partial w}{\partial x} + \frac{\partial u}{\partial z}\right)\right] + \frac{\partial}{\partial y}\left[\mu\left(\frac{\partial w}{\partial y} + \frac{\partial v}{\partial z}\right)\right]$$

Applying the equations to the geometry of a bearing, x is taken along the film circumference, y is taken in the radial direction, and z is taken in the axial direction, as shown in figure 3.1. For a thin film the component of velocity in the y direction is small compared with that in the x and z directions, and the variation of velocity in the x and z directions is small compared with that in the y direction. On this

basis equation 3.2 may be approximated to

$$\frac{\partial P}{\partial x} = \frac{\partial}{\partial y}\left[\mu \frac{\partial u}{\partial y}\right]$$
$$\frac{\partial P}{\partial y} = 0 \qquad (3.3)$$
$$\frac{\partial P}{\partial z} = \frac{\partial}{\partial y}\left[\mu \frac{\partial w}{\partial y}\right]$$

The first and third equations have boundary conditions requiring that there is no slip at the bearing and journal surfaces. These two equations may be integrated to give the circumferential and axial velocity profiles,

$$u = \frac{1}{2\mu} y(y-h)\frac{\partial P}{\partial x} + \left(\frac{U_1 - U_2}{h}\right)y + U_2$$
$$w = \frac{1}{2\mu} y(y-h)\frac{\partial P}{\partial z} \qquad (3.4)$$

assuming no variation in viscosity across the oil film, where U_1 and U_2 are the surface velocities of the shaft and bearing respectively.

Reynolds' equation may now be obtained by applying the equation of continuity to the bearing shown in figure 3.1, which illustrates the bearing notation. The centre of the shaft is displaced from the centre of the bearing under load by a distance e, the eccentricity. The position of an element is defined by an angle ϕ from a radial, fixed axis and the circumferential distance x is given by $x = R\phi$. The local film height, h, is approximated by $h = c(1 + \varepsilon \cos\phi_r)$, where ε is the eccentricity ratio $\frac{e}{c}$, and ϕ_r is the relative angle measured between the instantaneous line of centres and the element. The angle ϕ_r is a relative angle since the line of centres does not remain fixed in space, and the relative circumferential distance is given by $x_r = R\phi_r$.

The equation of mass continuity for the elemental volume, $h\delta x\delta z$, is given by

$$\frac{\partial}{\partial x}\left[\int_0^h \rho u\,dy\right] + \frac{\partial}{\partial z}\left[\int_0^h \rho w\,dy\right] + \frac{\partial}{\partial t}\left[\rho h\right]_{x,z} = 0 \qquad (3.5)$$

It is important to note that equation 3.5 contains both fixed and relative co-ordinate terms, the film height, h, being defined in terms of ϕ_r and the circumferential distance, x, being defined in terms of ϕ.

If there is no viscosity variation across the bearing clearance, then by substituting equation 3.4 into equation 3.5, the continuity equation becomes

$$\frac{\partial}{\partial x}\left[\rho\left(\frac{-h^3}{12\mu}\cdot\frac{\partial P}{\partial x} + \left(\frac{U_1+U_2}{2}\right)h\right)\right] + \frac{\partial}{\partial z}\left[\frac{-\rho h^3}{12\mu}\cdot\frac{\partial P}{\partial z}\right] + \frac{\partial}{\partial t}\left[\rho h\right]_{x,z} = 0$$

which may be rewritten as

$$\frac{\partial}{\partial x}\left[\frac{\rho h^3}{12\mu}\frac{\partial P}{\partial x}\right] + \frac{\partial}{\partial z}\left[\frac{\rho h^3}{12\mu}\cdot\frac{\partial P}{\partial z}\right] = \frac{\partial}{\partial x}\left[\left(\frac{U_1+U_2}{2}\right)\rho h\right] + \frac{\partial}{\partial t}\left[\rho h\right]_{x,z} \qquad (3.6)$$

Equation 3.6 is the Reynolds' equation for a compressible fluid derived in terms of a fixed co-ordinate system. The equation contains the fixed co-ordinate term $x(\phi)$, and also the relative co-ordinate term $x\ (\phi_r)$ used in the definition of local clearance.

The equation may be expressed wholly in terms of the relative co-ordinate system.

3.2. Reynolds' equation in a relative co-ordinate system

The fixed co-ordinate system may be related to the relative co-ordinate system by the expressions

$$\phi = \phi_r + \theta(t)$$

$$\text{or } x = x_r + R.\theta(t)$$

where $\theta(t)$ is the instantaneous displacement of the line of centres from the fixed radial axis. (see figure 3.1)

The required transformations from the fixed co-ordinate system to the relative co-ordinate system are

$$\left[\frac{\partial}{\partial x}\right]_{z,t} = \left[\frac{\partial}{\partial x_r}\right]_{z,t}$$

$$\left[\frac{\partial}{\partial z}\right]_{x,t} = \left[\frac{\partial}{\partial z}\right]_{x_r,t} \qquad (3.7)$$

$$\left[\frac{\partial}{\partial t}\right]_{x,z} = \left[\frac{\partial}{\partial t}\right]_{x_r,z} - R\dot{\theta}\left[\frac{\partial}{\partial x_r}\right]_{z,t}$$

Substituting equations 3.7 into equation 3.6 gives

$$\frac{\partial}{\partial x_r}\left[\frac{\rho h^3}{12\mu}\frac{\partial P}{\partial x_r}\right]_{z,t} + \frac{\partial}{\partial z}\left[\frac{\rho h^3}{12\mu}\frac{\partial P}{\partial z}\right]_{x_r,t} = \frac{\partial}{\partial x_r}\left[\left(\frac{U_1+U_2}{2}\right)\rho h\right]_{z,t} + \frac{\partial}{\partial t}\left[\rho h\right]_{x_r,z} - R\dot{\theta}\frac{\partial}{\partial x_r}\left[\rho h\right]_{z,t}$$

which gives, upon re-arranging and dropping transformation subscripts

$$\frac{\partial}{\partial x_r}\left[\frac{\rho h^3}{12\mu}\frac{\partial P}{\partial x_r}\right] + \frac{\partial}{\partial z}\left[\frac{\rho h^3}{12\mu}\frac{\partial P}{\partial z}\right] = \frac{\partial}{\partial x_r}\left[(U_1+U_2-2R\dot{\theta})\rho h\right] + \rho\frac{\partial h}{\partial t} + h\frac{\partial \rho}{\partial t} \qquad (3.8)$$

Equation 3.8 is the Reynolds' equation for a bearing supplied with a compressible fluid expressed wholly in terms of a rotating co-ordinate system.

For the case of an oil lubricated journal bearing it is assumed that the lubricant is incompressible and that the lubricant film is isothermal, hence ρ = constant and $\frac{\partial \rho}{\partial t} = 0$.

If the bearing is subjected to a constant rotating load the journal centre will perform a circular orbit, hence $\frac{\partial h}{\partial t} = 0$, and the incompressible form of Reynolds' equation for a bearing subjected to a constant rotating load becomes

$$\frac{\partial}{\partial x_1}\left[h^3\frac{\partial P}{\partial x_1}\right]+\frac{\partial}{\partial z}\left[h^3\frac{\partial P}{\partial z}\right]=6\mu(U_1+U_2-2R\dot{\theta})\frac{\partial h}{\partial x_1} \quad (3.9)$$

Equation 3.9 is the same as Reynolds' equation for a steadily loaded bearing with the right hand side of the equation modified by an equivalent velocity $U_{eff}=U_1+U_2-2R\dot{\theta}$ It would, therefore, appear that the bearing subjected to a constant, rotating load may be represented by an equivalent steadily loaded journal bearing having journal velocity U_{eff}, ie. angular velocity $\omega_{eff}=\omega_1+\omega_2-2\dot{\theta}$

3.3. Imposed velocity method

The effective velocity for a bearing subjected to a constant rotating load may be derived more simply by the following method.

If the bearing system of figure 3.2 is considered, the constant, rotating load may be brought to rest by imposing an angular velocity of $-\dot{\theta}$ upon the complete system, thus forming the equivalent bearing system, shown in figure 3.3, which is steadily loaded. The load is stationary, the shaft rotates at an angular velocity, $\omega_1-\dot{\theta}$, and the bush rotates at an angular velocity of $\omega_2-\dot{\theta}$. The steadily loaded bearing of figure 3.3 may be further simplified. The shaft drags lubricant into the convergent clearance at a rate dependent on $\omega_1-\dot{\theta}$, and the bush drags lubricant into the convergent clearance at a rate dependent on $\omega_2-\dot{\theta}$. The total entrainment effect is, therefore, dependent on the sum of the shaft and bush velocities, and the system of figure 3.3 can be reduced to the system of figure 3.4, where a steadily

loaded shaft rotates at an angular velocity $\omega_1+\omega_2-2\dot{\theta}$ in a fixed bush, ie. $\omega_{eff} = \omega_1+\omega_2-2\dot{\theta}$

3.4. Application of theory to White's squeeze film

White's apparatus was a vertical, non-rotating, rigid shaft surrounded by a non-rotating bearing. The bearing was subjected to a constant, rotating load, hence $U_1 = U_2 = 0$, or $\omega_1 = \omega_2 = 0$ and the Reynolds' equation for a bearing with an incompressible fluid subjected to a constant, rotating load is

$$\frac{\partial}{\partial x_r}\left[h^3\frac{\partial p}{\partial x_r}\right] + \frac{\partial}{\partial z}\left[h^3\frac{\partial p}{\partial z}\right] = -12\mu R\dot{\theta}\frac{\partial h}{\partial x_r} \qquad (3.10)$$

3.5. Limitations of Reynolds' equation

Reynolds' equation is a statement of the continuity of the fluid within the clearance of a bearing. The equation is, therefore, applicable only to those regions where the lubricant is single phase. Reynolds' equation can be applied to the convergent region of the bearing clearance, but in the divergent clearance the conditions may be such that the lubricant film ruptures to form gas-filled cavities, and Reynolds' equation is invalidated. The solution of Reynolds' equation to calculate the load carrying capacity of a bearing requires a set of boundary conditions which are governed by the effect of the cavitation region on the continuous region.

3.6. Solution of Reynolds' equation

Reynolds' equation may be solved using numerical

relaxation to obtain the pressure distribution over a bearing.

Equation 3.8 is non-dimensionalised using the following relationships

$$x_r = R\phi_r,\ \bar{z} = L\bar{z},\ H = \frac{h}{c} = 1+\varepsilon\cos\phi_r \qquad \bar{P} = \frac{pc^2}{6\mu U_{eff} R} \tag{3.11}$$

where p is the gauge pressure P-Pa, Pa being atmospheric pressure.

Substituting equations 3.11 into equation 3.8 gives

$$\frac{\partial}{\partial\phi_r}\left[H^3\frac{\partial\bar{p}}{\partial\phi_r}\right] + \alpha^2\frac{\partial}{\partial\bar{z}}\left[H^3\frac{\partial\bar{p}}{\partial\bar{z}}\right] = \frac{\partial H}{\partial\phi_r} \tag{3.12}$$

where α is the ratio of radius to length, $\frac{R}{L}$

The variable $\bar{p}$ may now be replaced by the variable $M = \bar{p}H$, which changes less rapidly with ϕ_r than $\bar{p}$, so improving the numerical accuracy of the solution, and also increasing the rate of convergence. Equation 3.12 becomes

$$\frac{\partial^2 M}{\partial\phi_r^2} + \alpha^2\frac{\partial^2 M}{\partial\bar{z}^2} + F(\phi_r).M = G(\phi_r)$$

where $F(\phi_r) = \dfrac{3\,(2\varepsilon\cos\phi_r + \varepsilon^2(\cos\phi_r)^2 + \varepsilon^2\cos 2\phi_r)}{4\,(1+\varepsilon\cos\phi_r)^{3/2}}$

and $G(\phi_r) = \dfrac{-\varepsilon\sin\phi_r}{(1+\varepsilon\cos\phi_r)^{3/2}}$

The bearing is now characterised by a grid. Each point on the grid is assigned an initial estimate of the value of M. For each point on the grid the derivatives of the variable M with respect to ϕ_r and z are represented by finite difference forms, in this case by using a three point finite difference scheme in each direction. Inserting the finite difference approximations into

Reynolds' equation makes it possible to find a relaxed (modified) value of M at a grid point. If the modified value of M is equal to the original value, Reynolds' equation is locally satisfied, but there is usually a difference, and the basis of the solution is that the modified value is a better approximation than the original value. By repeatedly relaxing all the points on the grid a final converged solution may be reached.

The convergence of the iterative procedure may be increased using over-relaxation, in which the difference between the original grid value and the final grid value is multiplied by a factor and added to the original. This factor, if greater than 2, will cause a numerical instability, but between 1 and 2 will greatly accelerate the rate of convergence. The optimum value for over-relaxation has been derived by Gnanadoss and Osborne (15), and the derivation has been described by Lloyd and McCallion (16).

The optimum over relaxation factor q_{opt} may be expressed as

$$q_{opt} = 2\left\{\frac{1-(1-T^2)^{\frac{1}{2}}}{T^2}\right\}$$

where $T = 1 - 2\pi^2\left\{\frac{1+\left(\frac{\pi R}{L}\right)^2}{I^2+4\left(\frac{\pi RJ}{L}\right)^2}\right\}$

I and J are the number of circumferential and axial grid points respectively.

The iterated solution will yield a region of ϕ_r and z where the values of M are such that negative gauge pressures are occurring. Oil cannot sustain pressures

below its vapour pressure and, therefore, cavities will be formed in the low pressure region. Floberg (17) reported that in his experiments with a flooded, steadily loaded journal bearing air came out of solution from the oil, raising the pressure in the cavitation region to atmospheric after prolonged running. In the analysis used here the pressure within the cavitation region has been taken as atmospheric, and all pressures below atmospheric have been excluded.

The supply pressure to the bearing also affects the predicted pressure profile of the bearing. The bearings used in the experimental work were end-fed, thus one end of the bearing was subjected to the supply pressure, p_{end}, while the pressure at the other end of the bearing was atmospheric. The effect of the supply pressure has been included in all the calculations.

The load carrying capacity of the bearing can be calculated by converting the values of M to give pressures, and integrating the pressure field over the bearing to give the radial and tangential components of the film force, Fr and Fs, as shown in figure 3.5. The total load capacity is given by $\sqrt{F_r^2 + F_s^2}$.

The load angle ψ is the angular displacement of the line of centres from the line of action of the load, and its value is given by $\tan \psi = \frac{-F_s}{F_r}$. For the case of a dynamically loaded journal bearing, whose effective velocity, $\omega_1 + \omega_2 - 2\dot{\theta}$, is greater than zero, the line of centres leads the line of action of the load, as in figure 3.6(a), and the load angle will be described as

positive, or leading. When the effective velocity is less than zero the line of centres will lag the line of action of the load, and the load angle will be described as negative, or lagging, as in 3.6(b).

Figures 3.7 to 3.10 are examples of the theoretical bearing performance. Figures 3.7 and 3.8 show the effect of varying either viscosity or rotational speed on the load carrying capacity of the bearing used in the experimental work. Figure 3.7 shows the effect of variation of viscosity at constant rotational speed, while figure 3.8 shows the effect of varying rotational speed with the viscosity constant. The graphs are shown in the form of log (f) against eccentricity ratio, where f is the non-dimensional film force given by

$$f = \left| \frac{Wc^2}{6\mu U_{eff} R^2 L} \right|$$

W is the load carrying capacity of the bearing.

The effect of varying the cavitation pressure is also shown, the upper curves being for cavitation at the vapour pressure of oil, approximately zero bar absolute (-1.0 bar gauge), and the lower curves being for cavitation at ambient pressure (0.0 bar gauge). The end supply pressure used in the calculations was $10KN/m^2$, the value used in the experimental work.

The variation of viscosity in the range 20cP to 60cP, which is the range of viscosity variation noted experimentally, can be seen to have very little effect on the predicted performance of the bearing. The same comments apply to the case of variation of rotational

speed, where the cases shown are within the range normally used during experimentation.

Figures 3.9 and 3.10 show the variation of load angle with eccentricity for varying viscosity and varying speed. The convention of leading load angle for effective velocities greater than zero, and lagging load angles for effective velocities less than zero is assumed. Again the variations of viscosity and speed within the experimental values have only a slight effect on the predicted curves.

CHAPTER 4

Cavitation

Cavitation can occur within a liquid when the pressure is reduced towards the saturated vapour pressure. Two forms of cavitation may occur, the first being true or vaporous cavitation, which takes place when the pressure drops to the saturated vapour pressure, causing boiling and the formation of vapour cavities. The second type of cavitation is gaseous cavitation which is caused by the release of dissolved gases (normally air) from the liquid as the pressure is reduced towards the vapour pressure.

Both forms of cavitation may occur in the operation of a journal bearing, but gaseous cavitation has normally been observed. The measured pressure within the cavitation region of a steadily loaded journal bearing has been found to be close to atmospheric pressure (see Floberg (17)), whereas a cavitation pressure of absolute zero, the approximate vapour pressure of oil, would have been observed had vaporous cavitation been predominant.

4.1. Steadily loaded journal bearing

The rotation of the shaft in a steadily loaded journal bearing produces a high pressure region within the lubricant in the convergent clearance, and a low pressure region within the divergent clearance. If the pressure within the divergent clearance falls low enough

for cavitation to occur, the fluid film ruptures to form a two phase region. Reynolds' equation is applicable only to a continuous fluid and can apply only to the lubricant in the convergent clearance, but the boundary conditions which must be applied to Reynolds' equation are determined by the cavitated region. Extensive theoretical and experimental work has been carried out to determine the cavitation boundary conditions. The work carried out by Jakobsson and Floberg (10) has led to the wide acceptance of the boundary conditions

$p = \frac{\partial p}{\partial x} = 0$ at the film breakdown boundary

$p = 0$ at the reformation boundary.

Floberg (18) has also carried out work with a glass bearing which allowed observation of the cavitation region. The photographic evidence obtained showed an ordered, symmetrical cavitation region composed of air fingers separated by oil filaments. Similar work has been carried out by Sir G.I. Taylor (19), while Cole and Hughes (20) have worked with bearings with oil feeds through either a single hole or a circumferential groove.

4.2. Dynamically loaded bearing

Lubrication theory suggests that the prediction of the load carrying capacity of a dynamically loaded bearing subjected to a constant rotating load, as shown in figure 3.2, may be carried out using the equivalent, steadily loaded bearing shown in figure 3.4. Experiments have been carried out by Marsh (21) with a self-acting air bearing subjected to a synchronous rotating load, which

indicate that performance prediction with the equivalent bearing is possible. Marsh's work, however, was carried out with air, which is a single phase lubricant. Cavitation could not occur and Reynolds' equation was applicable throughout the film.

4.2.1. Oil lubricated journal bearing

Reynolds' equation applies to the continuous region of a lubricant film, while the cavitation region determines the boundary conditions applied to that continuous region. The equivalence of the bearing systems of figures 3.2 and 3.4 depends not only upon the sum of velocities but also upon the mode of cavitation and, therefore, the boundary conditions. The steadily loaded journal bearing boundary conditions are used in the prediction of the load carrying capacity of the dynamically loaded bearing, and if the cavitation modes are different it is possible that the load carrying capacity of the dynamically loaded bearing may be predicted incorrectly, as indicated by White's results (2).

4.2.2. Experimental evidence

(a) Cole and Hughes

Cole and Hughes (1) made a qualitative study of an oil film with the dynamically loaded bearing rig shown in figure 4.1. The apparatus consisted of a steel shaft rotating in a 25 x 25 mm, non-rotating glass bush, which could be subjected to a constant rotating load by a loading eccentric and springs. The loading system

produced two equal, sinusoidally varying forces which were 90° out of phase, thus producing a resultant which was a constant rotating load. The cavitated region was photographed through the wall of the glass bush.

Cole and Hughes reported that the cavitation zone rotated synchronously with the load, and that its appearance was different from the cavitation zone observed in a steadily loaded bearing. Close inspection of their photographs shows that for a constant rotating load with no shaft rotation, the cavitation zone was composed of many irregular, fern-like cavities, very unlike the ordered cavitation zone seen in a steadily loaded bearing. With the load rotating at constant speed, the shaft speed was increased from rest in the direction of the load. As the effective velocity, $\omega_1 - 2\dot{\theta}$, was increased from $-2\dot{\theta}$ to 0 the extent of the fern-like cavitation zone decreased, until at $\omega_1 - 2\dot{\theta} = 0$ the cavitation zone appeared to have disappeared completely. When $\omega_1 - 2\dot{\theta} = 0$, the theory predicts zero gauge pressures throughout the film, and, hence, no load carrying capacity and no cavitation region, as in Cole and Hughes' photographs. When the shaft speed was increased further, such that $\omega_1 - 2\dot{\theta} > 0$, ie. when the shaft rotation dominated the effective velocity, the cavitation region became of the type normally seen in steadily loaded bearings. Long air fingers separated by oil filaments were seen in the cavitation region.

The photographs show that when the rotating load is dominant a different form of cavitation exists from

when shaft rotation is dominant. Cole and Hughes, however, were unable to comment on the effect of the change of mode of cavitation on the load carrying capacity of the bearing, as the orbital motion of the bearing was not recorded.

(b) D.C. White

White (2) carried out work on an apparatus designed to test the performance of squeeze film journal bearings. A vertical, rigid, non-rotating shaft was surrounded by a non-rotating bearing which was subjected to a constant, rotating load. The load was produced by two hydraulic exciters producing equal, sinusoidally varying forces and mounted at an angular displacement of 90° from each other. The resultant was a constant rotating load. White's results showed that at eccentricity ratios greater than 0.3 the load carrying capacity of the bearing dropped to between one quarter and one fifteenth of the predicted load carrying capacity. White also carried out a visual study of the oil film which pointed to the mode of cavitation as a possible cause of the loss of load capacity.

White replaced his test bearing with a perspex bearing and recorded the behaviour of the oil film with a high speed ciné camera. At low eccentricity ratios the oil film could be seen to be fern-like and irregular, as in the photographs of Cole and Hughes (1). As the high pressure region swept past the camera the cavities could be seen to disappear, and would reappear as the low pressure region passed. It was observed that the oil

film in the bearing was almost stationary. At any point in the film, the lubricant oscillated about a mean position as the minimum clearance rotated. The cavitation region travelled through the almost stationary film as local cavities formed in the low pressure region, and disappeared as the high pressure region passed.

At eccentricity ratios greater than 0.3 the oil film had a crazed appearance. Unlike the cavitation region at low eccentricity ratios, the cavities did not form and disappear, but were present throughout a complete load cycle, and simply expanded and contracted as the low pressure and high pressure regions passed. The lubricant film was almost stationary relative to the bearing surfaces and the cavities were, therefore, stationary relative to both surfaces and the lubricant. White believed that the mode of cavitation may have been the cause of the discrepancy between his experimental results and the theoretical predictions.

4.3. Cavitation in a system with a rotating shaft and rotating bush

The author has carried out work with a bearing rig designed by Smith (22) at Leeds University, in which a horizontal shaft rotates inside a rotating perspex bush. The bearing was subjected to a constant unidirectional load by moving the bush in relation to the shaft to give a required eccentricity. The observation of the low pressure region in this system, the equivalent system of figure 3.3, allowed an interesting comparison between

the cavitation region of White's squeeze film and the cavitation region in a system comprising a rotating shaft and rotating bush, the equivalent system of figure 3.3.

4.3.1. Description of apparatus

Smith's apparatus was composed of a horizontal, rotating shaft surrounded by a rotating bush made of perspex. The shaft could be rotated in one direction only, but the bush could be rotated in the same direction as the shaft and also in opposition to it. Oil was fed by gravity to the bearing ends. The bush could be displaced relative to the shaft to allow variation of the eccentricity ratio. The load could not be measured and all the results described are purely qualitative.

4.3.2. Observations

The bush was first displaced to give an eccentricity ratio of 0.8. The effects of various combinations of shaft and bush speed upon the low pressure region were noted.

(a) Shaft rotation only

Air was entrained immediately from the ends of the bearing when the shaft was started. The low pressure region exhibited air-finger cavitation as observed by Floberg (18).

(b) Shaft and bush rotating in the same direction

When the shaft was started stable air fingers could be seen. The bush was then rotated in the same direction as the shaft, which caused the air fingers in the low

pressure region to become unstable. The film reformation boundary was stable, but the breakdown boundary was unstable. Figure 4.2 is a diagrammatic representation of the process which was observed. At time t the air fingers were branched as in figure 4.2(a) with the branches A_1, A_2, A_3, A_4 in the positions shown. As the shaft and bush rotated the branches passed backwards along the air finger in the direction of rotation, while more branches formed at the tip of the air finger, so that at time $t + dt$ the branches were A_3, A_4, A_5, A_6 as shown in figure 4.2(b). The appearance of the low pressure region was the same at all combinations of shaft and bush speed.

(c) Shaft and bush rotating in opposite directions

The shaft was started and normal finger type cavitation was observed. As the bush speed was increased with the shaft speed held constant, the width of the air fingers decreased and the number increased. There was no sign of branching and the air fingers remained stable until the shaft and bush speeds were almost equal. At this speed the effective velocity is approximately zero. The cavitation region was in the position shown in figure 4.3(a), ie. $\omega_1 + \omega_2 > 0$ and shaft rotation dominates.

When the bush speed was increased so that it was greater than the shaft speed the low pressure region was seen to move from the position shown in figure 4.3(a) to that in 4.3(b) where bush rotation dominates.

(d) Bush rotation only

In this case air fingers were again observed as in the case of rotation of the shaft alone. The film

breakdown boundary was unstable but there was no sign of branching.

The observations quoted above occurred at all eccentricity ratios used and in each case a small region of air bubbles could be seen behind the low pressure zone on the centre line, apparently trapped within a reverse flow region at the film reformation boundary.

4.3.3. Comments

An important difference between White's observations and those on Smith's apparatus is that the cavitation zone in White's apparatus moves through a stationary oil film, while Smith's rig exhibited a stationary low pressure region in a circumferentially moving oil film. The observations of the low pressure region in White's, Cole and Hughes and Smith's apparatus do, however, show that the systems of figures 3.2 and 3.3 may undergo a different form of cavitation from the steadily loaded system in figure 3.4. The differences in cavitation from the steadily loaded bearing may be due to the cavities being unable to attach themselves to a surface. The changes in the form of the cavitation may be responsible for the drop in load carrying compared to the predicted values which was noted by White.

4.4. Validity of the equivalent systems

It is normally assumed that the individual surface velocities of the shaft and bearing have no effect on the cavitation within the lubricant film. The experimental

observations quoted previously suggest that this assumption may not be valid.

In the dynamically loaded bearing of figure 3.2 the low pressure region moves with angular velocity $\dot{\theta}$, the velocity of the load, and if cavitation occurs within the low pressure region the velocity of the cavitation zone is

$R(\dot{\theta}-\omega_1)$ relative to the shaft

and $R(\dot{\theta}-\omega_2)$ relative to the bearing

where R is the radius of the bearing.

In figure 3.3, an equivalent bearing with rotating shaft, rotating bearing and constant unidirectional load, the cavitation region is stationary and the velocities of the cavitation region are again

$R(\dot{\theta}-\omega_1)$ relative to the shaft

and $R(\dot{\theta}-\omega_2)$ relative to the bearing.

The bearing systems of figures 3.2 and 3.3 have the same relative velocities between the low pressure region and the two surfaces.

If the system of figure 3.4 is now considered it can be seen that the low pressure region is stationary and that the cavitation zone will have velocities

$R(2\dot{\theta}-\omega_1-\omega_2)$ relative to the shaft

and 0 relative to the bearing.

It is clear that the bearing system of figure 3.4 has not maintained the velocity of the cavitation zone relative to the two surfaces, and it is possible that this discrepancy may cause the difference in the cavitation zones which has been described.

The cavitation zone in a bearing subjected to a

constant rotating load has normally been considered to be similar to that in a steadily loaded bearing, and it has been assumed that it orbits the bearing synchronously with the load. The load carrying capacity of the dynamically loaded bearing is predicted using the boundary conditions found in a steadily loaded bearing. It has, however, been shown that the bearing systems of figures 3.2, the dynamically loaded bearing, and 3.4, the steadily loaded bearing, do not have the same relative velocities for the cavitation zone. It may, therefore, be incorrect to apply the standard steadily loaded boundary conditions to the dynamically loaded bearing. The possible invalidity of the boundary conditions may be the cause of the differences between White's results and conventional theory.

CHAPTER 5

Planning of apparatus

The experimental results, which White obtained with a squeeze film rig, indicate a large discrepancy between the predicted load capacity and the actual load carrying capacity of a bearing subjected to a constant, rotating load. If White's results were true generally, the load carrying capacity of a dynamically loaded system may be over-estimated by a factor of at least four. Further results were required to compare practical results with theoretical predictions. An apparatus was designed to provide experimental data on the load carrying capacity of a dynamically loaded journal bearing.

5.1. Design options

Conventional theory assumes the equivalence of the dynamically loaded system, figure 3.2, and the steadily loaded system, figure 3.4, to allow the prediction of the load carrying capacity of the dynamically loaded bearing. The steadily loaded boundary conditions would be used in the calculation of load carrying capacity. It has been shown in Chapter 4 that the relative velocities of the cavitation zone with respect to the shaft and bearing are not maintained in the transition from the dynamically loaded bearing to the steadily loaded bearing. The relative velocities are maintained in the step from the dynamically loaded bearing to the system of a rotating shaft with a rotating bearing, which is shown in figure 3.3.

It should be possible to use a dynamically loaded system, as in figure 3.2, or a system composed of a rotating shaft in a rotating bush with a constant load, as in figure 3.3, to determine the effect of the relative velocities on the prediction of load carrying capacity.

5.1.1. Rotating shaft with rotating bush

The first design considered was that of a machine similar to that used later by Smith (22). A diagrammatic cross-section is shown in figure 5.1.

A horizontal bush was to be supported on a pair of radial ball bearings. The bush would be driven by an electric motor through a belt and pulley. Two phosphor-bronze test bearings would be fitted into the bush. The use of two bearings would give the bearing angular stiffness. A horizontal shaft, driven by belt and pulley from an electric motor, would pass through the test bearings, and a loading yoke would transmit a unidirectional, constant load to the shaft through a pair of ball bearings.

5.1.2. Rotating load with rotating shaft

The second design to be considered was that of a rotating shaft supporting a non-rotating bearing which was subjected to a constant rotating load. Three options were available, the first being an apparatus similar to that used by Cole and Hughes (1) and illustrated in figure 4.1. A horizontal bush was surrounded by a non-rotating bearing. The test bearing was subjected to a constant rotating load produced by a mechanical system

which subjected the bearing to two equal, sinusoidally varying forces at right angles to each other.

The second option was an apparatus similar to that used by White (2). A vertical, rotating shaft would support a non-rotating bearing, which would be subjected to a constant rotating load. The load would be produced by two hydraulic exciters generating equal, sinusoidally varying forces at right angles to each other.

The third option is shown in figure 5.2. A vertical shaft would be driven by belt and pulley from an electric motor. A bearing housing containing two test bearings would be mounted around the shaft. Two test bearings would be used to give the assembly angular stiffness. The bearing housing would be restrained from rotation, but would be free to orbit the shaft. A pair of ball bearings and a loading collar would be mounted on the bearing housing. The bearing load would be transmitted from an outer loading ring, which would be mounted concentrically with the shaft. The load would be transmitted through the ball bearings to the test bearings. The loading ring would be free to rotate on a set of bearings, and rotation of the loading ring would cause the bearing to be subjected to a constant rotating load.

5.1.3. Comparison of the designs

The disadvantage of the system comprising a rotating shaft and rotating bush was that it would not have been possible to make reliable comparisons between White's data and the results from the apparatus. The system of

a rotating shaft with a rotating load was chosen, as direct comparison between White's results and the experimental data was possible. Such an apparatus could be run as a conventional steadily loaded rotating shaft and the results compared with the experimental results of Dubois and Ocvirk (23). Squeeze film results could be taken to check White's experimental results by rotating the load with the shaft stationary. Further results could be taken with both shaft and load rotating to determine the effect of proportional variation of shaft and load speed on the load carrying capacity.

The option shown in figure 5.2 was chosen for its inherent simplicity and the ease with which the apparatus could be modified to accept a combination of a steady and a rotating load to allow further work to be carried out. A constant unidirectional load could be transmitted to the bearing housing through a yoke mounted outside the loading ring.

The final design of the apparatus and instrumentation is detailed in the following chapter.

CHAPTER 6

Apparatus and Instrumentation

6.1. General description of apparatus

The final design was as shown in the general arrangement drawing of figure 6.1 and in plates 6.1 and 6.2. The letters used in the text refer to the parts illustrated in the general arrangement drawing.

6.1.1. Shaft (A)

The shaft was turned from EN8 steel to produce a working section of two inches nominal diameter. The diameter of the working section was measured accurately using Solex air gauging equipment, and the results obtained are given in table 1 of appendix I.

The shaft was mounted vertically in the centre of a 1¾ inches thick, mild steel base plate (B). The use of such a massive base plate was considered necessary to damp out vibration, which could have affected the experimental readings. The lower end of the shaft was supported in a single row, deep groove, radial ball bearing mounted in a bearing holder (C). The holder passed through a hole bored centrally in the base plate and was secured by bolts through a flange. The upper end of the shaft was located by a single row, radial, deep groove ball bearing mounted in a housing (D). The housing was at the centre of three radial arms which were clamped to supporting pillars (E). The height of the pillars could be effectively raised or lowered by placing

shims (F) between the pillars and the radial arms. The height could, therefore, be adjusted so that a reasonable preload was placed on the shaft bearings when the arms were clamped to the support pillars. The preload removed axial play from the shaft bearings and increased their radial stiffness. The total radial run-out of the shaft, including the non-circularity of the shaft, was 1.5×10^{-4} inches (3.8×10^{-3} mm.).

The shaft was connected to a $\frac{1}{2}$ H.P. D.C. electric motor by belt and pulley. The shaft speed was variable between 0 and 850 r.p.m. using a Zenith SC2-E-R electronic speed controller.

6.1.2. Bearing assembly

Two phosphor bronze test bearings (G), one inch long, were interference fitted into a bearing housing (H). Two bearings were used to give the test assembly angular stiffness. The bearings were separated by on oil supply chamber, which was radiused to prevent air being trapped within the bearing assembly. Oil was fed to the supply chamber through drillings, the bearings being end-fed as in the apparatus used by White (2). A shallow chamber was provided at the outer ends of the bearings to collect the oil flow, which was piped back to the oil tank. Sealing between the shaft and the bearing housing was effected by lip seals mounted at the extreme ends of the bearing housing.

Two large, single row radial ball bearings were mounted between the outer diameter of the bearing housing (H)

and the inner diameter of a loading collar (J). The outer surface of the loading collar had two diametrically opposite flats machined on it. One was used to carry a target for a load speed transducer, while the other supported the loading system.

The bearing housing and loading collar were fully assembled before the phosphor bronze bushes were machined, so ensuring that deformation did not occur during assembly. The bushes were bored to a nominal diameter of 2.004 inches to give a nominal diametral clearance of 0.004 inches. When the machining had been completed the diameter of the bearings was measured using Solex air gauging equipment, and the results are given in table 2 of appendix I.

The bearing end plates (K), which were bolted to the ends of the bearing housing, held the clamping rings (L) for the ball bearings and compressed the lip seals axially. The upper bearing end plate differed from the lower bearing end plate in that it had three lugs, which could be used to support the bearing assembly. The mounting points for the eccentricity transducers and load speed transducer were also situated on the end plate.

The complete bearing assembly was suspended about the vertical shaft on the end of a long soft spring. The spring terminated in three lengths of Bowden cable (M), which were fitted with eyebolts which passed through the support lugs on the upper end plate. The bearing housing was wired to prevent rotation of the test bearings.

6.1.3. Loading system

The loading ring (N) was mounted concentric to the shaft and bearing system. The outer face of the loading ring was grooved to accept the six supporting bearings, which were mounted on adjustable pillars (P). The concentricity of the loading ring was ensured by careful adjustment of the support pillars. A dial gauge was mounted on the loading ring and set to measure the distance between the shaft and the ring. Rotation of the loading ring allowed measurement of the eccentricity, which could be adjusted by moving the support pillars. The loading ring was set to give a maximum eccentricity of $\pm$ 0.006 inches, most of which was probably due to non-circularity of the loading ring.

A pulley was bolted to the loading ring and connected to a $\frac{1}{2}$ H.P. D.C. motor by a belt. The speed of the loading ring could be varied in the range 0 - 250 r.p.m. by a Zenith SC2-E-R electronic speed controller.

The spring loading mechanism was mounted between the loading ring and loading collar. Two springs (Q) were set over screwed adjusters which were mounted in a reaction plate (R). The reaction plate was bolted to the loading ring. Mild steel caps fitted over the ends of the springs were located in a plate which was bolted to the loading collar. A driving rod (S) could be fitted to transmit the driving torque from the loading ring to the loading collar. Rotation of the loading ring (N) caused rotation of the spring load, and thus the bearing housing was subjected to a constant rotating load.

In practice it was found that the springs were capable of transmitting the driving torque to the loading collar, and the driving rod was omitted.

6.1.4. Oil supply

Oil was supplied to the central supply chamber by a Monopump type SB15. This pump provides a pulseless oil flow without an accumulator. An A.C. Delco paper element filter was used in the supply line to ensure the cleanliness of the oil supply.

6.2. Instrumentation

6.2.1. Eccentricity measurement

Eccentricity was measured using Distec non-contact displacement transducers, which operate on an eddy current principle, and are unaffected by the presence of a dielectric between the probe tip and the target. These transducers were ideal for the situation where oil was present between the shaft and the probe. The transducers were first set to give an output voltage of approximately -8vD.C. The output signal was linear about -8vD.C. for a change in displacement, going more negative for an increased gap and more positive for a reduced gap.

Two probes were mounted on each end of the bearing in the holders fixed to the bearing end plates (K). The probes were set at right angles to each other, and the output voltages were led to oscilloscopes operating in X - Y mode to display the loci of the ends of the bearing.

The output from the probes was of the order $-8v \pm \Delta v$ where Δv was the maximum variation in output voltage from the D.C. level. Δv was in the range 0 - 0.3v. When the load was rotating the speed was low enough to require the use of the oscilloscopes in D.C. mode, which made it impossible to display the bearing loci directly on the oscilloscopes at the required amplifier gain of 0.1v/cm. The base level of -8vD.C. was too high, and it was necessary to reduce the base level to approximately 0v. The D.C. level was reduced using the circuit of figure 6.2.

The eccentricity transducers and level-reduction circuit were calibrated using a small calibration jig. The probe was mounted in a holder and the output of the electronic system compared with the displacement of a two inch diameter specimen of EN8 steel mounted on a micrometer barrel. The gain of the transducers was altered so that all the channels would have the same output/displacement characteristic. The transducers were recalibrated frequently during the testing to ensure that the original output/displacement characteristic was maintained. The variation of output with displacement was 141mv/0.001 inch.

The output of the transducer circuits was fed to two oscilloscopes operating in X - Y mode in order to display the bearing loci. Eccentricity measurement was taken from the oscilloscopes. Accuracy was maintained by frequently checking the calibration of the oscilloscopes. Oscilloscope accuracy was $\pm 5\%$ and readings were taken

to within ± 0.01v on the gain setting of 0.1v/cm.

6.2.2. Force measurement

The compression of the loading springs was measured using internal calipers, which were compared with a vernier gauge. The spring forces were then found using a load-compression calibration, which had been carried out on an E-type tensometer. The compression of the springs was measured to an accuracy of ± 0.1 mm. to give an accuracy of ± 10N. The total bearing force was given by the sum of the spring forces, while the individual bearing load was given by the average spring load.

6.2.3. Speed measurement

(a) Shaft

A six-toothed wheel was mounted at the upper end of the shaft. The wheel rotated passed the tip on an eddy current proximity transducer to produce a periodic square wave form. The signal was fed to an A.M.F. Venner 7735 digital timer counter to give the shaft frequency.

(b) Load

A target was attached to the loading collar (J). An eddy current proximity transducer was mounted on the upper bearing end plate and a periodic signal was produced as the target passed the probe. The signal was fed to an A.M.F. Venner 7735 timer counter, which measured the periodic time.

An advantage of the eddy current transducers used in the work was an output which was invariant with

rotational speed. The transducers were, therefore, suitable for the low speeds of load rotation used in the experiments.

6.2.4. Load angle measurement

The load speed transducer was mounted opposite one of the eccentricity transducers, as shown in figure 6.3. The situation shown is that of shaft and load rotating in the same direction. The output of the eccentricity transducer was sinusoidal, as shown in figure 6.4(a) and oscillated about a base D.C. level of approximately -8v. The output of the load speed transducer was a step function as shown in figure 6.4(b).

The load speed target was mounted opposite the loading system, so that the step in the load speed transducer output coincided with the load passing the displacement transducer. The minimum clearance is given by the minimum on the sinusoidal eccentricity transducer output, and if the load rotates at constant angular velocity $\dot{\theta}$, then the load angle ψ can be given by the formula

$$\psi = \frac{\Delta t}{t_o} \times 360^\circ$$

where Δt is the time interval between the minimum displacement and the load, and t_o is the periodic time corresponding to the angular velocity of the load, $\dot{\theta}$. Unfortunately Δt could not be determined directly.

An electronic circuit was designed which would determine the value of the load angle indirectly. Figure 6.5 shows the final circuit. The output of the

eccentricity transducer, which was oscillating about a mean level of approximately -8vD.C., was passed through a large capacitance to reduce the mean level to 0.0v, as shown in figure 6.6(a). The signal was then passed through an operational amplifier into a 'nand' gate to produce the output shown in figure 6.6(b). As the sinusoidal input voltage to the amplifier went slightly positive, the output of the 'nand' gate dropped to OvD.C., and when the sinusoidal input went slightly negative the output of the 'nand' gate went positive. The load speed signal was conditioned to give the signal shown in figure 6.6(c).

The outputs of the eccentricity shaping circuit and the modified load speed were fed to the 'time B - C' inputs of an A.M.F. Venner 7735 digital timer-counter. The counter was started on the first negative going signal on the B- input and stopped on the first negative going signal on the C- input. The counter was started by the shaped eccentricity signal at the position shown in figure 6.6(b), and was stopped after time t_1 , as shown in figure 6.6(c), for the shaft and bush rotating in the same direction.

If the counter started at an angle of 0°, then the minimum clearance would have occurred at an angle of 270°. The periodic time of the load was t_0 . The load angle Ψ could be represented by the time between the passing of the minimum clearance and the passing of the load at t_1. The load angle Ψ was given by the following expression

$$\psi = 270^\circ - \left(\frac{t_1}{t_o}\right) \times 360^\circ$$

The expression above was valid only when the load and shaft were rotating in the same direction. When the load and shaft were rotating in opposite directions the load angle was given by

$$\psi = \left(\frac{t_1}{t_o}\right) \times 360^\circ - 270^\circ$$

The positive and negative values of load angle, which designated whether the minimum clearance was leading or lagging the load, were given automatically by the formulae above.

The operation of the system described above depended on constant rotation of the load, but did not depend on the speed of rotation.

6.2.5. Oil temperature and viscosity

(a) Oil temperature

The oil temperature was measured with copper-nickel thermocouples at inlet to the supply chamber, and at the two bearing ends. An effective temperature, given by Cameron (24, 25), was then used to determine an effective viscosity. The effective temperature, Teff, was given by

$$Teff = Tin + 0.8\ (Tout - Tin)$$

where Tin is the bearing inlet temperature

Tout is the bearing outlet temperature.

The inlet and outlet temperatures were determined to an accuracy of $\pm$ 0.3°C.

(b) Viscosity measurement

The oil used was Shell Tellus 27, a mineral based

hydraulic oil that was also used by White (2) in his experiments. The viscosity variation of the oil with changing temperature was found using standard, calibrated U-tube viscometers in a thermostatically controlled water bath. The viscosity calibration curve is shown in figure 6.7.

6.2.6. Inlet pressure measurement

The oil supply pressure to the bearing was measured using a bourdon gauge supplied by the Budenberg gauge company.

6.3. Preliminary testing

The completed apparatus has been described in the preceding paragraphs. Only after extensive testing was the final configuration reached. The main problems encountered during the commissioning of the apparatus were connected with the support of the bearing system.

Originally the bearing system was supported on two radial arms mounted at one end in the loading ring, and at the other end in Rotolin linear ball bushings inserted in the loading collar. The weight of the bearing assembly proved too great for the supports, and this system was abandoned in favour of four short wires mounted in screwed adjusters which passed through the upper bearing holder (D). The ends of the wires were located at the upper bearing end plate (K). The orbits at the two ends of the bearing, as shown on the oscilloscopes, were 180° out of phase with the bearing

assembly supported in this way. The motion of the bearing was conical and not purely translational, as required. The support mechanism was changed to a system in which the bearing assembly was held between two sets of compressed springs, as shown diagrammatically in figure 6.8. The downward loading of the springs and the bearing assembly was balanced by the upward force of the lower set of springs. It was found that with such a system the motion of the bearing assembly was conical, and no adjustment of the loading springs could produce the required translational motion. Analysis showed that such a system disobeyed the law of minimum potential energy, and the complete assembly was, therefore, unstable.

The bearing was finally supported by a long, soft spring at the end of the three cables, a method which proved extremely successful. The bearing loci could be adjusted until they were equal and in phase by adjusting the load springs. The motion of the bearing assembly was, therefore, purely translational and the results detailed in Chapter 7 were subsequently taken with this supporting mechanism.

An interesting point to note is that when conical motion existed, there appeared to be a large loss of load carrying capacity at high eccentricity ratios. Quantitative data was not recorded, but this result is similar to that obtained by White (2).

CHAPTER 7

Experimental Method and Results

When the apparatus had been fully developed a set of experimental procedures was designed to measure the performance of the test bearings.

7.1. Experimental method

White's experiments were carried out on a bearing which was supplied with oil by flooding one end of the bearing. In order to maintain similar conditions to those encountered in White's experiments, the oil supply pressure was kept to the low value of $10KN/m^2$. White carried out one set of results with an inlet pressure of $10lbf/in^2$ and one set of results was carried out later at $100KN/m^2$ (approximately $14lbf/in^2$) to allow comparison.

The experimental methods for the various configurations possible were as described below.

(a) Steadily loaded bearing

A rotating shaft subjected to a constant, unidirectional load, the steadily loaded bearing, was taken as the control case. The performance of steadily loaded bearings is well documented and agrees closely with theory, thus allowing the results taken from the apparatus to be compared with existing results, to ensure the correct performance of the bearing.

The oil pump was started to fill the bearing and the supply pressure was set to $10KN/m^2$. The shaft speed was set to a constant value and the apparatus was allowed

to settle to its stable operating temperature at that shaft speed. The oil in the bearing clearance was subjected to high viscous shearing, which caused a large temperature rise within the film. The temperature rise was dependent on the shaft speed. Because of the length of time required for the apparatus to reach a steady operating temperature at a given shaft speed, the most efficient way of carrying out the testing was to set the shaft to a constant speed, and take readings as the load was varied, with the shaft speed maintained at its preset value to ensure a constant operating temperature. When the oil temperatures at inlet to and outlet from the bearing were constant, a test was carried out at the preset shaft speed.

The bearing was loaded by compressing the two loading springs equally. The load was then rotated very slowly while the eccentricities of both ends of the bearing were observed on the oscilloscopes. If the two loci were of unequal amplitude, small adjustments were made to the loading springs until the eccentricities at each end of the bearing were equal, thus ensuring that the motion of the bearing was purely translational. When equal orbits were achieved a set of results was taken.

The readings of eccentricity and load angle were obtained by allowing the load to rotate very slowly. Eccentricity readings were then taken from the oscilloscopes and the load angle results noted. At all times great care was taken to ensure that the load speed was kept to such a value that it would have no significant effect on the performance of the bearing, or the mode of cavitation.

The maximum error in the non-dimensional film force, $\left|\frac{Wc^2}{6\mu U_{eff} R^2 L}\right|$, due to load rotation, was approximately ±8 percent at the minimum shaft speed used of 300 r.p.m., and dropped to ± 3 percent at the maximum shaft speed used, 800 r.p.m. The load was then altered to obtain another set of readings, giving the characteristics of variation of load angle and eccentricity with varying load, for constant shaft speed.

When the test had been completed, the shaft speed was reset to allow another set of results to be taken. The shaft speeds used ranged between 300 r.p.m. and 800 r.p.m. in increments of 100 r.p.m.

(b) Rotating load only

The shaft was held stationary and the bearing subjected to a constant rotating load, to produce a situation similar to that in White's squeeze film bearing.

The bearing was first filled and the supply pressure was set to $10KN/m^2$. The load was applied by compressing the two loading springs equally, and then rotated at speeds in the range between 0 r.p.m. and 250 r.p.m. Small adjustments were made to the load springs at each value of speed to ensure that the bearing was undergoing pure translational motion. Readings of load angle and eccentricity were taken when the orbits at both ends of the bearing were equal.

It was possible to take a set of results immediately after changing the load speed, because it was found that the pure rotating load did not cause a temperature rise within the oil film. The shaft centre orbited at constant

eccentricity through an almost stationary oil film (see Chapter 4). There was little viscous shearing within the oil film. At any given point the oil in the film oscillated about a mean position as the minimum clearance rotated. The net work done on the fluid was very small, and there should, theoretically, have been negligible temperature rise. During testing no detectable temperature increase was noted.

The characteristic determined for the bearing operating as a squeeze film was the variation of eccentricity and load angle for varying load speed, with the load held constant.

When a complete set of readings had been taken for a particular load, the load was changed, and the procedure repeated.

(c) Rotating load with rotating shaft

The bearing was filled with oil and the supply pressure set to $10KN/m^2$.

As with the experiments for the steadily loaded bearing, the most efficient way of carrying out the testing for a rotating shaft with a rotating load was to maintain a constant shaft speed, to allow the apparatus to reach its equilibrium temperature at that shaft speed. When equilibrium had been reached load speed could be altered, and results taken for the operation of the bearing at the preset shaft speed. The shaft speed could then be altered to allow another set of readings to be taken.

When the oil exit temperatures were stable testing

could begin. The bearing load was applied by compressing the two loading springs equally. The load speed was then varied in the range 0 r.p.m. to 250 r.p.m. both in the same direction as, and in opposition to the shaft.

The load was then changed and the procedure described above repeated. When the test had been completed the shaft speed was altered and the results repeated at the new shaft speed.

The shaft speeds used were between 100 r.p.m. and 800 r.p.m. in increments of 100 r.p.m. The load speed was varied between 0 r.p.m. and 250 r.p.m. in increments of 50 r.p.m., both in the same direction and in opposition to the shaft. The ranges of effective velocity, which were examined, are detailed in the table below.

Shaft speed range (r.p.m.)	$\omega_1 - 2\dot{\theta}$	Effect
100 - 800	$0 < \omega_1 - 2\dot{\theta} < \omega_1$	shaft rotation dominates load angle leads
100 - 500	$\omega_1 - 2\dot{\theta} = 0$	load capacity zero at $\omega_1 - 2\dot{\theta} = 0$
100 - 400	$\omega_1 - 2\dot{\theta} < 0$	load rotation dominates load angle lags
100 - 800	$\omega_1 - 2\dot{\theta} > \omega_1$	load rotates in opposite direction to shaft and reinforces load carrying capacity

7.2. Presentation of Results

(a) Load carrying capacity

The load carrying capacity of the bearing is shown in figures 7.3, 7.5 and 7.7 to 7.14. The logarithm of the non-dimensional film force, f, is plotted against eccentricity ratio, where

$$f = \left| \frac{Wc^2}{6\mu U_{eff} R^2 L} \right|$$

W being the individual bearing load.

On each figure the solid line indicates the conventionally predicted load carrying capacity, assuming constant cavitation pressures of either atmospheric, $p_{cav} = 0.0$, or absolute zero, $p_{cav} = -1.0$.

(b) Load angle

Figures 7.4, 7.6 and 7.15 to 7.22 show the variation of load angle with eccentricity ratio in polar co-ordinate form. On each figure the boundaries given by the theoretical values of load angle for cavitation pressures of atmospheric, $p_{cav} = 0.0$, and absolute zero, $p_{cav} = -1.0$ are shown.

(c) Variation of eccentricity ratio with $\frac{\dot{\theta}}{\omega_1}$ at constant load

For the combination of a rotating shaft with a rotating load, the results for load carrying capacity may be redrawn to show the variation of eccentricity ratio with the ratio of load speed to shaft speed, $\frac{\dot{\theta}}{\omega_1}$. These results are shown in figures 7.23 to 7.30 and are intended to demonstrate the loss of load carrying capacity as the effective velocity, $\omega_1 - 2\dot{\theta}$, tends to zero,

ie. when $\frac{\dot{\theta}}{\omega_1}$ tends to 0.5.

(d) Tabulated results

The results plotted in figures 7.3 to 7.30 are tabulated in appendix II, tables A1 to A20.

7.3. Discussion of results

Dubois and Ocvirk (23) have carried out experimental work in a steadily loaded bearing which yielded the results shown in figures 7.1 and 7.2. Their results are compared with conventional theory, assuming a cavitation pressure of atmospheric, and an end-pressure, p_{end}, of atmospheric. In their apparatus oil was supplied to the bearing through a central hole. Figure 7.1 shows the variation of non-dimensional film force with eccentricity ratio, while figure 7.2 shows the variation of load angle with eccentricity ratio. In both cases the results agree closely with the conventional theory, which is shown as solid lines. The results of Dubois and Ocvirk represent a data set with which the results taken from the apparatus described in this thesis may be compared.

7.3.1. Steadily loaded bearing

The results for the steadily loaded bearing are tabulated in appendix II, tables A1 and A2.

(a) Load carrying capacity

The variation of film force with eccentricity ratio is shown in figure 7.3. The tests were carried out at various shaft speeds, thus each individual test was run at a different oil temperature. The theoretical curve

corresponds to an average viscosity of 23cP. The performance of the bearing can be seen to agree closely with the theory, and also with the results of Dubois and Ocvirk (23), for a steadily loaded bearing. Results were obtained between eccentricity ratios of 0.6 and 0.9. Lower eccentricity ratios were not possible due to the bearing becoming unstable. It can be seen that the bearing is performing as predicted at high eccentricities.

(b) Load angle

Figure 7.4 compares the experimental load angle results with the envelope produced by the theoretical predictions of load angle for cavitation pressures of atmospheric and absolute zero. The curves are shown for viscosities of 28cP and 17.6cP to cover the range of viscosities encountered during the experimentation. The experimental results can be seen to be in close agreement with theory.

7.3.2. Rotating load results

The results for a rotating load without shaft rotation are given in tables A3 and A4 of appendix II. The results investigate the performance of the end-fed squeeze film bearing, as investigated by White (2). The results shown in figures 7.5 and 7.6 may be compared with White's experimental results.

(a) Load carrying capacity

The variation of non-dimensional film force with eccentricity ratio is shown in figure 7.5. The results are shown for eccentricity ratios greater than 0.45.

Lower eccentricity ratios could not be achieved due to the instability of the bearing, but these higher eccentricity ratios are most important for comparison with White's results. Figure 7.5 shows that the performance of the bearing is closely predicted by theory. There is no indication of the drop in load carrying capacity shown in White's investigations.

(b) Load angle

Figure 7.6 shows that the load angle of the bearing is in close agreement with the theory for a cavitation pressure of absolute zero, $p_{cav} = -1.0$.

7.3.3. Rotating load with rotating shaft

The results for a rotating load with a rotating shaft are tabulated in appendix II, tables A5 - A20. The behaviour of the bearing is shown in graphical form in figures 7.7 to 7.30.

(a) Load carrying capacity

Figures 7.7 to 7.14 show the variation of non-dimensional film force with eccentricity ratio for varying load speed, while shaft speed and load were maintained constant. Each figure shows the results taken at a constant shaft speed. For all values of shaft speed and load there is good agreement between the performance of the bearing and theory. There is no indication of the drop in load capacity which White's results suggest.

(b) Load angle

The variation of load angle with eccentricity

ratio is shown in figures 7.15 to 7.22.

(i) Ns = 100 r.p.m. to Ns = 400 r.p.m.

Figures 7.15 to 7.18 show the results obtained for shaft speeds which allowed a change in value of effective velocity from $\omega_1 - 2\dot{\theta} > 0$ to $\omega_1 - 2\dot{\theta} < 0$ as the load speed was increased in the direction of the shaft. Theory indicates a positive (leading) load angle for $\omega_1 - 2\dot{\theta} > 0$, and a negative (lagging) load angle for $\omega_1 - 2\dot{\theta} < 0$. It can be seen that there is good agreement with the conventional theory. As the effective velocity, $\omega_1 - 2\dot{\theta}$, tends towards zero, the load angle decreases towards 0°, until at an effective velocity of zero, the eccentricity ratio is one, and the load angle is 0.0°. The results can be seen to be in good agreement with theory. As $\omega_1 - 2\dot{\theta}$ goes negative the eccentricity should decrease and the load angle should go negative. The results continue to agree with theory in the region of negative load angle.

(ii) Ns = 500 r.p.m. to Ns = 800 r.p.m.

Figures 7.19 to 7.22 show those results for which the effective velocity was always greater than or equal to zero. Theory predicts a leading load angle and practical results were in good agreement.

(c) Variation of eccentricity ratio with the ratio $\frac{\dot{\theta}}{\omega_1}$ at constant load

Figures 7.23 to 7.30 illustrate the variation of eccentricity ratio with the ratio of load speed to shaft speed, $\frac{\dot{\theta}}{\omega_1}$, to show the reduction in the load carrying capacity of the bearing as $\omega_1 - 2\dot{\theta}$ tends to zero,

ie. at $\frac{\dot{\theta}}{\omega_1} = 0.5$.

As in the work of Stone and Underwood (12), the results show that reduction of the effective velocity, $\omega_1 - 2\dot{\theta}$, by increasing the load speed in the same direction of rotation as the shaft, will cause a decrease in the load carrying capacity of the bearing and an increase in eccentricity ratio as $\omega_1 - 2\dot{\theta}$ decreases from ω_1 to zero, ie. $\frac{\dot{\theta}}{\omega_1}$ increases from 0 to 0.5. Theory predicts zero load carrying capacity and an eccentricity ratio of 1.0 at $\omega_1 - 2\dot{\theta} = 0, \frac{\dot{\theta}}{\omega_1} = 0.5$. As the load speed is increased further in the direction of shaft rotation the effective velocity decreases from zero as $\frac{\dot{\theta}}{\omega_1}$ increases from 0.5. $|\omega_1 - 2\dot{\theta}|$ increases and the load carrying capacity increases, thus reducing the eccentricity ratio. When the load is rotated in opposition to the shaft the effective velocity increases, and the load carrying capacity should increase, causing a decrease in eccentricity ratio for $\frac{\dot{\theta}}{\omega_1} < 0$.

<u>(i) Ns = 100 r.p.m. to Ns = 400 r.p.m.</u>

Figures 7.23 to 7.26 show the results obtained for shaft speeds which allowed investigation of speed ratios both greater than and less than 0.5. As the load speed was increased from rest in the direction of the shaft, ie. $\frac{\dot{\theta}}{\omega_1}$ was increased from 0, the eccentricity ratio could be seen to increase, showing the reduction in load carrying capacity predicted by theory. At the critical speed ratio, $\frac{\dot{\theta}}{\omega_1} = 0.5$, the load carrying capacity is zero and the eccentricity ratio 1.0, as predicted by theory. As $\frac{\dot{\theta}}{\omega_1}$ increases from 0.5, $|\omega_1 - 2\dot{\theta}|$ increases, and the load

carrying capacity increases as the eccentricity ratio decreases. Rotation of the load in opposition to the shaft causes a decrease in eccentricity ratio and an increase in load carrying capacity, as shown by $\frac{\dot{\theta}}{\omega_1} < 0$

(ii) Ns = 500 r.p.m. to Ns = 800 r.p.m.

Figures 7.27 to 7.30 show those results taken for shaft speeds such that $\omega_1 - \dot{\theta} > 0$. As the load speed is increased in the direction of the shaft, $\frac{\dot{\theta}}{\omega_1}$ increases from 0 towards 0.5, and the predicted increase in eccentricity ratio and decrease in load capacity occurs. As the load speed is increased from rest in opposition to the shaft, causing $\frac{\dot{\theta}}{\omega_1}$ to decrease from 0.0, the load carrying capacity increases as the eccentricity ratio decreases, which is predicted by the theory.

7.3.4. Pressurised delivery

White conducted a single test with an oil delivery pressure of 10lbf/in^2. With an unpressurised delivery the load carrying capacity of the bearing had been one eighth of the predicted value. With the pressurised delivery it was found that the load carrying capacity was one quarter of the predicted value. A single test was, therefore, carried out to determine whether an increase in the oil supply pressure would alter the accuracy of prediction of load carrying capacity. The test was carried out with both the shaft and load rotating.

Shaft speed was set to 300 r.p.m. and supply pressure was set to 100KN/m^2. The results are tabulated in appendix II, tables A21 and A22, and are plotted in

figures 7.31 to 7.33. Although the results for load carrying capacity are less in agreement with theory than the results quoted previously, the discrepancy between theory and experiment remains far smaller than that shown by White. The load angle results shown in figure 7.32 are in good agreement with the theory. Figure 7.33 shows the variation of eccentricity ratio with $\frac{\dot{\theta}}{\omega_1}$ and the results can be seen to be similar to those shown previously, apart from an unexpected drop in eccentricity ratio as $\frac{\dot{\theta}}{\omega_1}$ goes negative for a load of 228N. A loss of load carrying capacity at $\frac{\dot{\theta}}{\omega_1} = 0.5$ is again shown.

CHAPTER 8

Final Discussion and Conclusions

8.1. Discussion

A derivation of Reynolds' equation for a bearing subjected to a constant rotating load has been described. The equation has been solved numerically to determine the load carrying capacity of a bearing by assuming the cavitation region to be well defined, as in a steadily loaded bearing. The results obtained from this form of analysis are at variance with the experiments of White (2), which indicated that a squeeze film bearing could support only between 6 percent and 25 percent of its predicted load carrying capacity at eccentricity ratios greater than 0.35. At lower eccentricity ratios White reported good agreement with conventional theory.

The experimental work carried out on the test bearing described in Chapter 6 has investigated three operating modes; the steadily loaded bearing, the squeeze film bearing, and a combination of a constant, rotating load upon a rotating shaft. The results for the steadily loaded bearing agree closely with theory, and also with the experimental results of Dubois and Ocvirk (23). When the bearing was operated as a squeeze film subjected to a constant rotating load, the situation investigated by White (2), theory and experiment were found to be in good agreement for the eccentricity ratios measured, which were greater than 0.45. The loss of load carrying capacity, which was found in White's investigation, did not occur.

The work was extended to include the case of a rotating shaft which supported a non-rotating bearing, which was subjected to a constant, rotating load, and theory and experiment were again found to be in good agreement.

The major query which arises is concerned with the difference between White's results and the results described in this thesis. The test bearing did not lose its load carrying capacity with respect to conventional theory at high eccentricity ratios. It is possible that the differences may be a result of the experimental methods used. Throughout the work described here, great care was taken to ensure that the motion of the test bearing was purely translational. The bearing housing was equipped with two pairs of proximity transducers, which allowed the observation of the motion of the extreme ends of the bearing housing. Pure translational motion was ensured by monitoring the orbits of both ends of the bearing on the oscilloscope screens, and making small adjustments of the loading springs until the orbits were equal and in phase. The gain of the amplifiers, which were used to power the proximity transducers, showed very little tendency to drift, but frequent checks were made on the four channels to ensure that the gain of the four transducers remained equal. In comparison, White's results were taken from a single pair of transducers positioned to measure the motion of the centre of the bearing. It is possible that the bearing may have undergone conical motion, even though the measured orbit was circular. Such motion could have caused the discrepancy between

White's experimental results and conventional theory. During the commissioning of the test rig described in this thesis, problems with the suspension system for the bearing housing caused conical motion to occur, and an apparent loss of load carrying capacity was detected, as in White's work.

The performance of a dynamically loaded bearing subjected to a constant, rotating load has been based on an equivalent steadily loaded bearing. The cavitation region has been modelled as well defined and similar to that in the steadily loaded bearing. Visual evidence, however, has been collected by Cole and Hughes (1) and White (2), which shows that the cavitation region is composed of a crazed pattern of air bubbles and oil. Conventionally, the velocity of the low pressure region with respect to the bearing surfaces has been assumed to have no effect on the mode of cavitation within a bearing, but the observations of Cole and Hughes (1) and White (2) show that this is not true. It appeared probable that the discrepancy between White's experimental results and the conventional theory may have been due to the inadequacy of the boundary conditions used.

It has been shown that in the transformation from the bearing subjected to a constant rotating load to the equivalent steadily loaded bearing, the relative velocities between the low pressure region and the bearing surfaces are not maintained. It was thought that the loss of equivalence may have caused the differences between White's results and the theory. The cavitation region

in the steadily loaded bearing has zero relative velocity with respect to the bearing, while in the dynamically loaded bearing it is given by the term $R(\dot{\theta}-\omega_r-\omega)$. The additional relative motion of the cavitation region may cause the physical difference in the cavitation form between the two loading régimes.

Despite the differences in the modes of cavitation, the work described here has shown that the performance of a bearing under a constant rotating load may be predicted accurately using conventional methods. The cavitation region in the steadily loaded bearing is well defined and may be adequately modelled by replacing any predicted negative gauge pressures with atmospheric pressure. The dynamically loaded bearing contains an ill-defined cavitation region composed of a crazed mixture of oil and air, yet the results described in this thesis show that the boundary conditions for the steadily loaded bearing may be applied to the theory to give reasonable performance prediction.

The cavitation region in the dynamically loaded bearing is a crazed mixture of oil and air bubbles. If the air comes out of solution at a pressure close to atmospheric, as is normally assumed, then it is very probable that the oil regions within the overall cavitation zone will also be close to this pressure. The region of cavitation could then be modelled by assuming that negative pressures could not exist without the occurence of some form of cavitation. Predicted negative pressures would be replaced by atmospheric pressure.

The boundary conditions for the dynamically loaded bearing would then, as a first approximation, be identical to those of the steadily loaded bearing and the agreement between theory and experiment shown in Chapter 7 would be expected.

8.2. Proposals for further work

Very little experimental data on the performance of dynamically loaded bearings has been collected previously. This thesis has extended the available information, but further work is required in this important field - few bearings undergo steady loading alone. It is important to understand the behaviour of a bearing under simple loading forms before going on to tackle the complicated loading patterns normally found in working machinery. A valuable addition to such work could be made by observing the performance of a bearing subjected to a combination of steady load and constant rotating load. The apparatus described here could be modified simply for such work. Useful work might also be carried out on a dynamically loaded bearing in which cavitation is suppressed by a high oil delivery pressure.

Apart from performance investigations, it is important that the mode of cavitation in the dynamically loaded bearing be better understood. Further investigation of the cavitation region in such a bearing is required in an attempt to determine the boundary conditions.

8.3. Conclusions

This report has given an account into the performance of a dynamically loaded journal bearing. Reynolds' equation has been solved to predict the performance of a bearing subjected to a constant rotating load, and good agreement has been found between the theory and the experimental data for the high eccentricities investigated. The work has shown that conventional theory, assuming steadily loaded boundary conditions, can be used to predict the performance of the bearing subjected to constant rotating load to sufficient accuracy for the designer.

The cavitation region in the dynamically loaded bearing has been shown by Cole and Hughes (1) and White (2) to be very different from that in the steadily loaded bearing. Even though the photographs show that the two loading forms promote very different forms of cavitation, it is probable that the boundary conditions imposed by the cavitation regions are similar, and may be modelled, as a first approximation, by p_{cav} = constant = atmospheric. The validity of the boundary conditions has not been confirmed, but until the cavitation region in the dynamically loaded bearing is better understood the work described in this thesis should give the designer more confidence in the prediction methods available to him.

References

1. Cole, J.A., and Hughes, C.J., 'Visual study of film extent in dynamically loaded, complete journal bearings.' Proc. Conf. Lub. Wear, Instn. Mech. Engrs, London, 1957, paper 87, pp.147-150, 12, 750.

2. White, D.C., 'Squeeze film journal bearing', Ph.D. thesis, Cambridge, 1970.

3. Harrison, W.J., 'The hydrodynamic theory of the lubrication of a cylindrical bearing under variable load, and of a pivot bearing', Trans. Camb. Phil. Soc., 1919, 22, pp.373-388.

4. Swift, H.W., 'Fluctuating loads in sleeve bearings', J. Inst. Civ. Engrs., 5 1936-37, pp.161-195.

5. Burwell, J.T., 'The calculated performance of dynamically loaded sleeve bearings', Trans. Amer. Soc. Mech. Engrs., J. Appl. Mech., 1947, 14, pp.A231-245.

6. Burwell, J.T., 'The calculated performance of dynamically loaded sleeve bearings -II', Trans. Amer. Soc. Mech. Engrs., 71, pp.358-360.

7. Burwell, J.T., 'The calculated performance of dynamically loaded sleeve bearings -III', Trans. Amer. Soc. Mech. Engrs., 1951, 18, no. 4, pp.393-404.

8. Ott, H.H., 'Zylindrische Gleitlager bei instationärer Belastung', Verlag A.G. Leemann, Zurich, 1964.

9. Hahn, H., 'Dynamically loaded journal bearings of finite width', Proc. Conf. Lub. Wear., Instn. Mech. Engrs., London, 1957, paper 55, pp.100-110.

10. Jakobsson, B., and Floberg, L., 'The finite journal bearing considering vaporisation', Nr. 190, Instn. Mach. Elements, Chalmers University, Goteborg, Sweden.

11. Horsnell, R., and McCallion, H., 'Prediction of some journal bearing characteristics under static and dynamic loading', Proc. Conf. Lub. Wear., Instn. Mech. Engrs, London, 1963, paper 19, p.126.

12. Stone, J.M., and Underwood, A.F., 'Load carrying capacity of journal bearings', Q.S.A.E. Trans., 1947, 1, p.56.

13. Simons, E.M., 'The hydrodynamic lubrication of cyclically loaded bearings', Trans. Amer. Soc. Mech. Engrs., 1950, 72, p.805.

14. Shawki, G.S.A., and Freeman, P., 'Journal bearing performance under sinusoidally altering and fluctuating loads', Proc. Instn. Mech. Engrs., London, 1955, 169, p.689.

15. Gnanadoss, A., and Osborne, M.R., 'The numerical solution of Reynolds' equation for a journal bearing', Q.J. Mech. Appl. Maths., 1964, 17, Pt. 2, p.241.

16. Lloyd, T., and McCallion, H., 'Recent developments in fluid film lubrication theory', Proc. Instn. Mech. Engrs., 1967-68, 182, Pt. 3A, pp.36-50.

17. Floberg, L., 'Boundary conditions of cavitation in journal bearings', Trans. Amer. Soc. Lub. Engrs., 1961, 4, pp.282-286.

18. Floberg, L., 'Cavitation in lubricating oil films', Cavitation in Real Liquids, Elsevier, 1964, pp.138-146.

19. Taylor, G.I., 'Cavitation in hydrodynamic lubrication', Cavitation in Real Liquids, Elsevier, 1964, pp.80-101.

20. Cole, J.A., and Hughes, C.J., 'Oil flow and film extent in complete journal bearings', Proc. Instn. Mech. Engrs., London, 1956, 170, pp.499-511.

21. Marsh, H., 'The stability of aerodynamic gas bearings, Pt. II, 'Non-circular bearings', Report for Ministry of Aviation, 1964.

22. Smith, E.H., 'A study of film rupture in hydrodynamic lubrication', Ph.D Thesis, Leeds University, 1975.

23. Dubois, G.B., and Ocvirk, F.W., 'Analytical derivation and experimental evaluation of short bearing approximation for full journal bearings', N.A.C.A. Technical Report no. 1157, 1953.

24. Cameron, A., Principles of Lubrication, Longmans, 1966, p.398.

25. Cameron, A., Basic Lubrication Theory, Longmans, 1971, p.105.

26. Hummel, C., 'Kritische Drehzahlen als Folge der Nachgiebigkeit des Schmiermittels in Lager,' V.D.I. Forschungsheft, 1926, 287

APPENDIX I

Metrology

Table 1 Dimensions of shaft

Table 2 Dimensions of bearings

Table 1 Dimensions of shaft

Shaft measurements were taken at the bearing positions on the shaft. Readings were taken in three positions: top end of bearing, centre and bottom end. Maximum and minimum readings were taken at each point.

(a) Upper bearing

Position	Maximum Diameter (Inches)	Minimum Diameter (Inches)
Top	1.99977	1.99985
Centre	1.99975	1.99988
Bottom	1.99977	1.99985
Average = 1.99981 Inches		

(b) Lower bearing

Position	Maximum Diameter (Inches)	Minimum Diameter (Inches)
Top	1.99967	1.99975
Centre	1.99972	1.99980
Bottom	1.99977	1.99983
Average = 1.99975 Inches		

Overall average diameter = 1.99978 Inches

Accuracy 2×10^{-5} Inches

Table 2 Dimensions of bearings

The bearing measurements were carried out in a similar manner to the shaft measurements.

(a) Upper bearing

Position	Maximum Diameter (Inches)	Minimum Diameter (Inches)
Top	2.00410	2.00408
Centre	2.00405	2.00400
Bottom	2.00402	2.00398
Average = 2.00404		

(b) Lower bearing

Position	Maximum Diameter (Inches)	Minimum Diameter (Inches)
Top	2.00408	2.00406
Centre	2.00400	2.00396
Bottom	2.00398	2.00389
Average = 2.00400		

Average over both bearings = 2.00402

Average diametral clearance = 4.25×10^{-3} Inches

Accuracy of readings = 2×10^{-5} Inches

APPENDIX II

Tabulated Results

Rotating shaft only p_{end} = 10KN/m^2 A1

Ns = 300 r.p.m. μ = 26.7cP			Ns = 400 r.p.m. μ = 22.8cP			Ns = 500 r.p.m. μ = 26.4cP		
$\psi°$	f	ε	$\psi°$	f	ε	$\psi°$	f	ε
37	.55	.84	48	.47	.89	56	.30	.79
35	.52	.81	50	.43	.84	60	.28	.77
47	.44	.79	50	.36	.79	58	.25	.74
51	.39	.77	58	.32	.76	62	.22	.71
48	.33	.76	61	.29	.72	66	.20	.66
48	.28	.74	67	.25	.69	65	.17	.63
53	.24	.72	73	.21	.66	71	.14	.61
84	.20	.71				74	.12	.59
72	.17	.69						

Rotating shaft only p_{end} = 10KN/m²

A2

Ns = 600 r.p.m. μ = 20.4cP			Ns = 800 r.p.m. μ = 17.6cP					
$\psi°$	f	ε	$\psi°$	f	ε	$\psi°$	f	ε
57	.32	.79	48	.27	.72			
59	.29	.77	40	.26	.71			
66	.27	.74	53	.23	.69			
49	.24	.73	53	.21	.68			
54	.22	.71	62	.19	.66			
62	.19	.69	63	.16	.63			
84	.16	.66						
86	.13	.63						

Rotating load only Pend = 10KN/m^2

W = 344N		μ = 66cP		W = 288N		μ = 66cP	
N_L	ψ°	f	ε	N_L	ψ°	f	ε
25	-25	1.13	.97	25	-29	1.00	.94
50	-40	.57	.86	50	-51	.50	.84
75	-51	.38	.77	75	-54	.33	.77
100	-51	.28	.72	100	-58	.25	.71
150	-57	.19	.68	150	-61	.17	.64
200	-68	.14	.63	200	-71	.13	.59
250	-59	.11	.58	250	-63	.1	.56

Rotating load only $p_{end} = 10KN/m^2$ A4

W = 228N μ = 66cP

N_L	ψ°	f	ε	N_L	ψ°	f	ε
25	-44	.79	.89				
50	-53	.40	.77				
75	-60	.26	.71				
100	-64	.20	.66				
150	-75	.13	.58				
200	-78	.16	.51				
250	-82	.08	.46				

Rotating load with rotating shaft $p_{end} = 10KN/m^2$ A5

Ns = 100 r.p.m. W = 344N μ = 50.6cP				Ns = 100 r.p.m. W = 288N μ = 46cP			
N_L	ψ°	f	ε	N_L	ψ°	f	ε
50	8	∞	1.0	50	4.26	∞	1.0
100	-18	.78	.95	100	-34	.71	.87
150	-27	.39	.89	150	-33	.35	.79
200	-28	.26	.77	200	-36	.24	.72
250	-34	.20	.69	250	-44	.18	.66
-50	50	.39	.91	-50	56	.35	.81
-100	55	.26	.76	-100	62	.24	.74
-150	51	.20	.69	-150	66	.18	.69
-200	53	.16	.64	-200	70	.14	.63
-250	42	.13	.59	-250	64	.12	.59
0	50	.78	.94	0	38.1	.71	.91

Rotating load with rotating shaft $p_{end} = 10KN/m^2$ A6

Ns = 100 r.p.m. W = 228N μ = 46cP				Ns = 100 r.p.m. W = 168N μ = 46cP			
N_L	ψ°	f	ε	N_L	ψ°	f	ε
50	1	∞	1.0	50	15	∞	1.0
100	-33	.57	.86	100	-59	.42	.74
150	-43	.29	.72	150	-68	.21	.64
200	-49	.19	.66	200	-81	.14	.58
250	-68	.14	.61	250	-86	.11	.53
-50	70	.29	.76	-50	79	.21	.63
-100	74	.19	.66	-100	93	.14	.58
-150	80	.14	.61	0	60	.42	.86
-200	83	.11	.56				
-250	73	.10	.53				
0	44	.57	.88				

Rotating load with rotating shaft $p_{end} = 10KN/m^2$ A7

Ns = 200 r.p.m. W = 317N μ = 38cP				Ns = 200 r.p.m. W = 257N μ = 38cP			
N_L	ψ°	f	ε	N_L	ψ°	f	ε
50	43	.93	.94	50	35	.77	.87
100	2	∞	1.0	100	-1	∞	.97
150	-9	.93	.94	150	-17	.77	.89
200	-19	.47	.91	200	-32	.38	.84
250	-31	.31	.84	250	-38	.26	.79
-50	53	.31	.82	-50	55	.26	.74
-100	55	.23	.77	-100	59	.19	.68
-150	56	.19	.71	-150	53	.15	.61
-200	64	.16	.64	-200	59	.13	.58
-250	65	.13	.61	-250	46	.11	.56
0	54	.47	.91	0	45	.38	.84

Rotating load with rotating shaft p_{end} = 10KN/m² A8

Ns = 200 r.p.m. W = 198N μ = 36cP				Ns = 200 r.p.m. W = 154N μ = 36cP			
N_L	ψ°	f	ε	N_L	ψ°	f	ε
50	53	.62	.82	50	51	.63	.81
100	0	∞	1.0	100	2	∞	1.0
150	-26	.62	.82	150	-45	.63	.82
200	-39	.31	.72	200	-54	.31	.76
250	-39	.21	.66	250	-57	.21	.68
-50	77	.21	.66	-50	79	.21	.66
-100	86	.16	.61	0	59	.31	.71
-150	77	.12	.58				
-200	88	.10	.56				
-250	84	.09	.56				
0	62	.31	.76				

Rotating load with rotating shaft $p_{end} = 10KN/m^2$

Ns = 300 r.p.m. W = 344N μ = 30cP				Ns = 300 r.p.m. W = 288N μ = 28cP			
N_L	ψ°	f	ε	N_L	ψ°	f	ε
50	32	.66	.87	50	52	.60	.77
100	34	1.32	.90	100	28	1.20	.87
150	-9	∞	1.0	150	-2	∞	1.0
200	-20	1.32	.90	200	-30	1.20	.87
250	-35	.66	.86	250	-33	.60	.77
-50	38	.33	.77	-50	52	.30	.72
-100	33	.26	.76	-100	48	.24	.69
-150	36	.22	.69	-150	59	.20	.66
-200	39	.19	.66	-200	63	.17	.64
-250	36	.17	.64	-250	65	.15	.62
0	38	.44	.82	0	56	.40	.74

Rotating load with rotating shaft $p_{end} = 10KN/m^2$ A10

Ns = 300 r.p.m. W = 228N μ = 28cP				Ns = 300 r.p.m. W = 168N μ = 35cP			
N_L	ψ°	f	ε	N_L	ψ°	f	ε
50	51	.47	.82	50	66	.28	.77
100	34	.95	.85	100	49	.56	.81
150	-8	∞	1.0	150	3	∞	1.0
200	-24	.95	.87	200	-31	.56	.79
250	-36	.47	.82	250	-37	.28	.76
-50	61	.24	.76	-50	34	.14	.68
-100	73	.19	.72	-100	81	.11	.64
-150	65	.16	.69	-150	64	.09	.61
-200	79	.14	.66	-200	83	.08	.59
-250	74	.12	.64	-250	—	—	—
0	60	.32	.79	0	72	.19	.74

Rotating load with rotating shaft $p_{end} = 10KN/m^2$

Ns = 400 r.p.m. W = 344N μ = 23cP				Ns = 400 r.p.m. W = 288N μ = 23cP			
N_L	ψ°	f	ε	N_L	ψ°	f	ε
50	50	.57	.91	50	58	.48	.84
100	38	.86	.94	100	45	.72	.89
150	28	1.71	.95	150	30	1.4	.94
200	-1	∞	1.0	200	-4	∞	1.0
250	-19	1.71	.95	250	-26	1.4	.94
-50	44	.34	.77	-50	55	.29	.74
-100	49	.29	.72	-100	62	.24	.69
-150	54	.24	.69	-150	60	.20	.66
-200	50	.21	.66	-200	62	.18	.63
-250	55	.19	.64	-250	60	.16	.61
0	51	.42	.87	0	52	.36	.79

Rotating load with rotating shaft p_{end} = 10KN/m^2 A12

Ns = 400 r.p.m. W = 228N μ = 23cP				Ns = 400 r.p.m. W = 168N μ = 23cP			
N_L	ψ°	f	ε	N_L	ψ°	f	ε
50	54	.38	.79	50	68	.28	.74
100	47	.56	.82	100	56	.42	.79
150	31	1.1	.91	150	34	.84	.89
200	-1	∞	1.0	200	-1	∞	1.0
250	-35	1.1	.89	250	-47	.84	.89
-50	57	.23	.64	-50	80	.17	.64
-100	67	.19	.58	-100	65	.14	.61
-150	56	.16	.54	0	—	—	—
-200	77	.14	.51				
-250	66	.13	.49				
0	50	.28	.71				

Rotating load with rotating shaft Pend = 10KN/m² A13

Ns = 500 r.p.m. W = 344N μ = 25cP				Ns = 500 r.p.m. W = 288N μ = 24cP			
N_L	ψ°	f	ε	N_L	ψ°	f	ε
50	40	.39	.77	50	61	.34	.72
100	42	.52	.81	100	53	.46	.77
150	37	.78	.84	150	49	.69	.82
200	29	1.56	.91	200	29	1.40	.91
250	9	∞	.97	250	1	∞	.97
-50	40	.26	.72	-50	57	.23	.68
-100	49	.22	.69	-100	64	.19	.64
-150	43	.19	.66	-150	59	.17	.62
-200	48	.17	.64	-200	68	.15	.59
-250	60	.16	.63	-250	69	.13	.57
0	46	.31	.71	0	64	.28	.69

Rotating load with rotating shaft $p_{end} = 10KN/m^2$ A14

Ns = 500 r.p.m. W = 228N μ = 23cP			
N_L	$\psi^\bullet$	f	ε
50	88	.29	.71
100	43	.38	.81
150	37	.58	.87
200	24	1.15	.94
250	0	∞	1.0
-50	61	.19	.64
-100	69	.17	.61
-150	68	.15	.56
-200	78	.13	.53
-250	67	.11	.51
0	54	.23	.67

Ns = 500 r.p.m. W = 168N μ = 23cP			
N_L	$\psi^\bullet$	f	ε
50	61	.21	.71
100	59	.28	.74
150	44	.42	.79
200	37	.84	.88
250	-10	∞	1.0
-50			
-100			
-150			
-200			
-250			
0			

Rotating load with rotating shaft $p_{end} = 10KN/m^2$ A15

Ns = 600 r.p.m. W = 344N μ = 20cP				Ns = 600 r.p.m. W = 288N μ = 20cP			
N_L	ψ°	f	ε	N_L	ψ°	f	ε
50	41	.39	.77	50	42	.35	.74
100	35	.48	.82	100	41	.43	.77
150	38	.65	.87	150	28	.58	.81
200	33	.98	.92	200	24	.87	.86
250	8	1.95	.96	250	22	1.74	.91
-50	62	.28	.76	-50	51	.25	.71
-75	66	.26	.74	-100	64	.22	.68
-150	67	.22	.72	-150	70	.19	.66
-200	72	.20	.71	-200	72	.17	.64
-250	76	.18	.69	-250	74	.16	.63
0	61	.32	.77	0	45	.29	.76

Rotating load with rotating shaft p_{end} = 10KN/m^2 A16

Ns = 600 r.p.m. W = 228N μ = 22cP				Ns = 600 r.p.m. W = 168N μ = 21cP			
N_L	ψ°	f	ε	N_L	ψ°	f	ε
50	57	.24	.77	50	71	.18	.56
100	56	.30	.79	100	58	.22	.66
150	55	.40	.82	150	59	.30	.71
200	52	.60	.87	200	53	.45	.74
250	36	1.19	.94	250	37	.91	.86
-50	60	.17	.72	0	78	.15	.58
-75	56	.16	.71				
75	61	.27	.77				
0	75	.20	.76				

Rotating load with rotating shaft p_{end} = 10KN/m^2 A17

Ns = 700 r.p.m. W = 344N μ = 19cP				Ns = 700 r.p.m. W = 288N μ = 19cP			
N_L	ψ°	f	ε	N_L	ψ°	f	ε
50	49	.36	.79	50	50	.30	.76
100	42	.43	.82	100	46	.36	.79
150	35	.53	.86	150	51	.45	.82
200	31	.71	.89	200	39	.59	.85
250	29	1.06	.91	250	37	.89	.91
-50	42	.27	.72	-50	67	.22	.69
-100	55	.24	.69	-100	64	.20	.66
-150	59	.21	.68	-150	56	.18	.63
-200	54	.19	.66	-200	70	.16	.59
-250	59	.18	.64	-250	63	.15	.58
0	45	.30	.76	0	55	.25	.72

Rotating load with rotating shaft p_{end} = 10KN/m^2 A18

Ns = 700 r.p.m. W = 228N μ = 18cP				Ns = 700 r.p.m. W = 168N μ = 18cP			
N_L	ψ°	f	ε	N_L	ψ°	f	ε
50	64	.24	.71	50	65	.26	.68
100	58	.29	.76	100	56	.31	.71
150	52	.36	.81	150	53	.39	.76
200	32	.48	.86	200	46	.52	.82
250	36	.72	.89	250	31	.78	.87
-50	58	.18	.63	-50	73	.20	.59
-100	60	.16	.59	-100	82	.17	.52
-150	61	.14	.58	-150	76	.16	.49
-200	74	.13	.54	0	74	.22	.64
0	67	.21	.68				

Rotating load with rotating shaft $p_{end} = 10KN/m^2$ A19

Ns = 800 r.p.m. W = 344N μ = 17cP				Ns = 800 r.p.m. W = 288N μ = 17cP			
N_L	ψ°	f	ε	N_L	ψ°	f	ε
50	47	.34	.77	50	52	.29	.77
100	42	.40	.79	100	54	.33	.79
150	38	.47	.81	150	48	.40	.82
200	34	.60	.84	200	27	.50	.84
250	24	.80	.87	250	32	.67	.86
-50	48	.27	.72	-50	60	.22	.74
-100	52	.24	.69	-100	80	.20	.72
-150	52	.22	.68	-150	81	.18	.71
-200	64	.20	.66	-200	81	.17	.69
-250	63	.18	.64	-250	82	.15	.66
0	44	.30	.76	0	67	.25	.76

Rotating load with rotating shaft p_{end} = 10KN/m^2 A20

Ns = 800 r.p.m. W = 228N μ = 17cP				Ns = 800 r.p.m. W = 168N μ = 16cP			
N_L	ψ°	f	ε	N_L	ψ°	f	ε
50	58	.23	.76	50	65	.17	.76
00	49	.26	.77	100	59	.20	.77
150	42	.32	.81	150	53	.24	.81
200	43	.40	.84	200	51	.30	.87
250	34	.52	.86	-50	73	.13	.59
-50	74	.18	.71	-100	83	.12	.56
-100	86	.16	.69	-150	89	.11	.53
-150	90	.14	.64	-200	90	.10	.49
-200	87	.13	.63	0	76	.15	.76
-250	92	.12	.59				
0	71	.20	.74				

Rotating shaft with rotating load $p_{end} = 100KN/m^2$ A21

Ns = 300 r.p.m. W = 344N μ = 32cP				Ns = 300 r.p.m. W = 288N μ = 30cP			
N_L	ψ°	f	ε	N_L	ψ°	f	ε
50	49	.62	.89	50	38	.55	.92
100	32	1.25	.94	100	42	1.10	.95
150	0	∞	1.0	150	1	∞	1.0
200	-1[illegible]	1.25	.92	200	-40	1.10	.94
250	-30	.62	.89	250	-52	.55	.89
-50	52	.31	.82	-50	67	.27	.77
-100	62	.25	.77	-100	79	.22	.69
-150	62	.21	.74	-150	77	.18	.64
-200	73	.18	.69	-200	85	.16	.61
-250	90	.16	.66	-250	71	.14	.58
0	70	.42	.86	0	73	.37	.87

Rotating load with rotating shaft p_{end} = 100KN/m^2 A22

Ns = 300 r.p.m. W = 228N μ = 32cP				Ns = 300 r.p.m. W = 168N μ = 30cP			
N_L	ψ°	f	ε	N_L	ψ°	f	ε
50	66	.41	.86	50	64	.32	.86
100	41	.83	.92	100	47	.64	.92
150	-2	∞	1.0	150	1	∞	1.0
200	-38	.83	.91	200	-35	.64	.91
250	-62	.41	.86	250	-49	.32	.84
-50	64	.21	.63	-50	76	.16	.74
-100	90	.17	.46	-100	84	.13	.66
-150	90	.14	.41	-150	81	.11	.59
-200	90	.12	.38	-200	90	.09	.54
-250	90	.10	.33	-250	90	.08	.51
0	77	.275	.82	0	74	.21	.82

Figures and Plates

White's Experimental Results

(See Reference (2))

Symbol	Frequency of Rotation (Hz)
×	10
+	15
△	20
□	25
◇	30
^	35
v	40
⋈	45
⊹	50

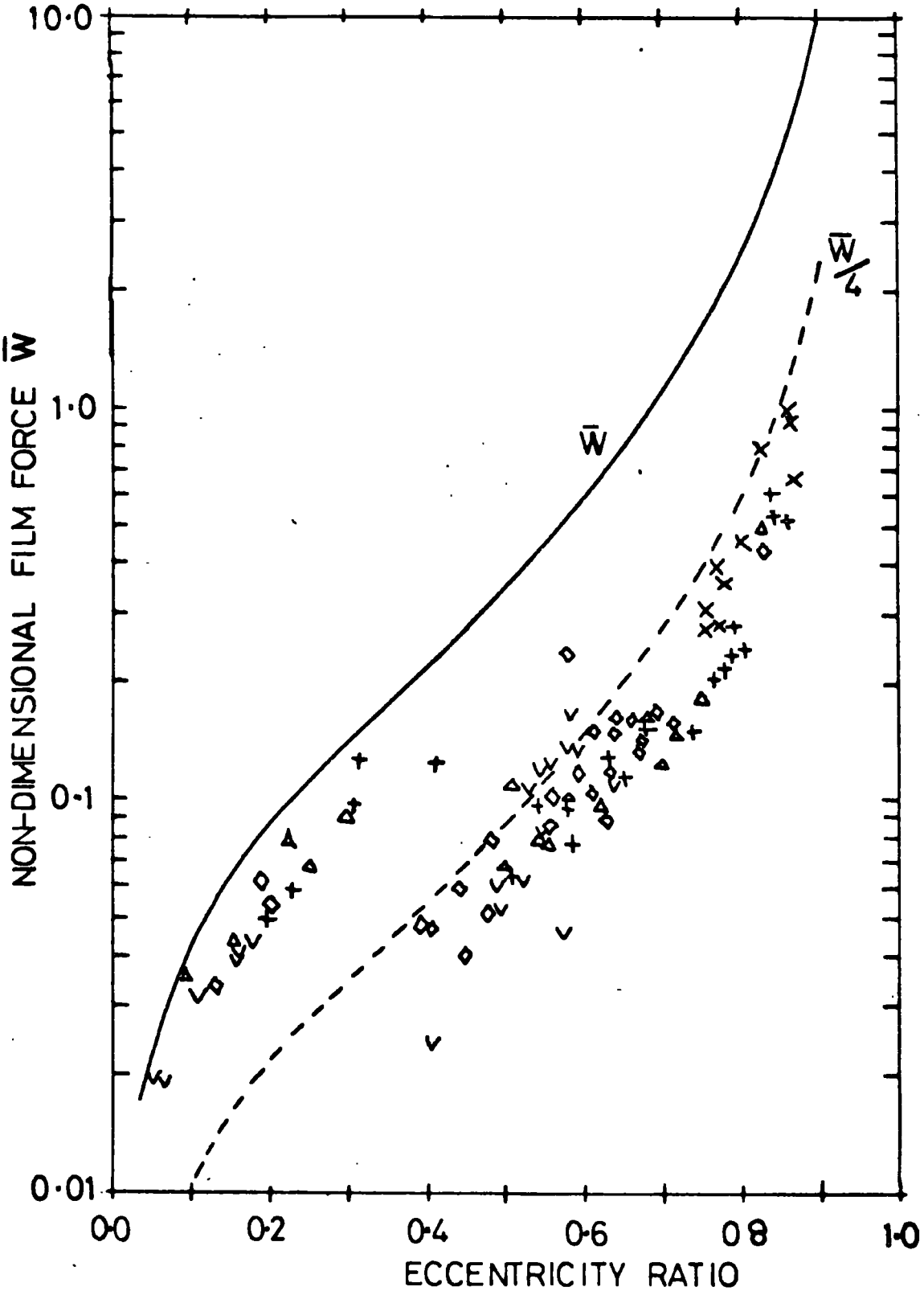

L=25·4mm, R=50·8mm, c=0·086 mm. OIL: TELLUS 27
ONE END FLOODED, THE OTHER OPEN

EXAMPLE OF WHITE'S RESULTS

FIG 2·1

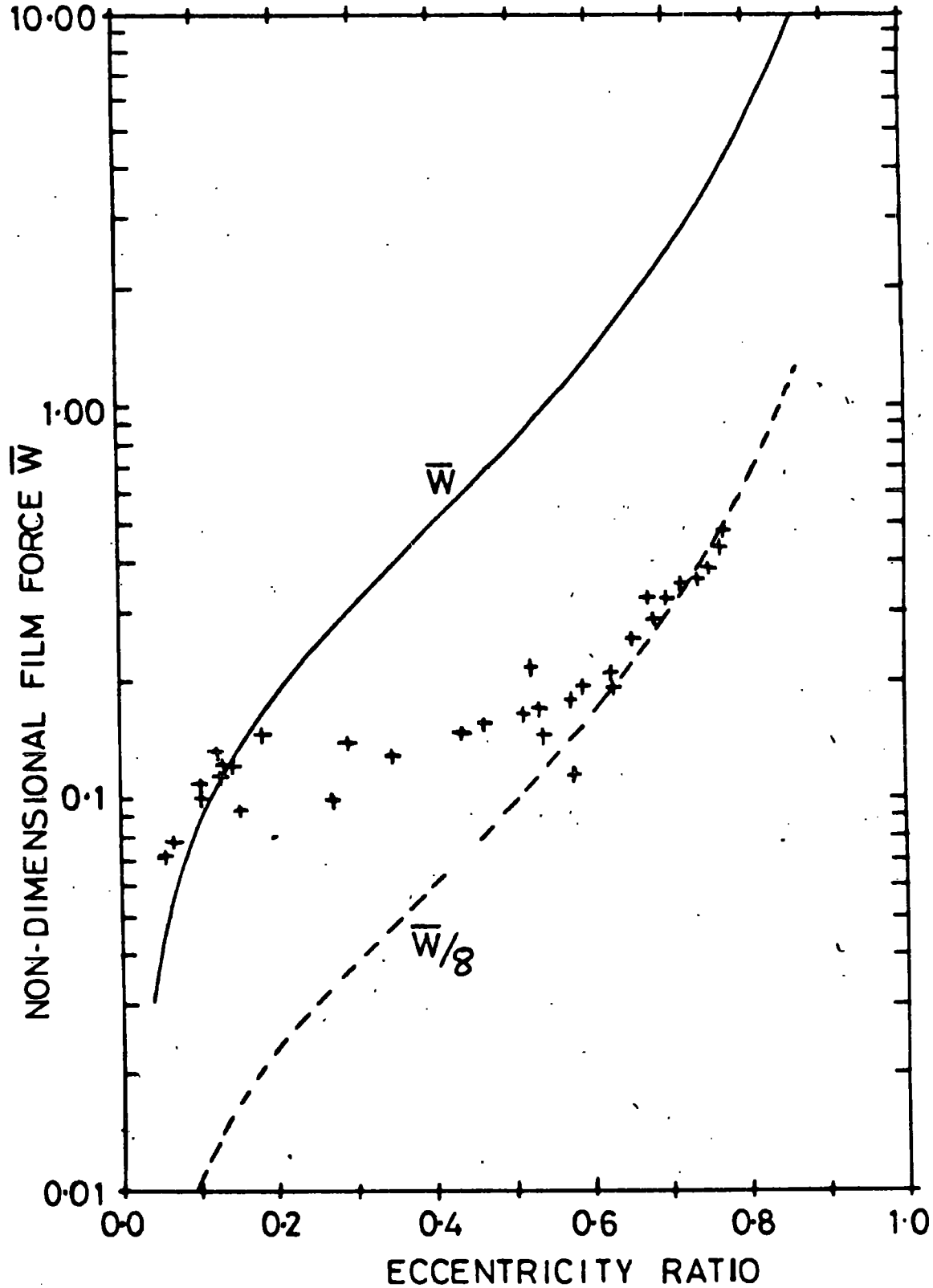

L=38·1mm, R=50·8mm, c=0·0914mm. OIL: TELLUS 27
ONE END FLOODED, THE OTHER SEALED

EXAMPLE OF WHITE'S RESULTS

FIG 2·2

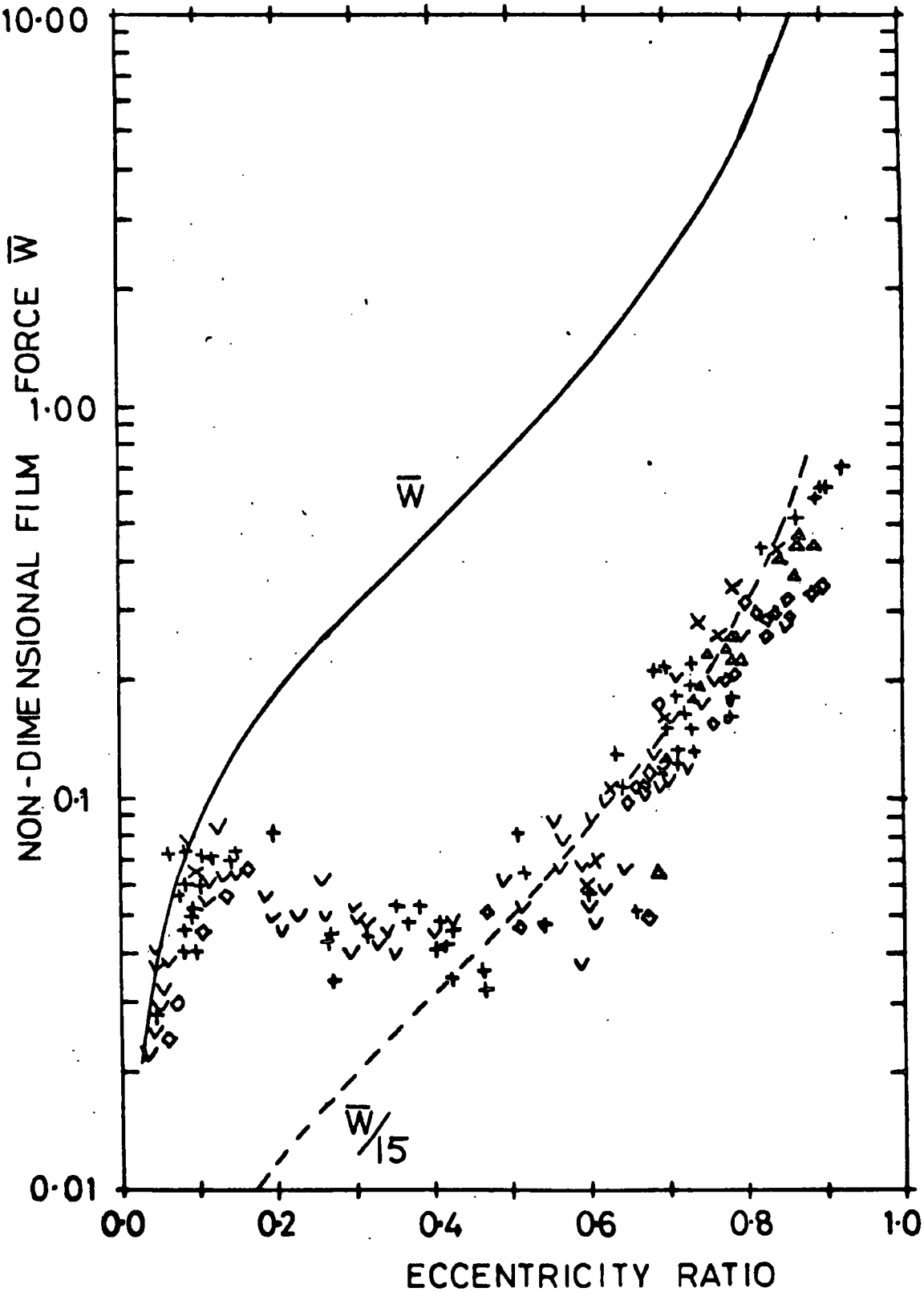

L=38·1 mm, R=50·8mm, c=0·0914mm, OIL: TELLUS 27
ONE END FLOODED, THE OTHER END OPEN

EXAMPLE OF WHITE'S RESULTS

FIG 2·3

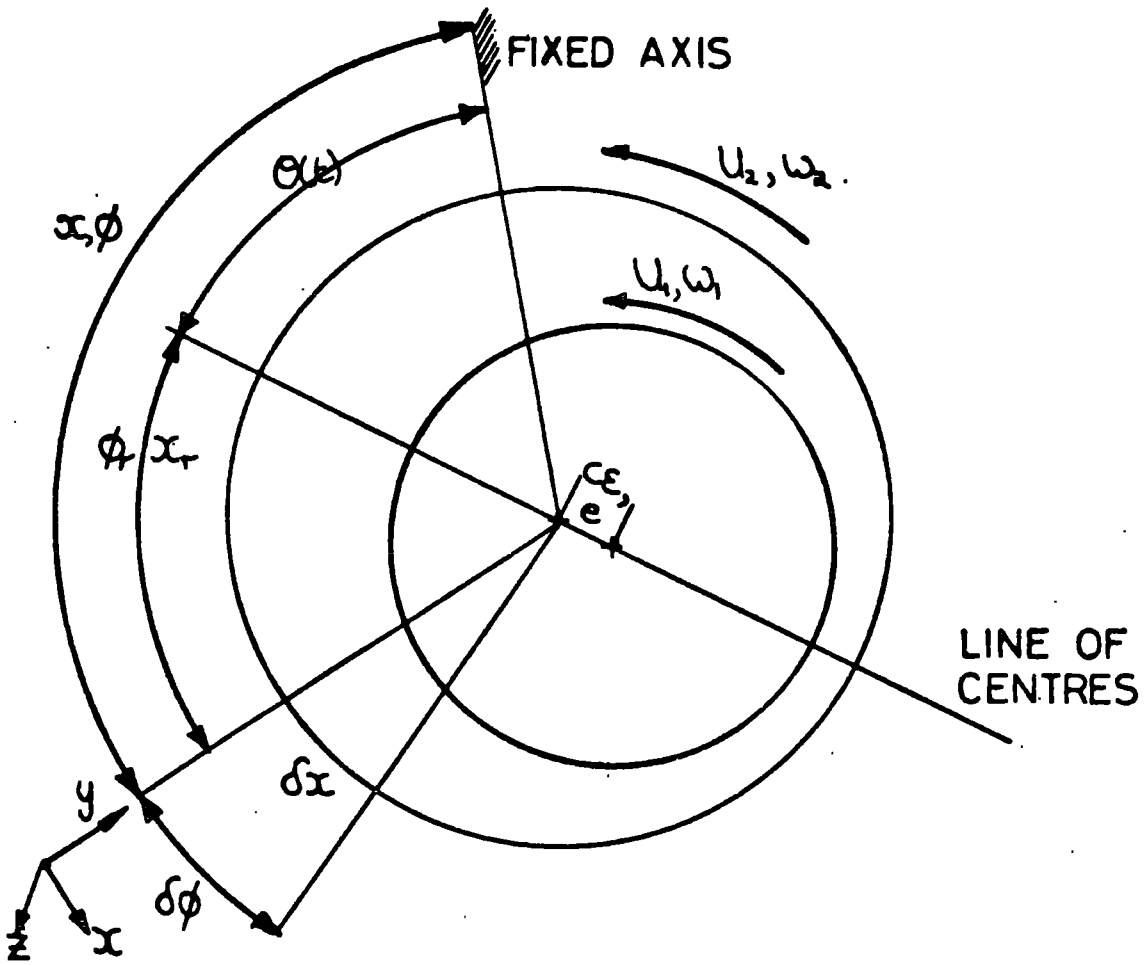

PLAIN JOURNAL BEARING NOTATION

FIG 3·1

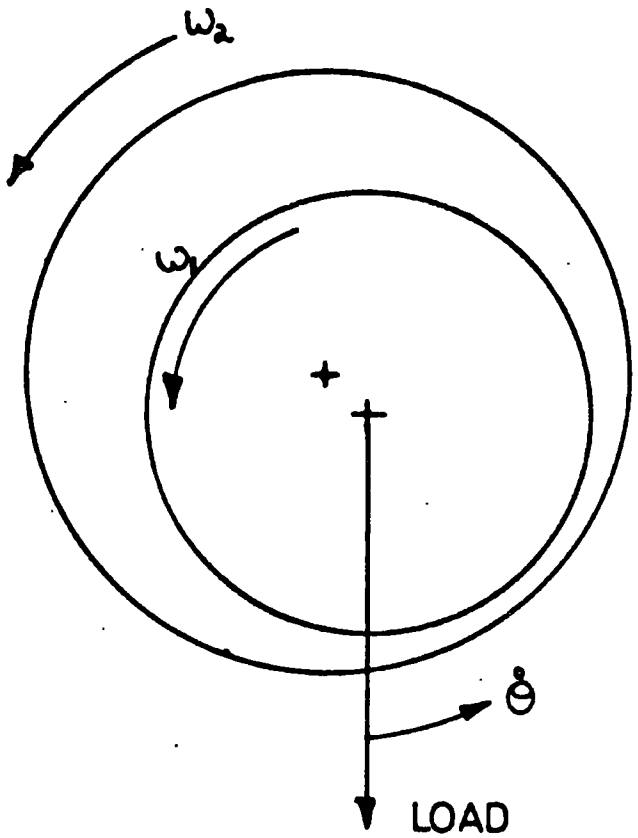

BEARING WITH ROTATING LOAD

FIG 3·2

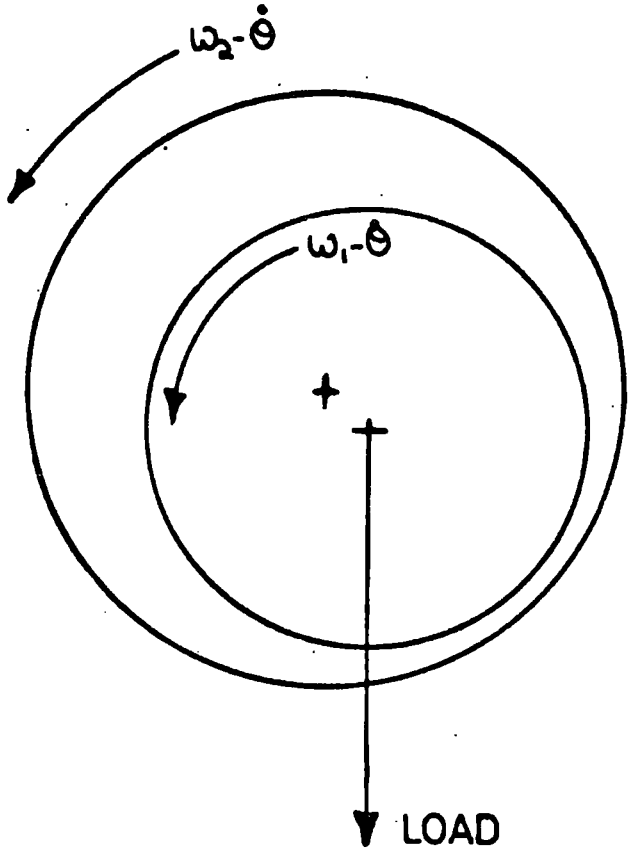

EQUIVALENT STEADILY LOADED BEARING

FIG 3·3

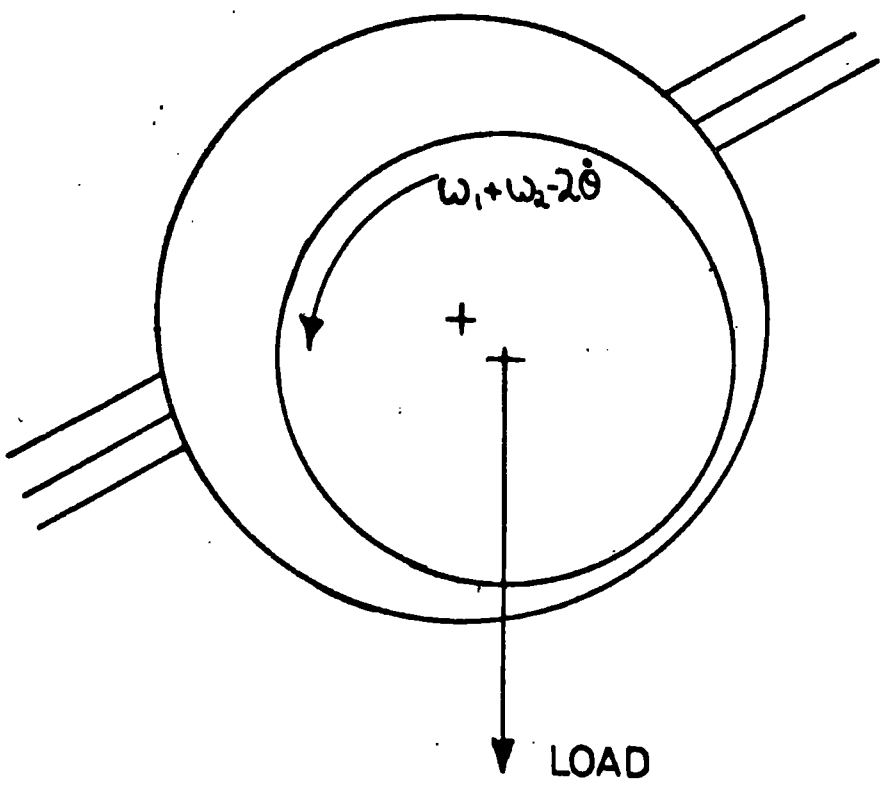

STEADILY LOADED BEARING

FIG 3·4

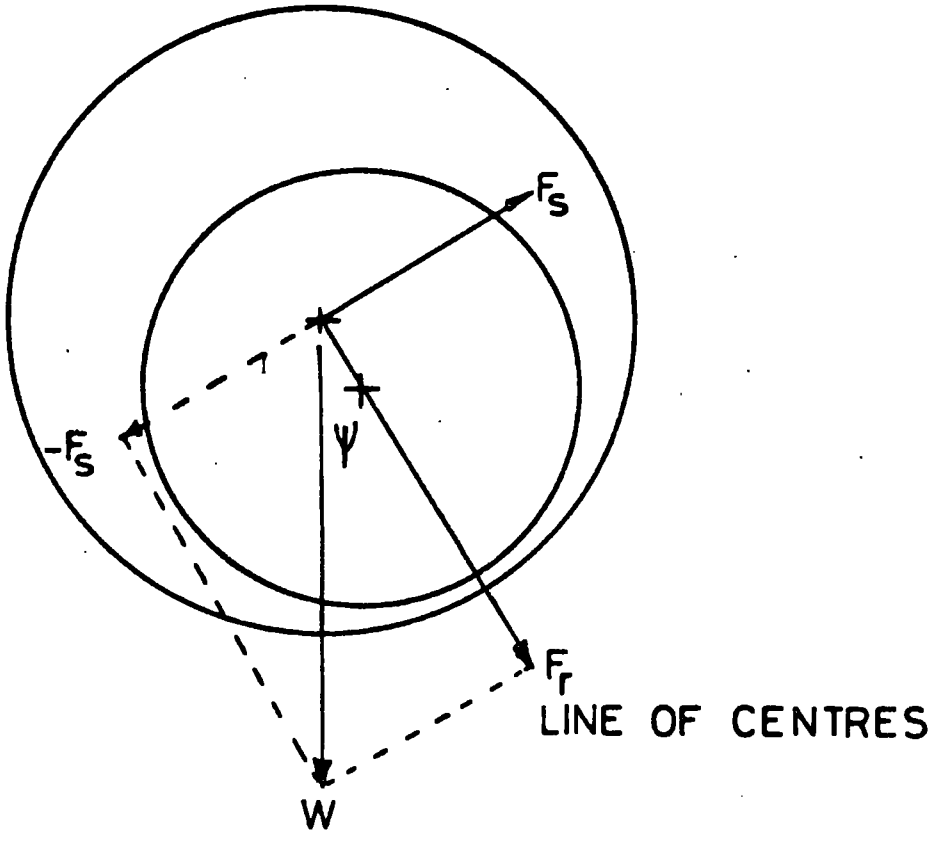

ORTHOGONAL LOADS

FIG 3·5

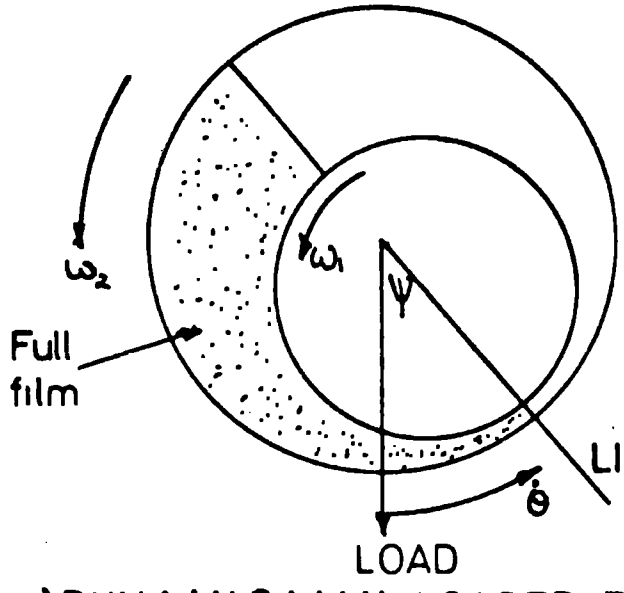

a) DYNAMICALLY LOADED BEARING (LEADING)

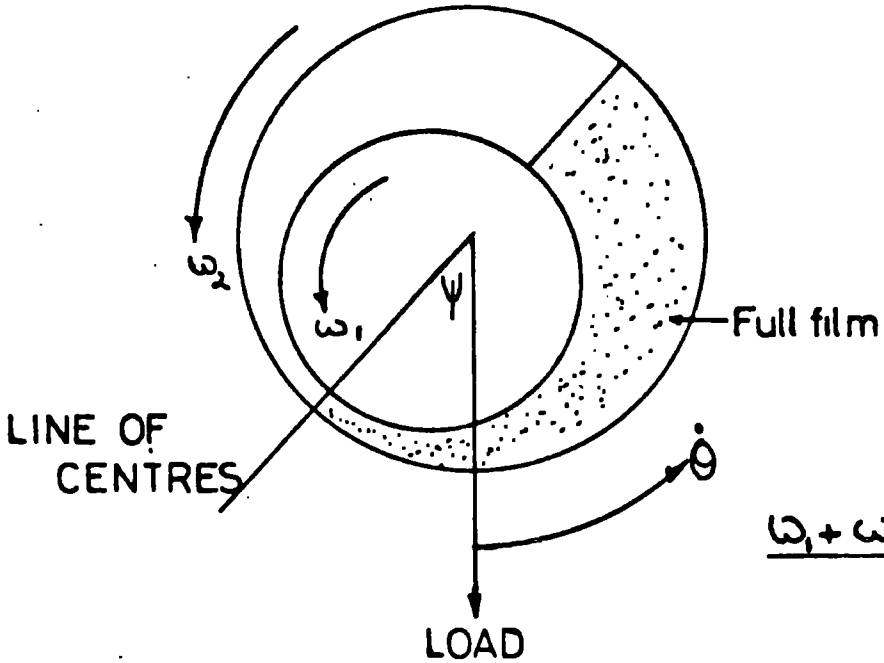

b) DYNAMICALLY LOADED BEARING (LAGGING)

DIFFERENCE IN LOAD ANGLE

FIG 3·6

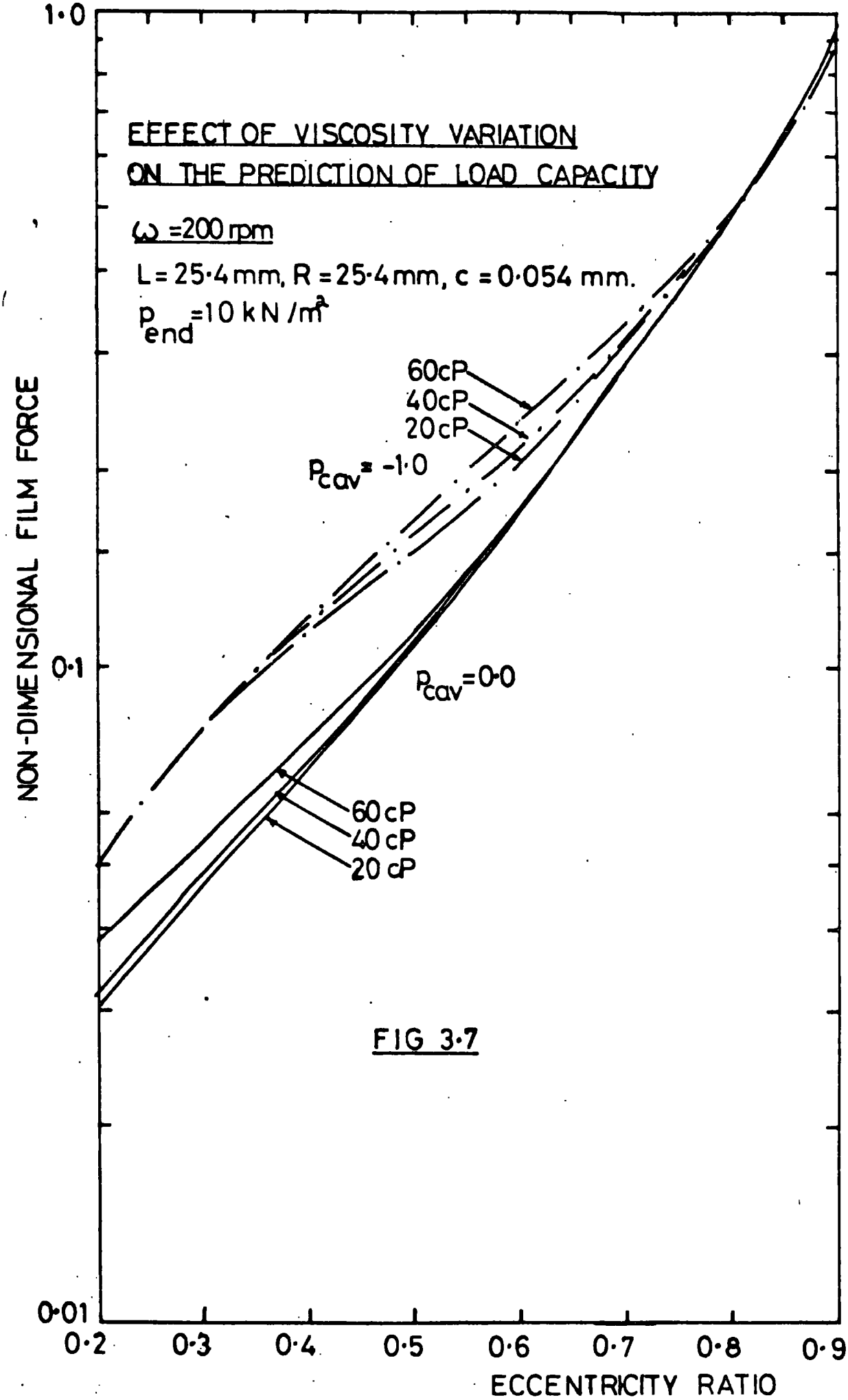
EFFECT OF VISCOSITY VARIATION
ON THE PREDICTION OF LOAD CAPACITY
ω =200 rpm
L = 25·4 mm, R = 25·4 mm, c = 0·054 mm.
p end =10 kN /m²
60cP
40cP
20cP
P cav = -1·0
P cav = 0·0
60 cP
40 cP
20 cP
NON-DIMENSIONAL FILM FORCE
1·0
0·1
0·01
0·2
0·3
0·4
0·5
0·6
0·7
0·8
0·9
ECCENTRICITY RATIO

FIG 3·7

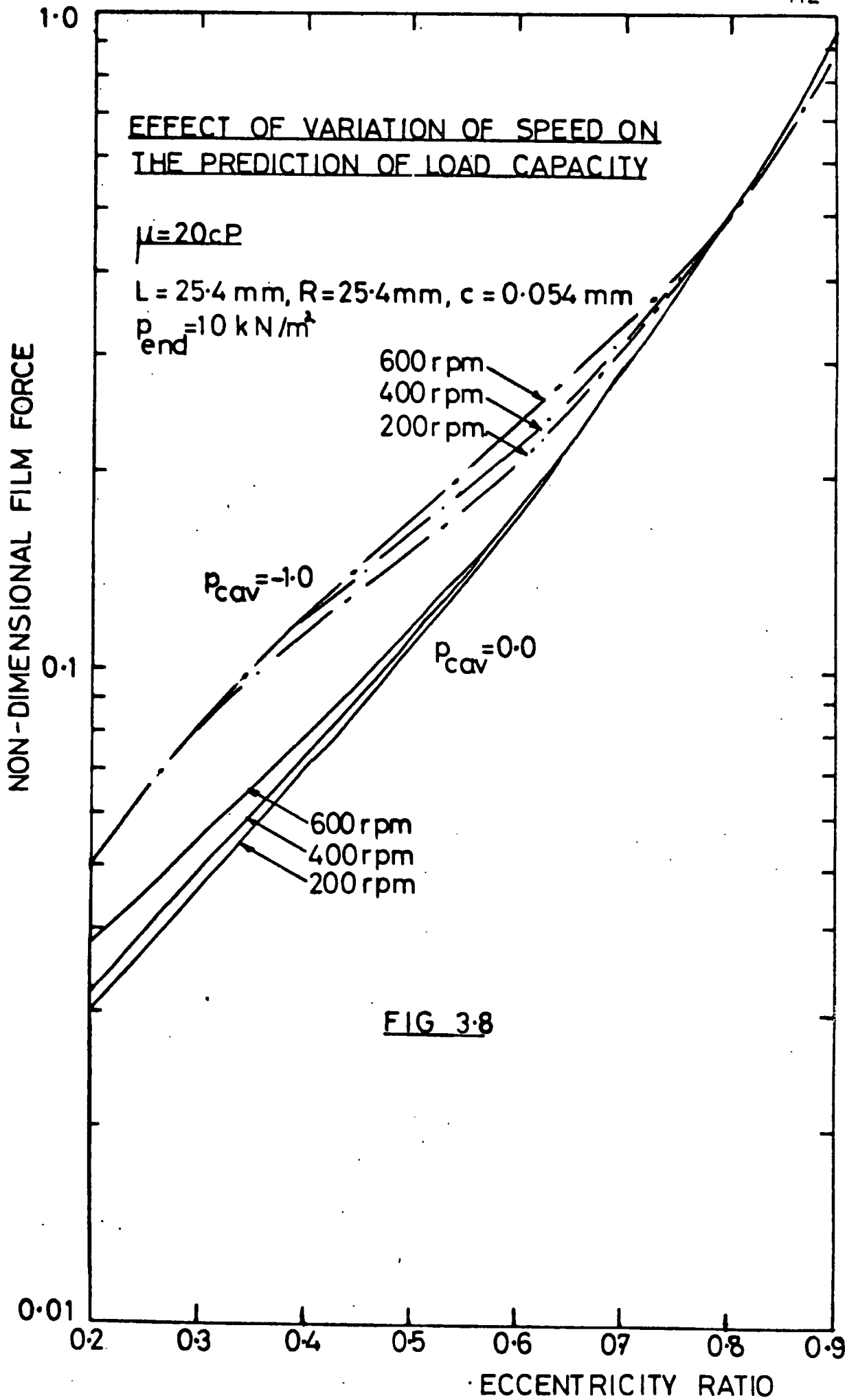
EFFECT OF VARIATION OF SPEED ON THE PREDICTION OF LOAD CAPACITY
μ=20cP
L = 25·4 mm, R=25·4mm, c = 0·054 mm
p_end=10 kN/m²
600 r pm
400 r pm
200 r pm
p_cav=-1·0
p_cav=0·0
600 r pm
400 r pm
200 r pm
NON-DIMENSIONAL FILM FORCE
1·0
0·1
0·01
0·2
0·3
0·4
0·5
0·6
0·7
0·8
0·9
ECCENTRICITY RATIO

FIG 3·8

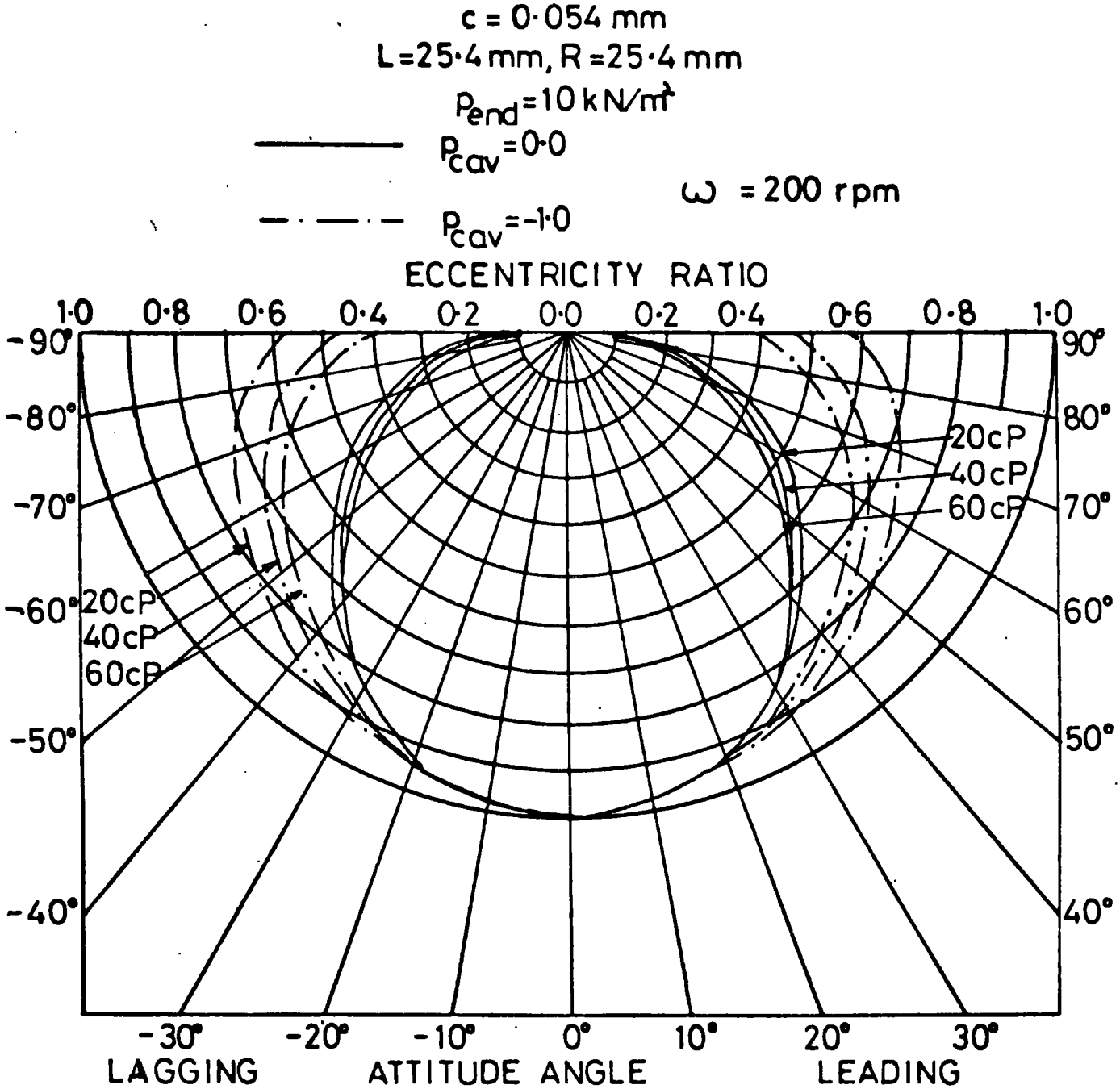

EFFECT OF VARYING VISCOSITY ON LOAD ANGLE PREDICTION

FIG 3·9

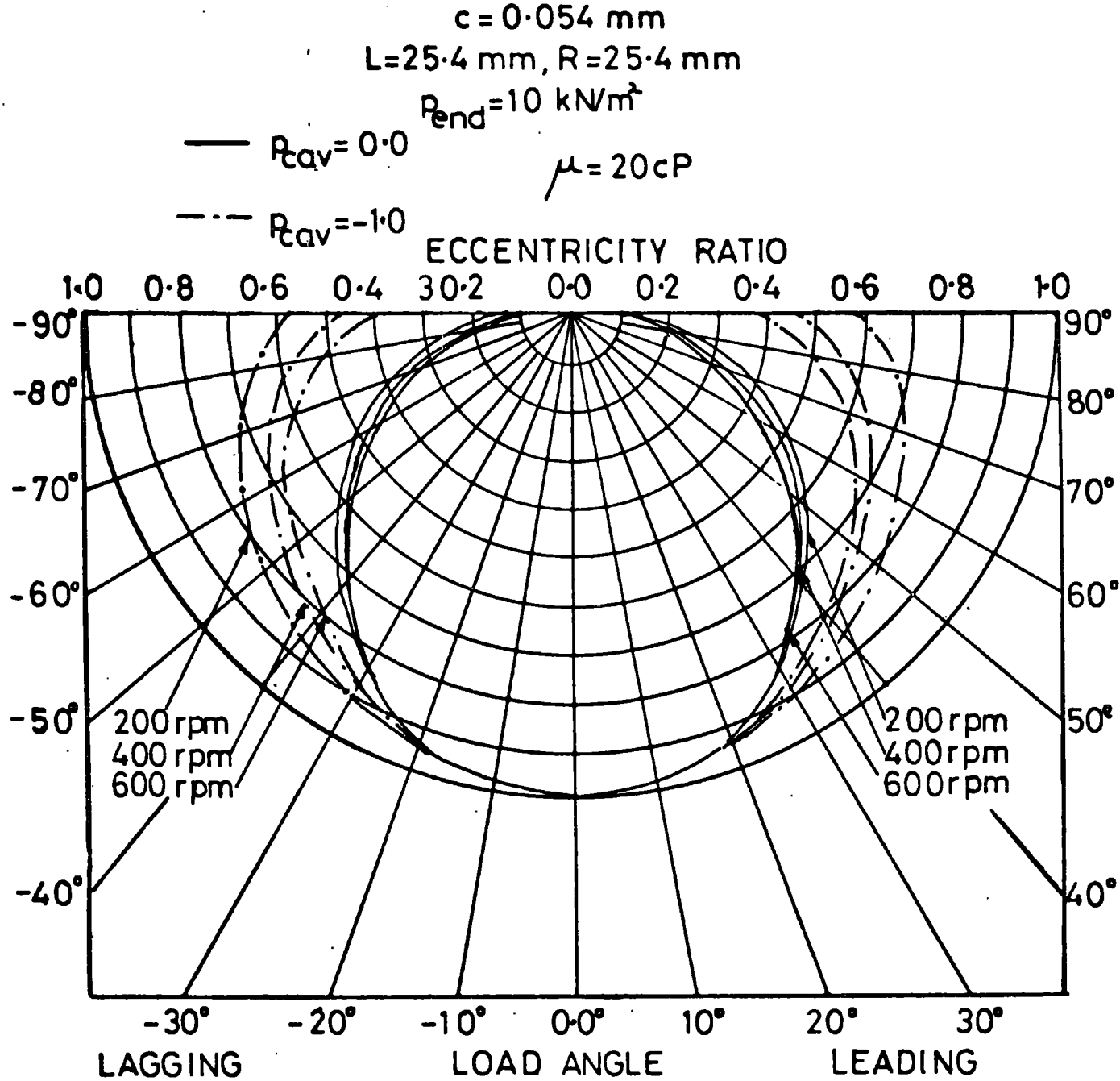

EFFECT OF VARYING SPEED ON LOAD ANGLE PREDICTION

FIG 3·10

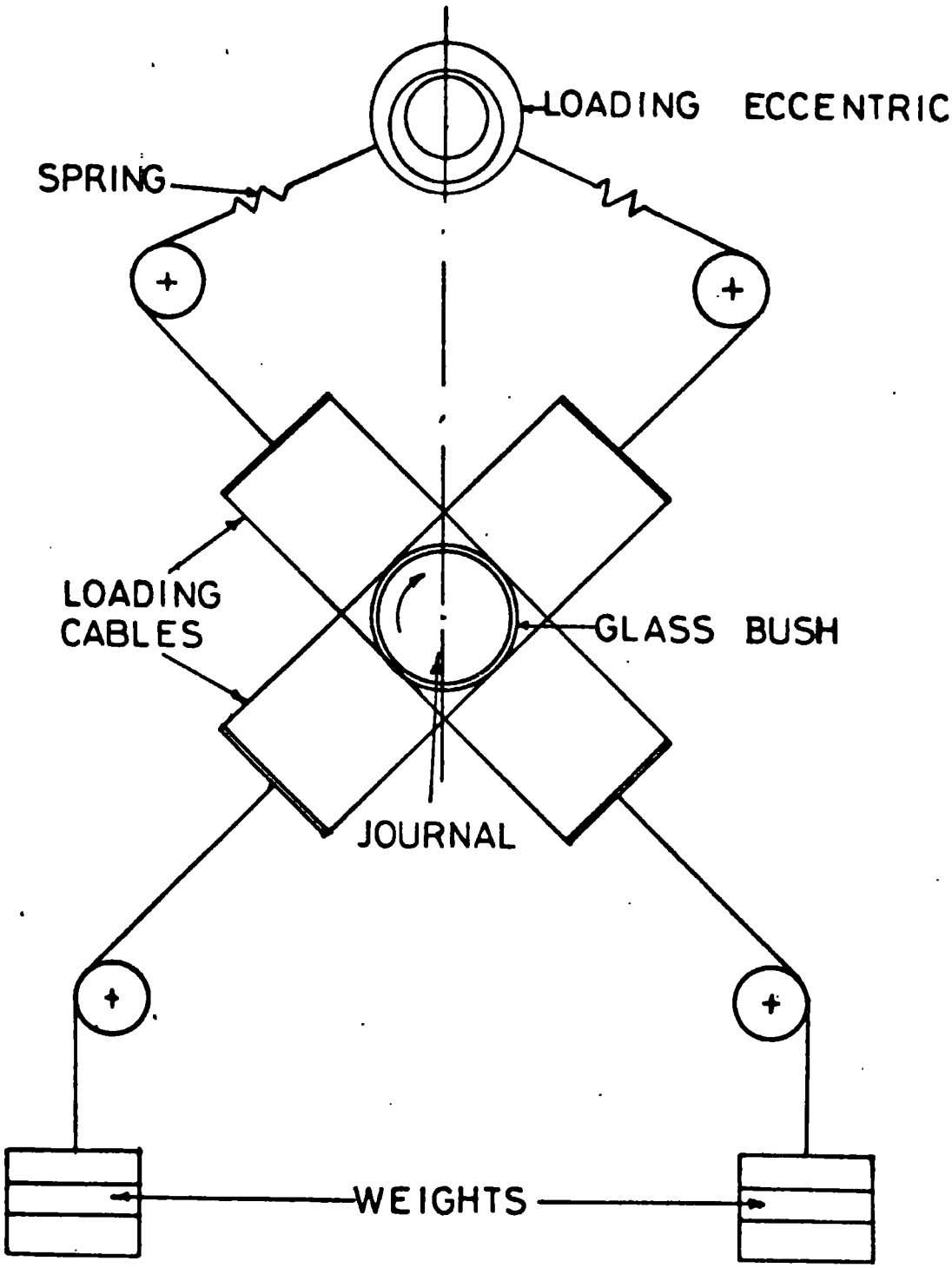

APPARATUS USED BY COLE AND HUGHES

FIG 4·1

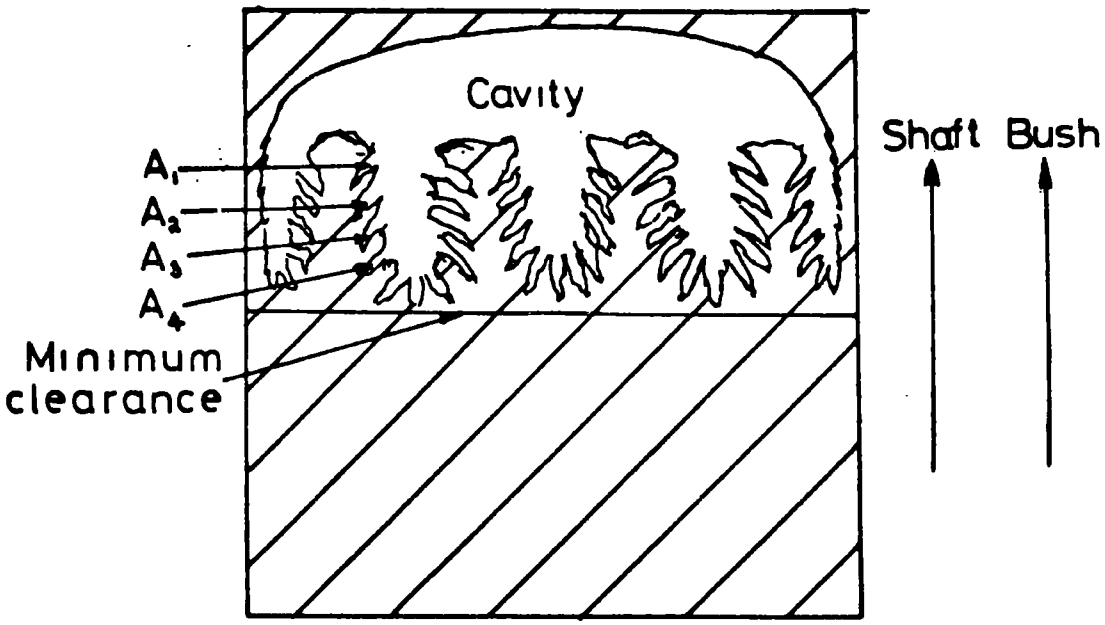

a) Cavity fingers at time t

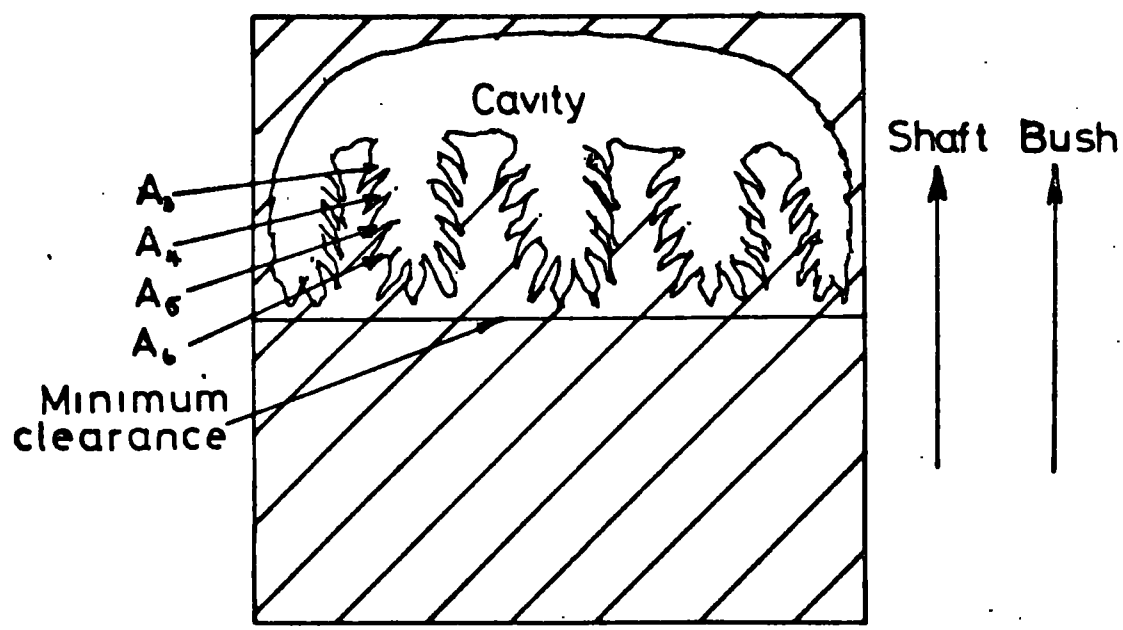

b) Cavity fingers at time t+dt

MOVEMENT IN AIR FINGERS IN CAVITATION REGION

FIG 4·2

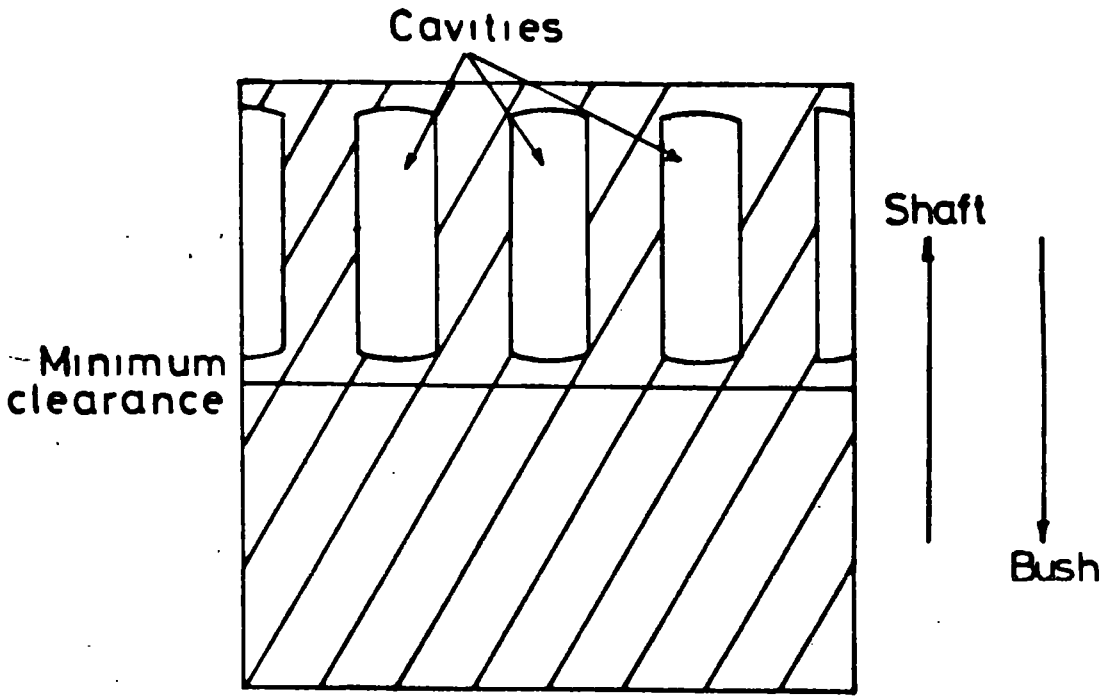

a) $\omega_1 + \omega_2 > 0$

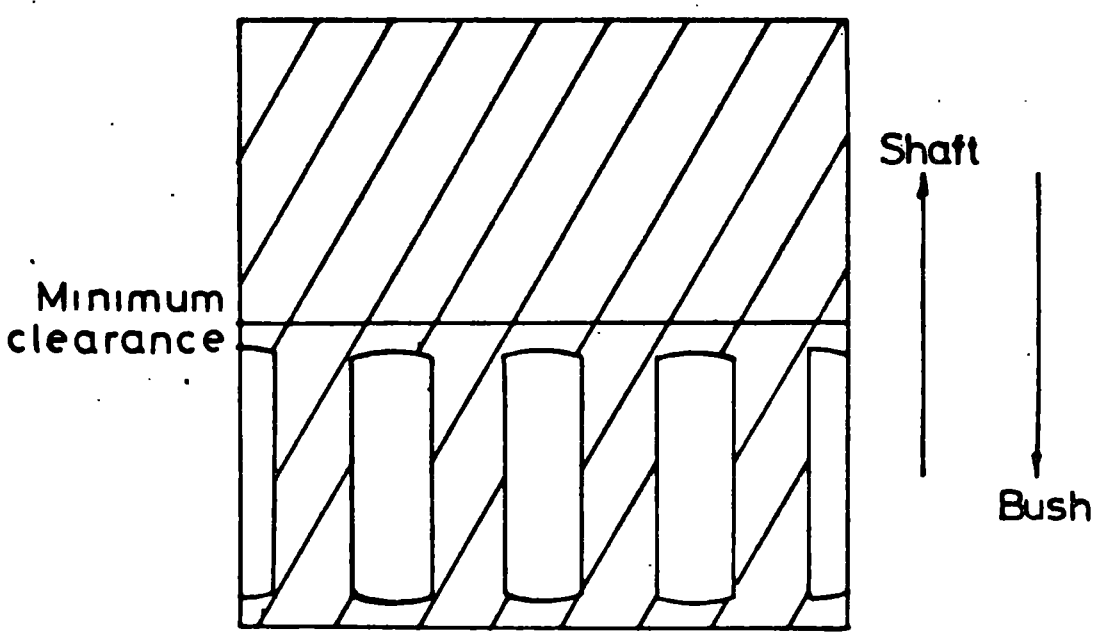

b) $\omega_1 + \omega_2 < 0$

EFFECT OF COMPARATIVE VARIATION OF SHAFT AND BUSH SPEED ON CAVITATION

FIG 4·3

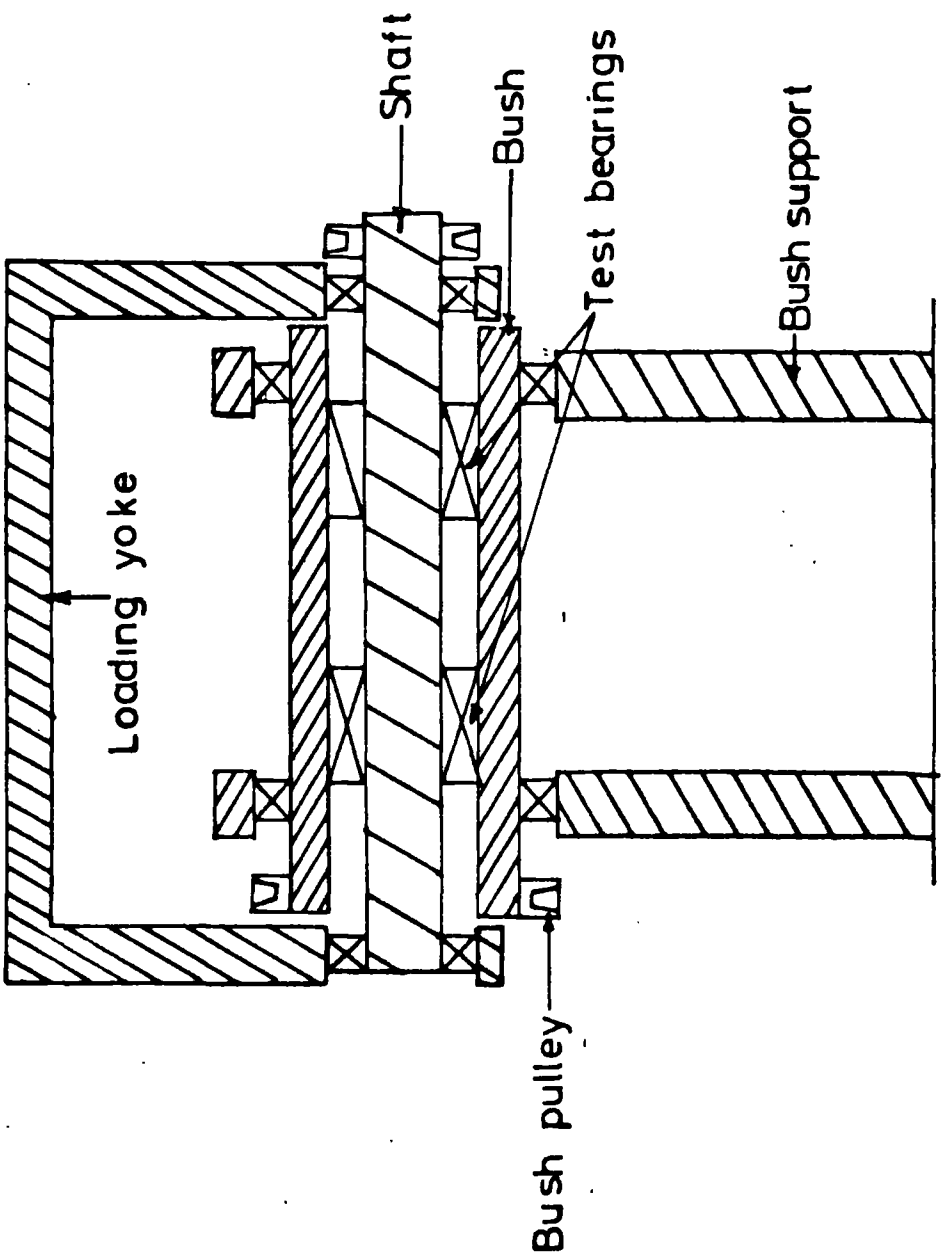

FIG 5:1 DIAGRAMMATIC CROSS-SECTION OF ROTATING SHAFT-ROTATING BUSH DESIGN

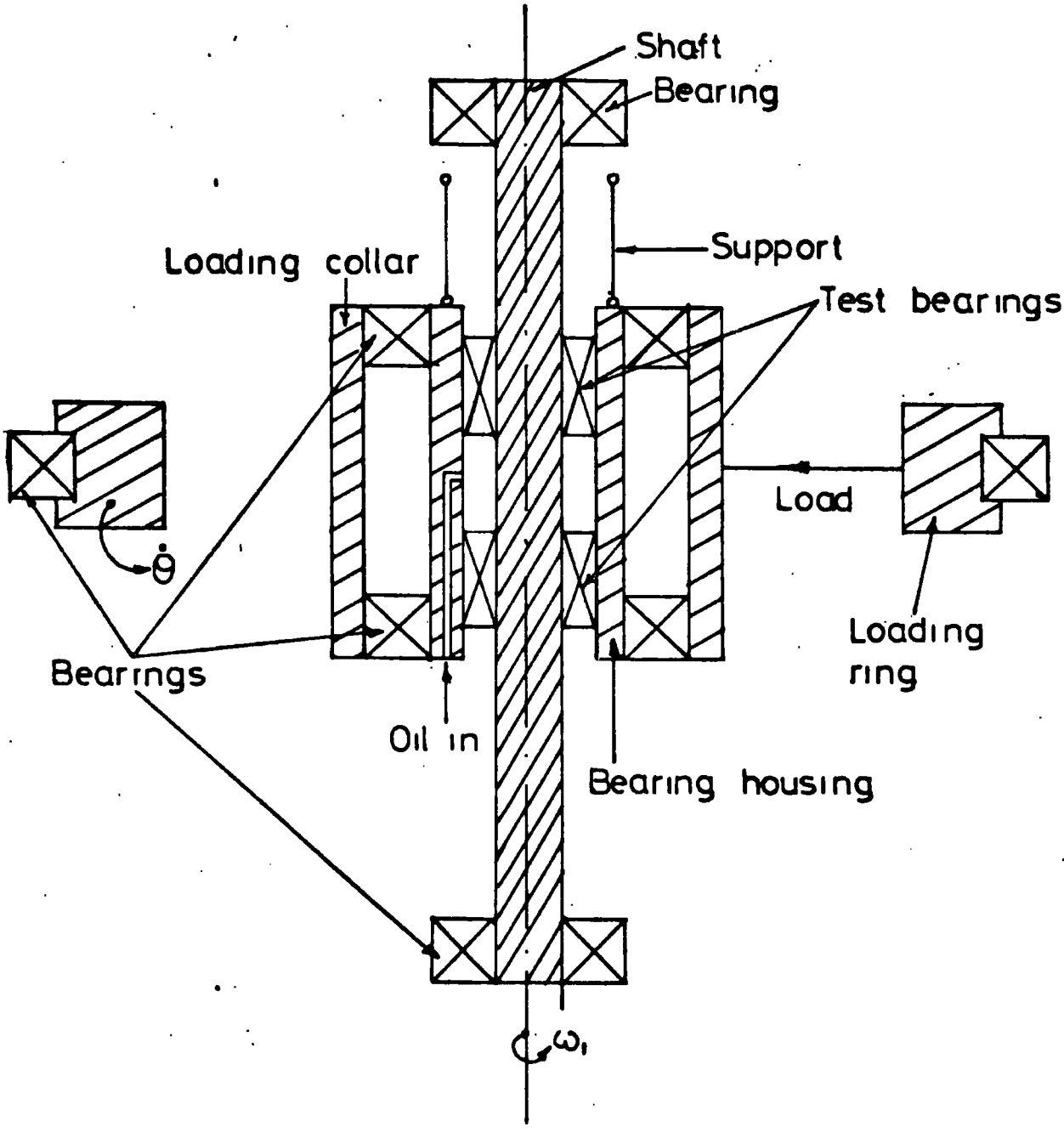

DIAGRAMMATIC CROSS-SECTION OF ROTATING SHAFT-ROTATING LOAD DESIGN

FIG 5·2

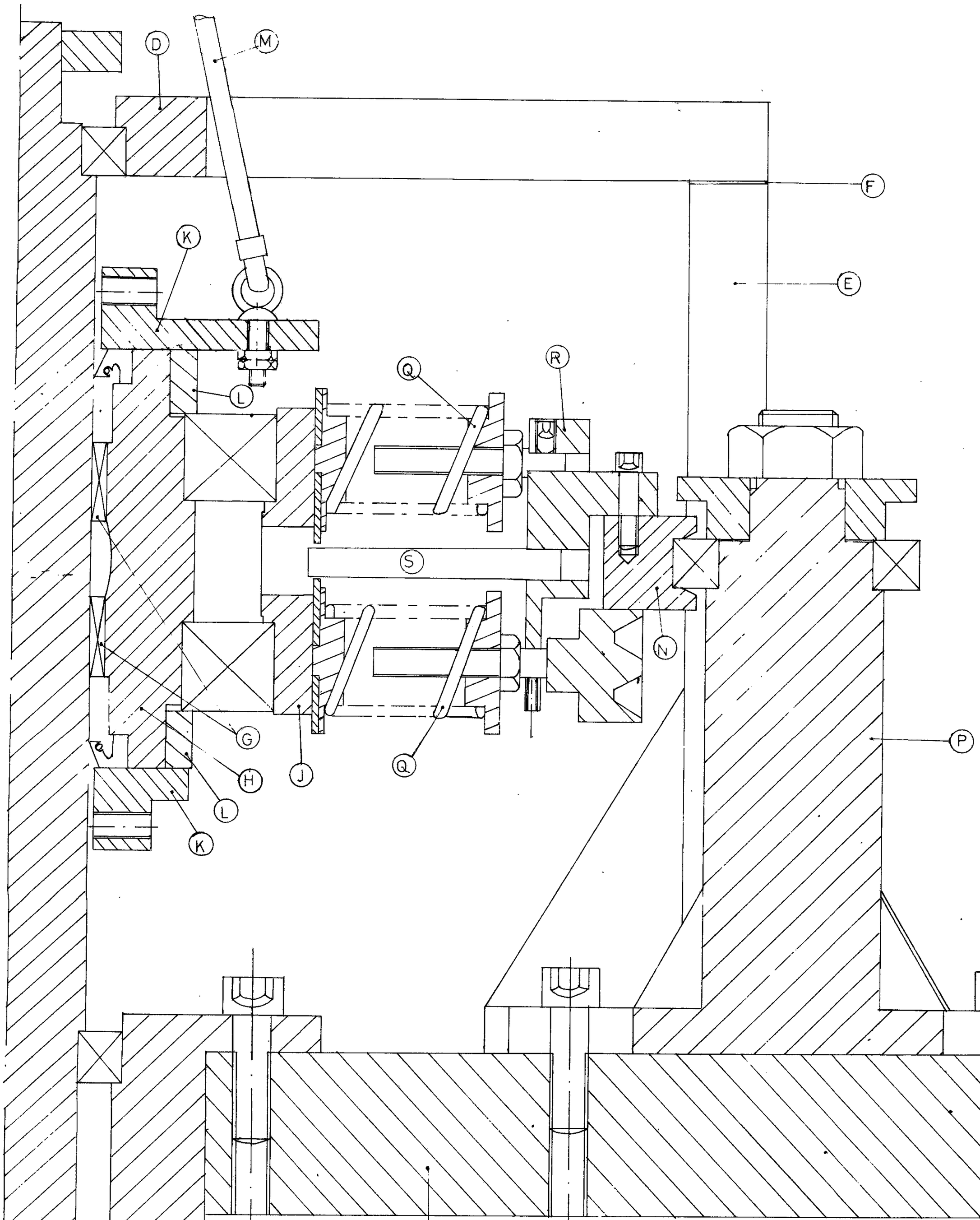

HALF SECTION OF RESEARCH APPARATUS
FULL SIZE

A	SHAFT	K	BEARING END PLATE
B	BASE	L	CLAMPING RING
C	LOWER BEARING HOLDER	M	BOWDEN CABLE
D	UPPER BEARING HOLDER	N	LOADING RING
E	SUPPORT PILLAR	P	SUPPORT PILLAR
F	SHIMS	Q	LOAD SPRING
G	TEST BEARINGS	R	REACTION PLATE
H	BEARING HOUSING	S	DRIVING ROD
J	LOADING COLLAR		

FIG 6·1

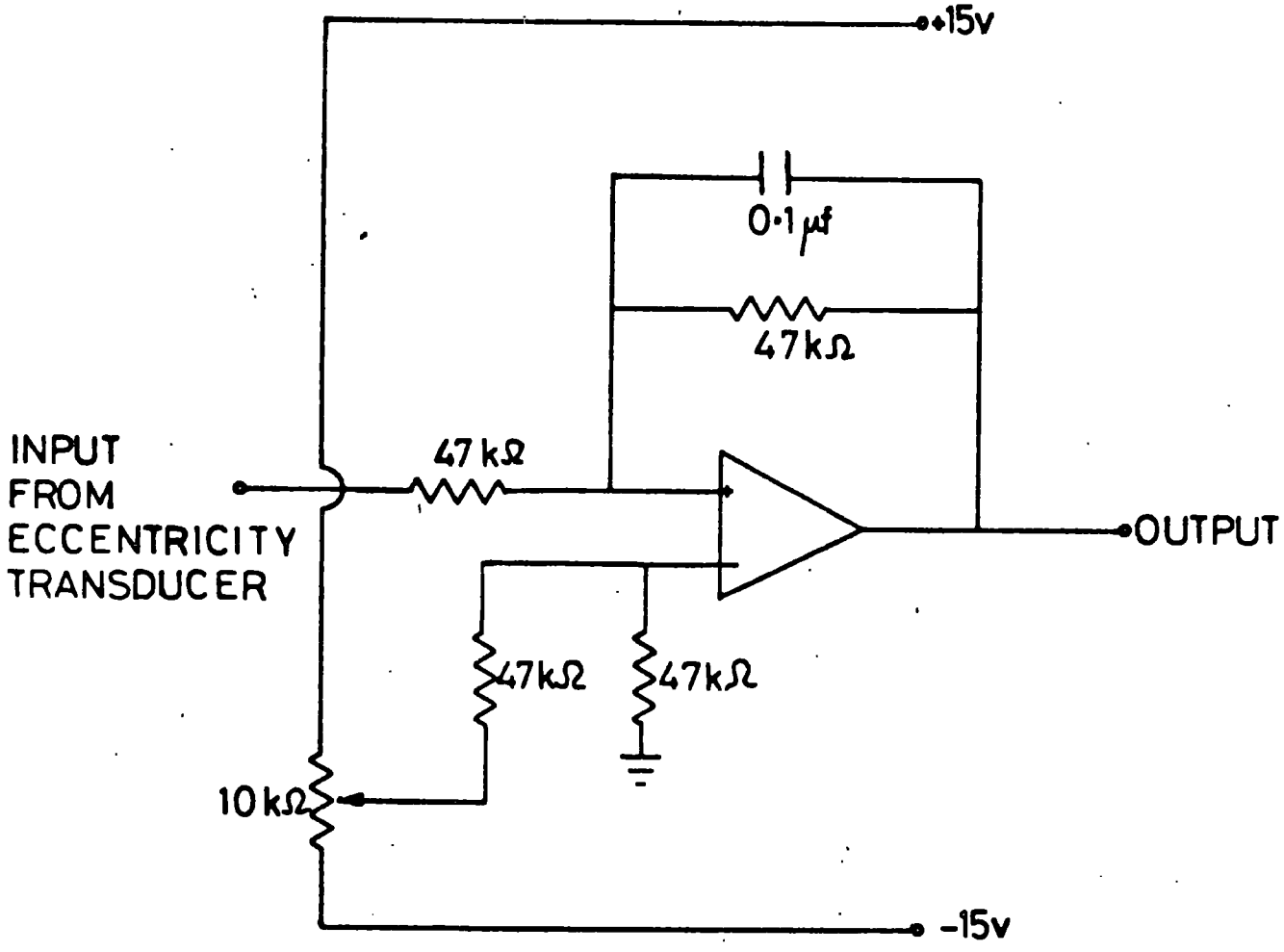

CIRCUIT FOR REDUCTION OF D.C. LEVEL

FIG 6·2

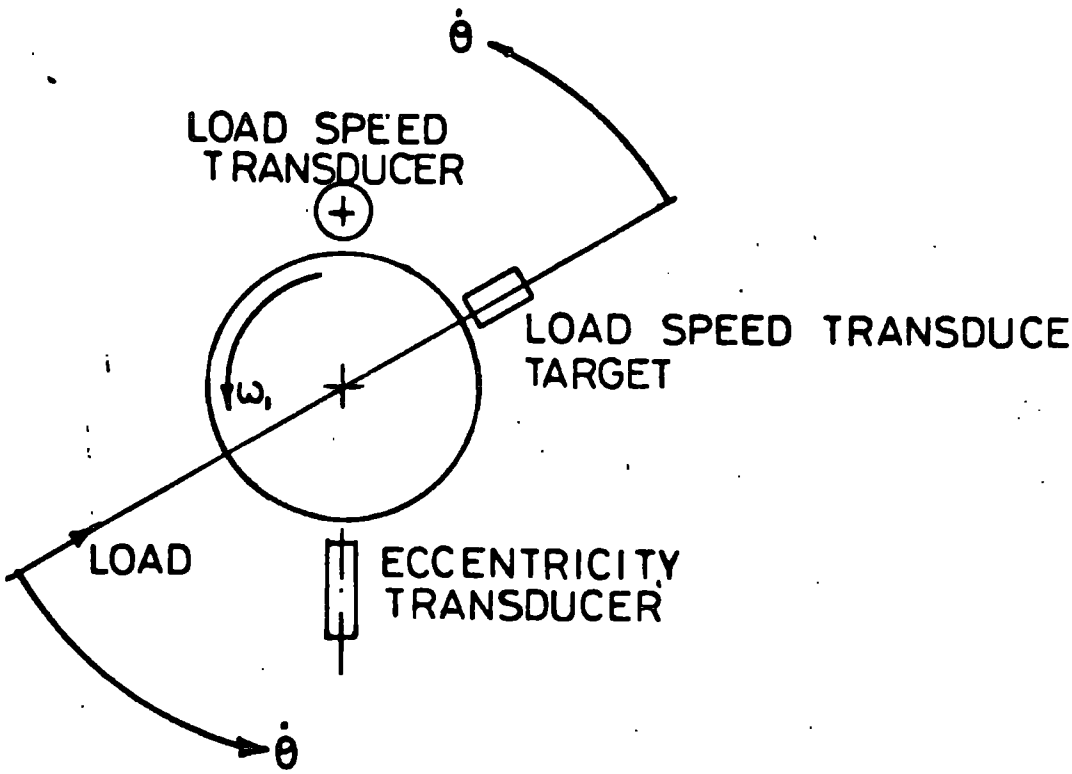

RELATIVE POSITIONS OF TRANSDUCERS USED FOR LOAD ANGLE DETERMINATION

FIG 6·3

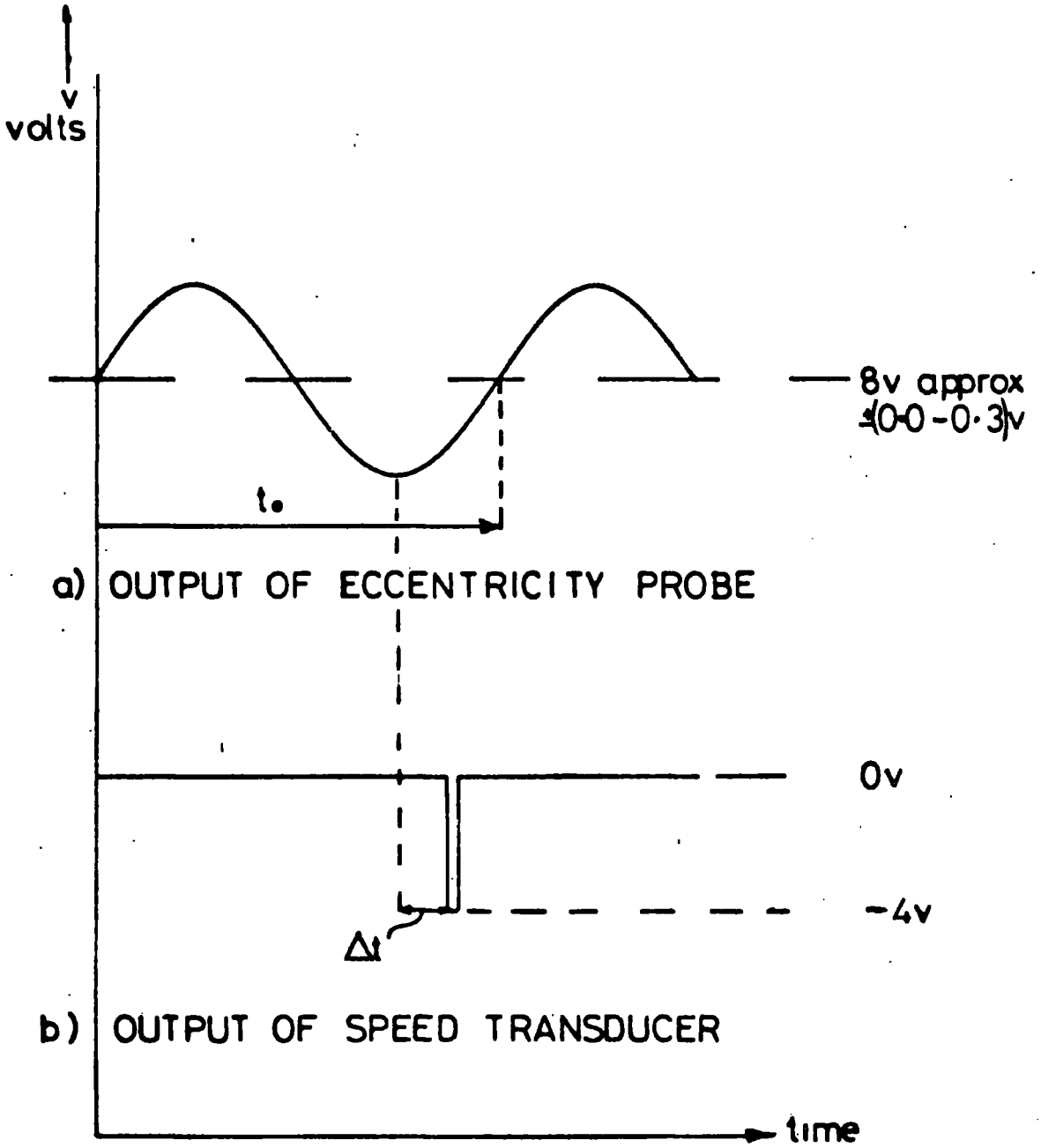

SIGNALS USED FOR DETERMINATION OF LOAD ANGLE

FIG 6·4

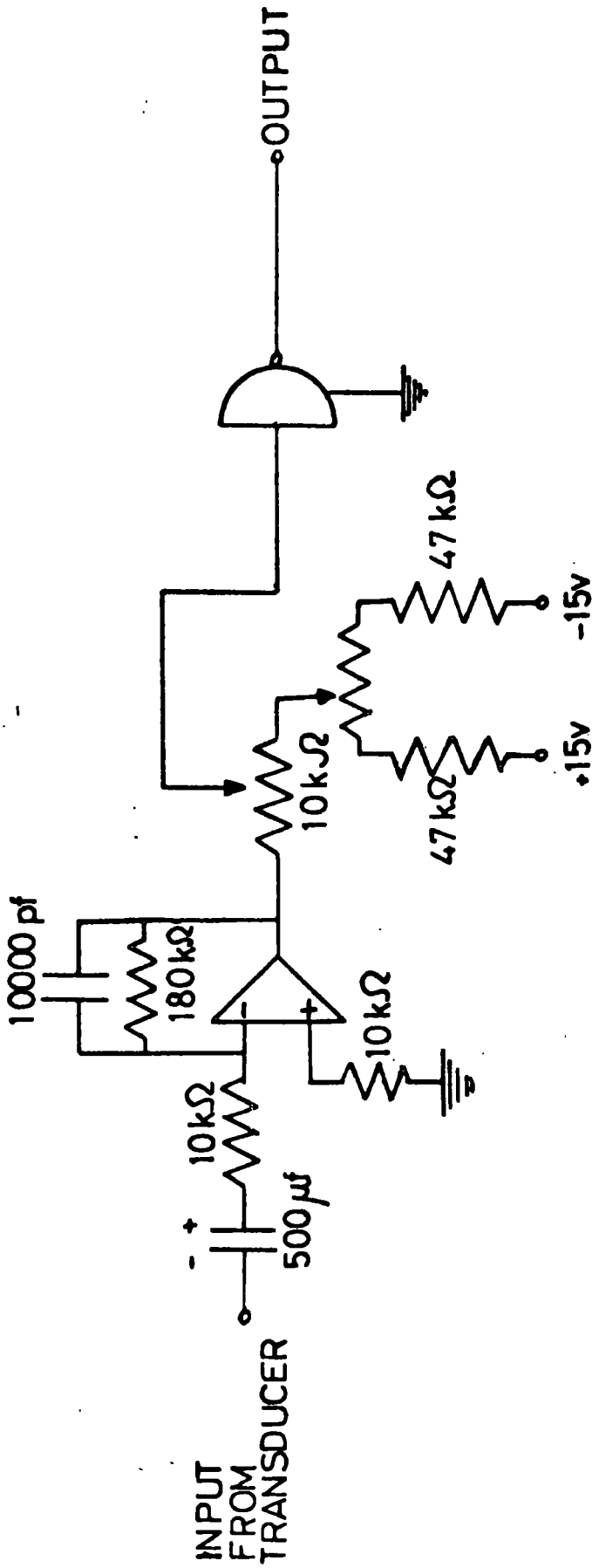

FIG 6·5 CIRCUIT FOR DETERMINATION OF LOAD ANGLE

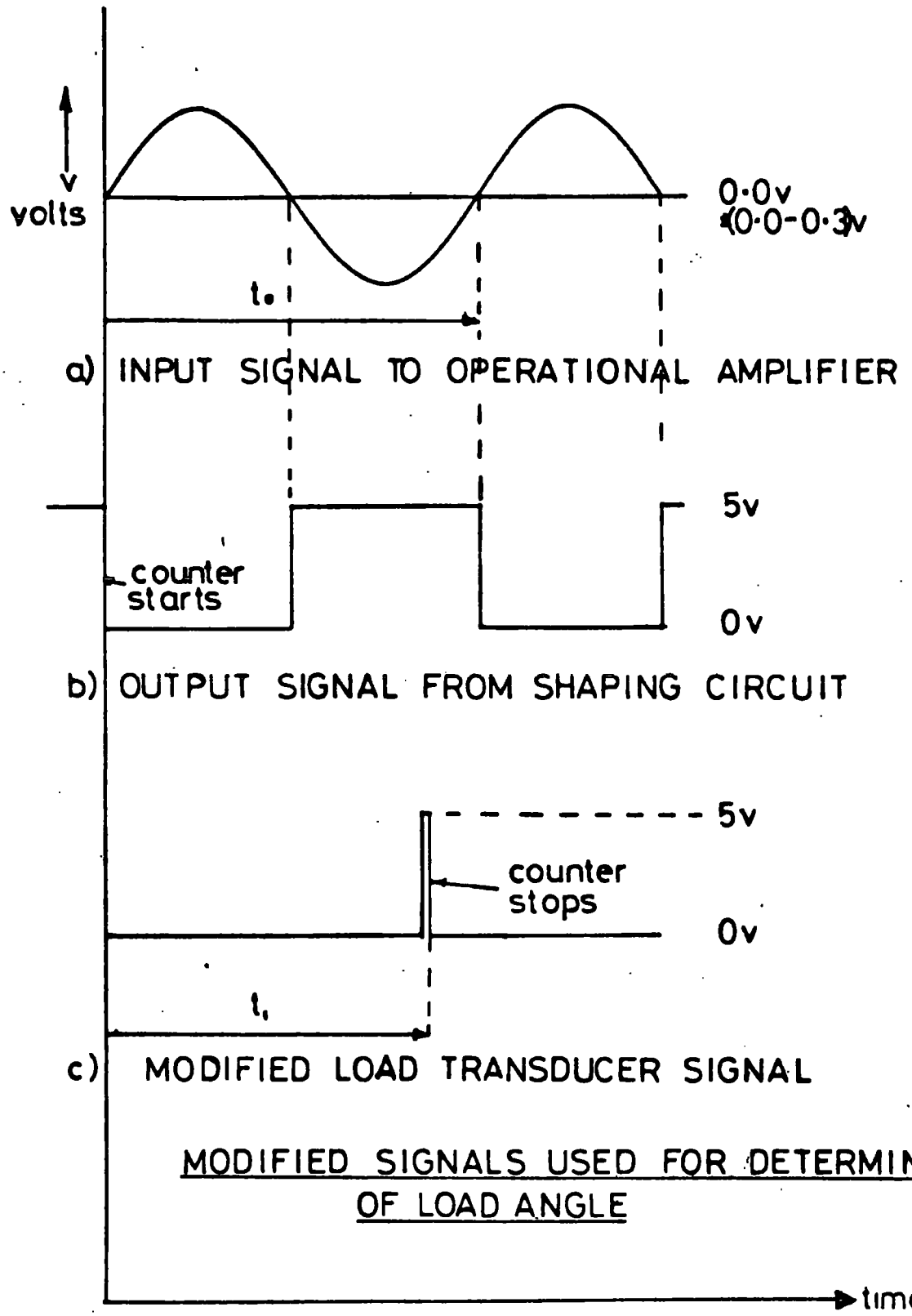

MODIFIED SIGNALS USED FOR DETERMINATION OF LOAD ANGLE

FIG 6·6

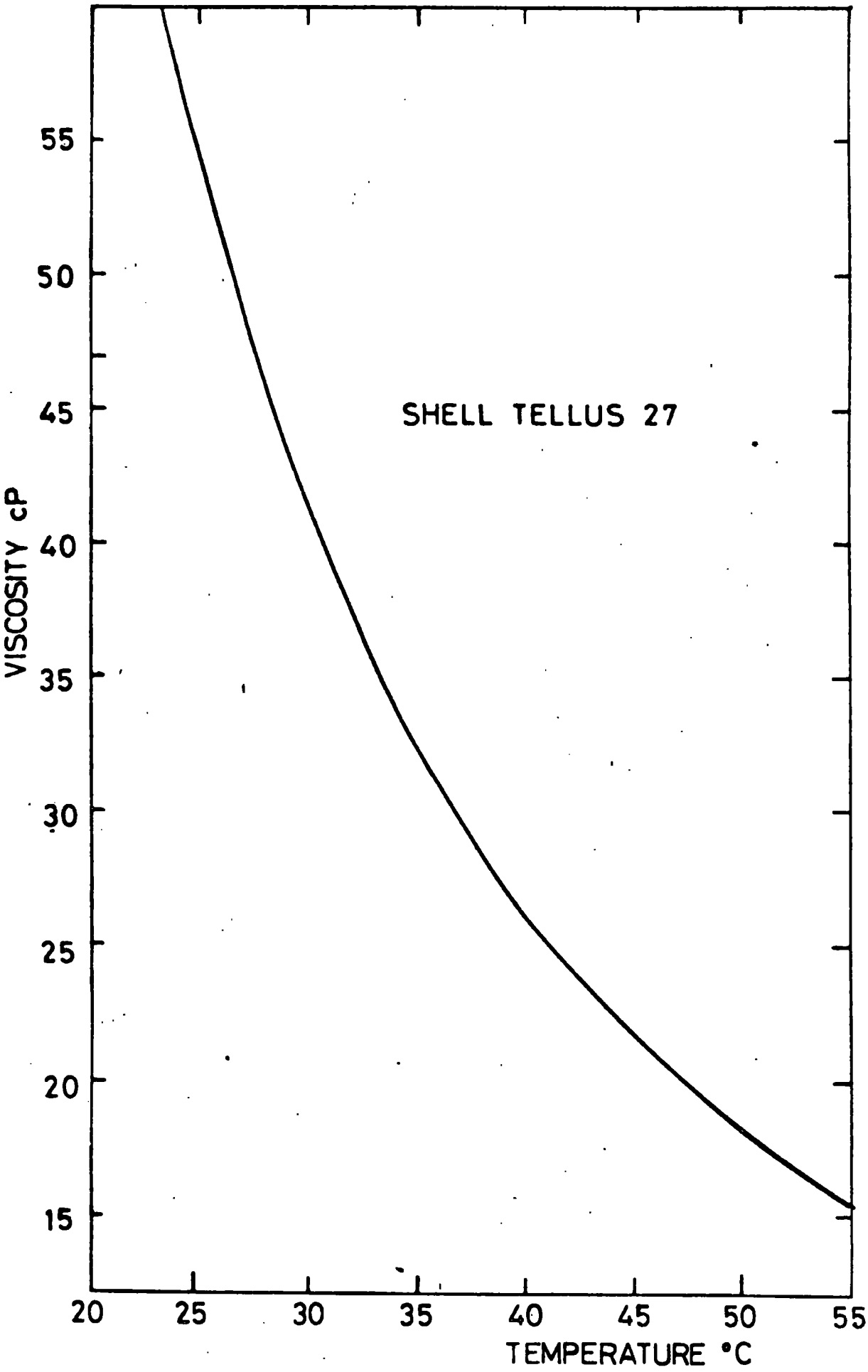

VISCOSITY CALIBRATION

FIG 6·7

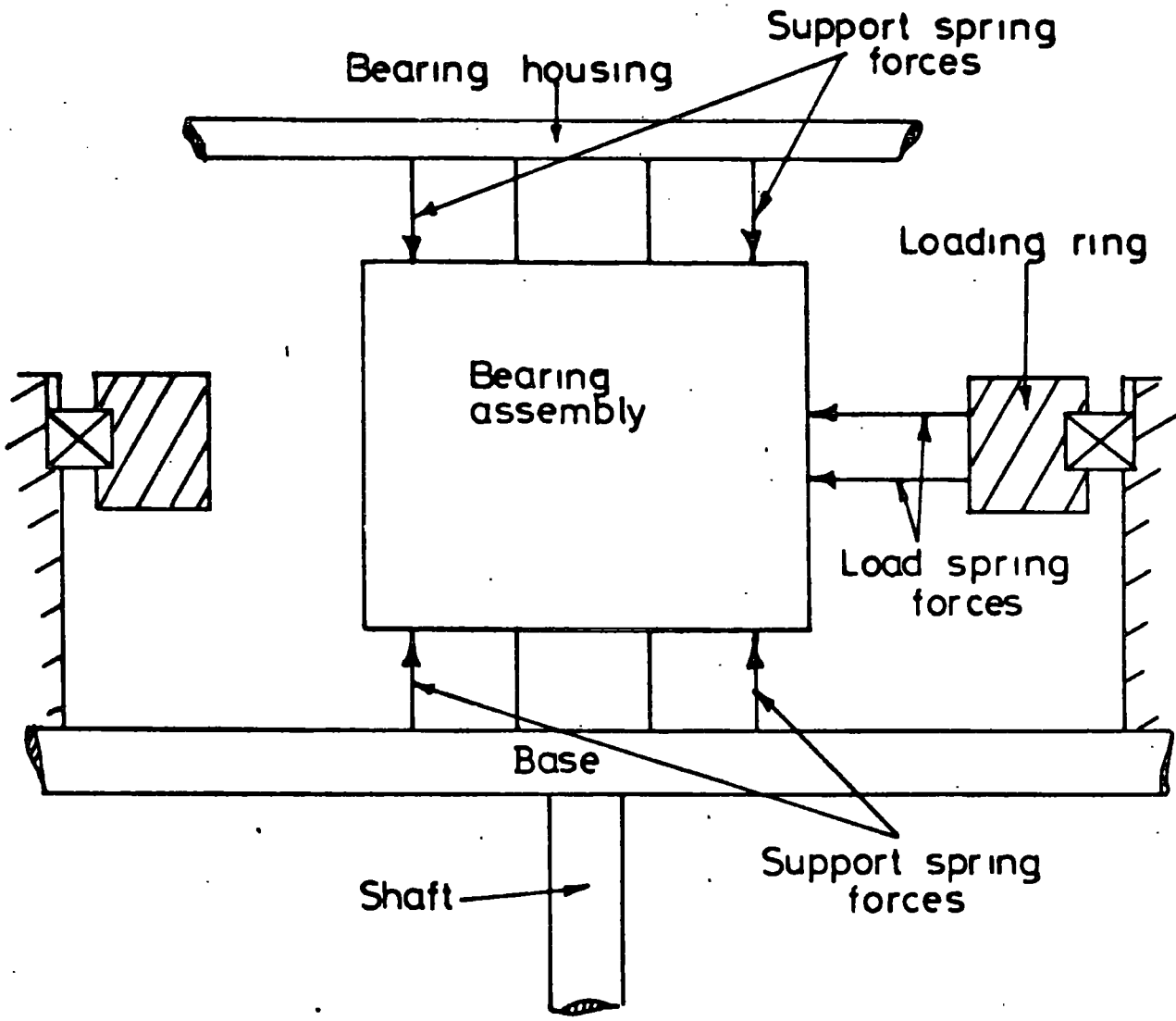

USE OF COMPRESSED SPRINGS AS SUPPORT SYSTEM

FIG 6·8

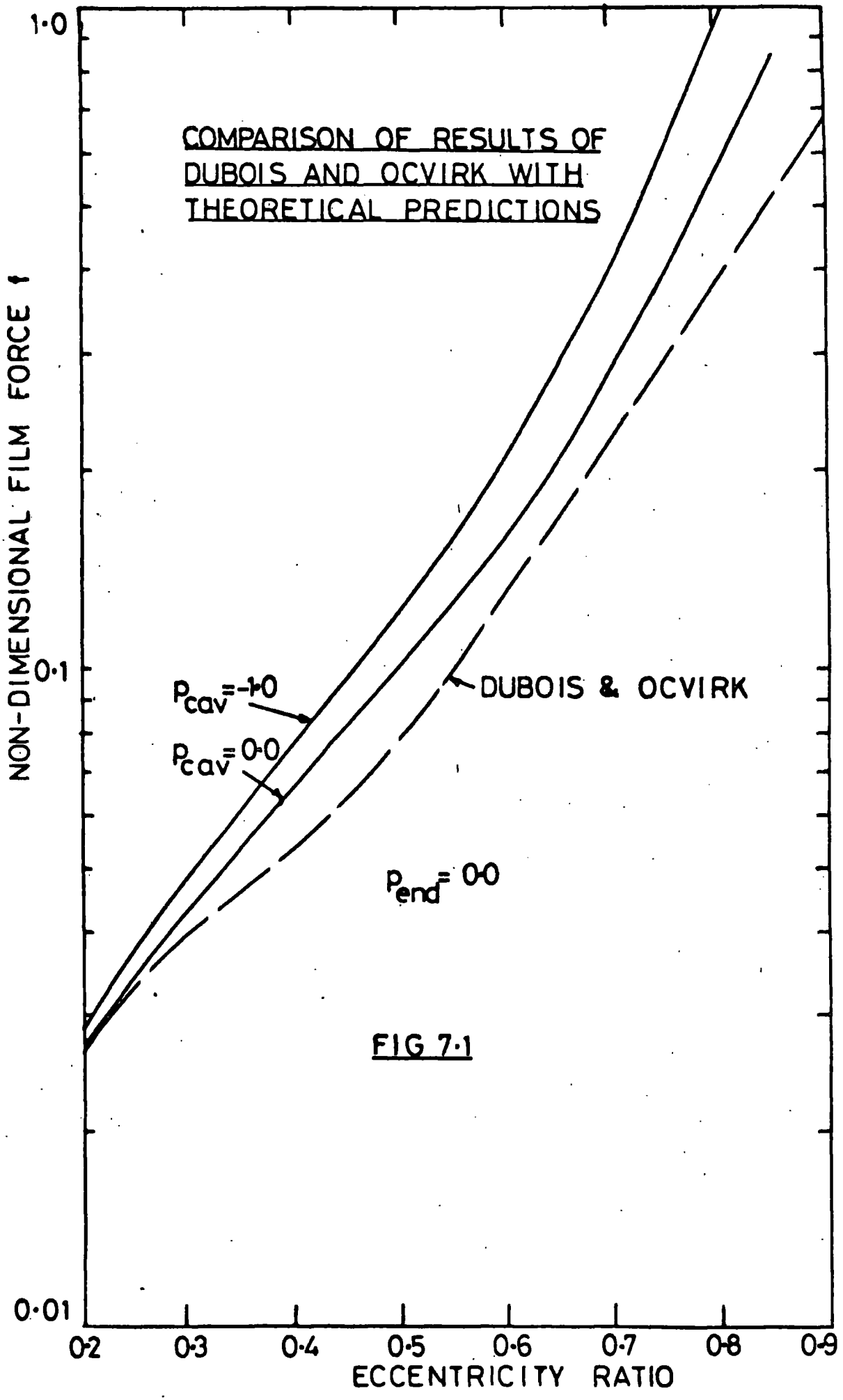
COMPARISON OF RESULTS OF
DUBOIS AND OCVIRK WITH
THEORETICAL PREDICTIONS
NON-DIMENSIONAL FILM FORCE f
1·0
0·1
0·01
P_{cav}=-1·0
P_{cav}=0·0
DUBOIS & OCVIRK
P_{end}= 0·0
0·2
0·3
0·4
0·5
0·6
0·7
0·8
0·9
ECCENTRICITY RATIO

FIG 7·1

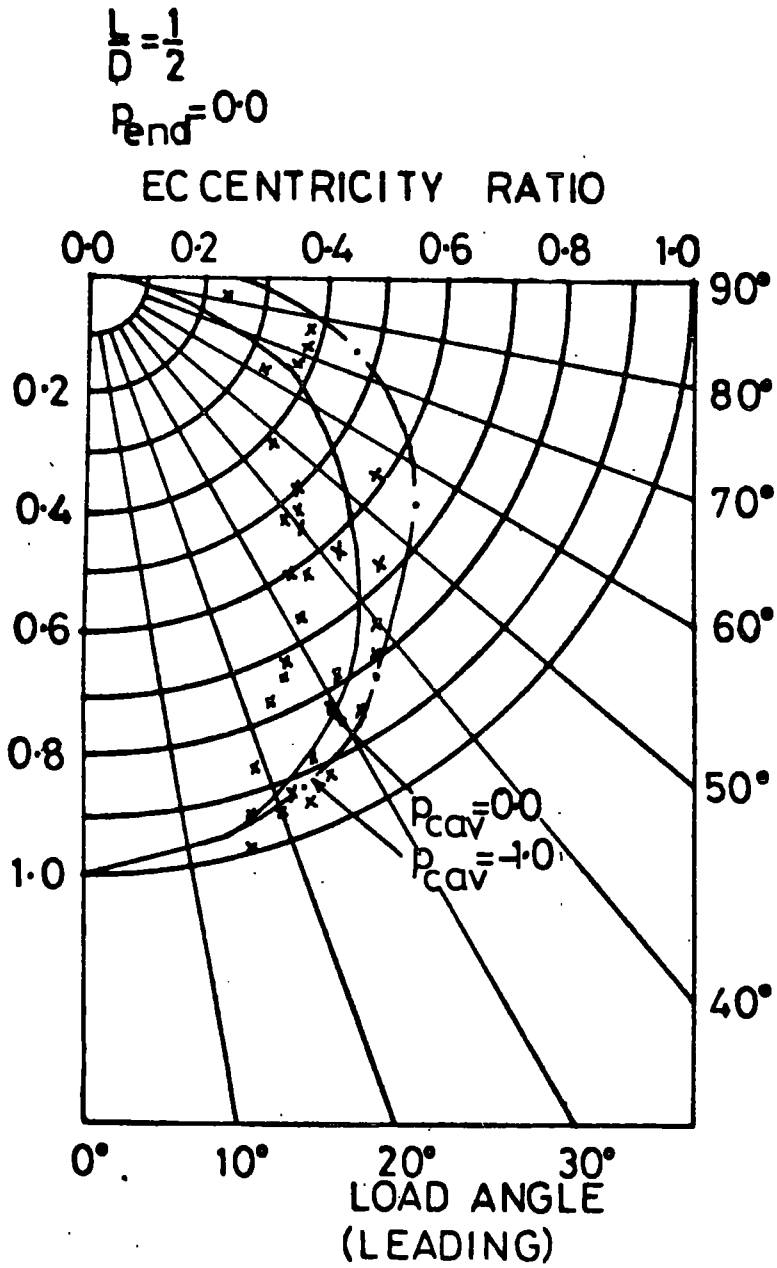

LOAD ANGLE RESULTS FROM DUBOIS AND OCVIRK

FIG 7·2

Experimental Results

Rotating shaft only (steadily loaded bearing)

Symbols	Shaft speed (r.p.m.)
•	300
⊡	400
x	500
v	600
⊗	800

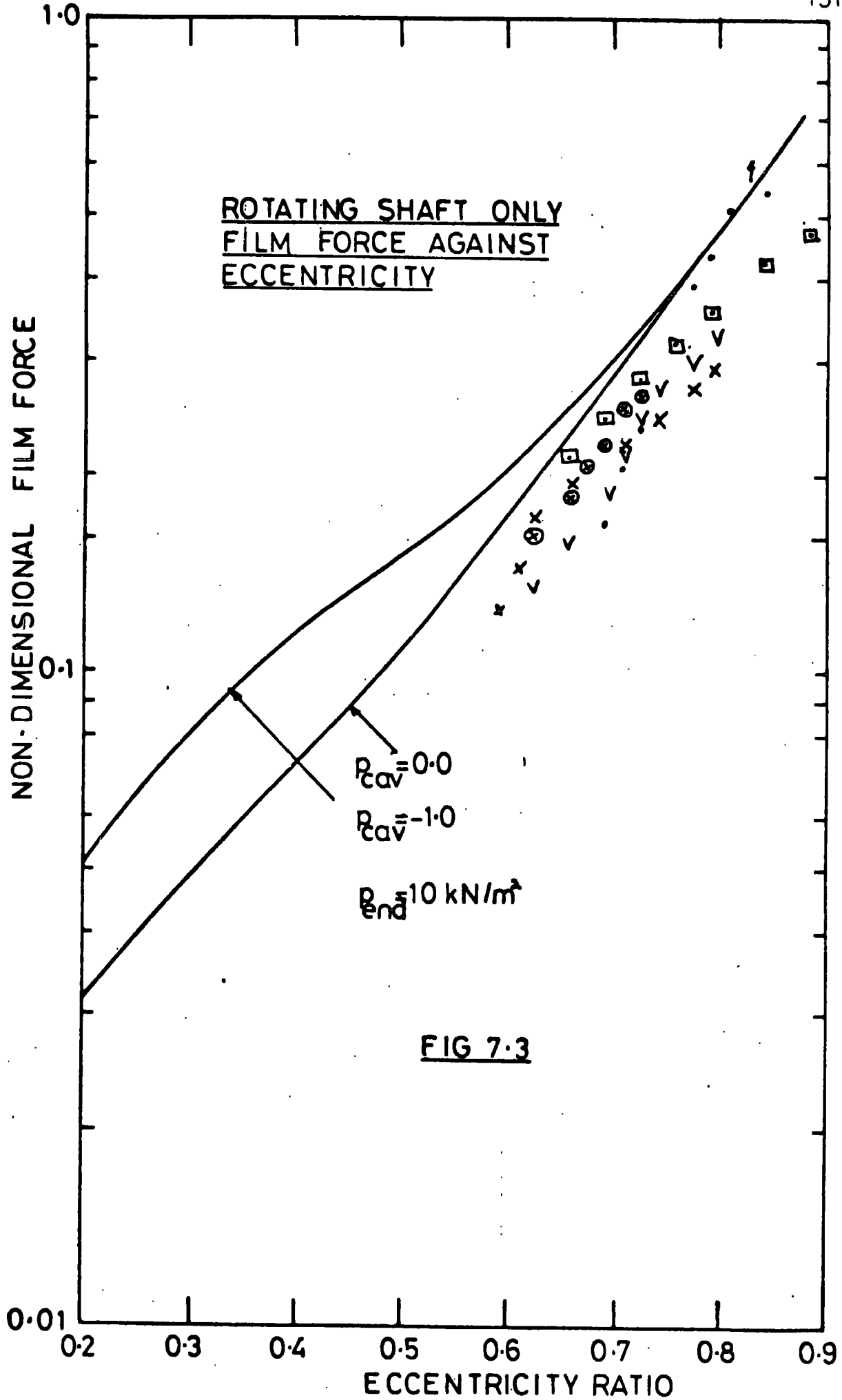
ROTATING SHAFT ONLY
FILM FORCE AGAINST
ECCENTRICITY
NON-DIMENSIONAL FILM FORCE
1·0
0·1
0·01
0·2
0·3
0·4
0·5
0·6
0·7
0·8
0·9
ECCENTRICITY RATIO
P_{cav}=0·0
P_{cav}=-1·0
P_{end}=10 kN/m²

FIG 7·3

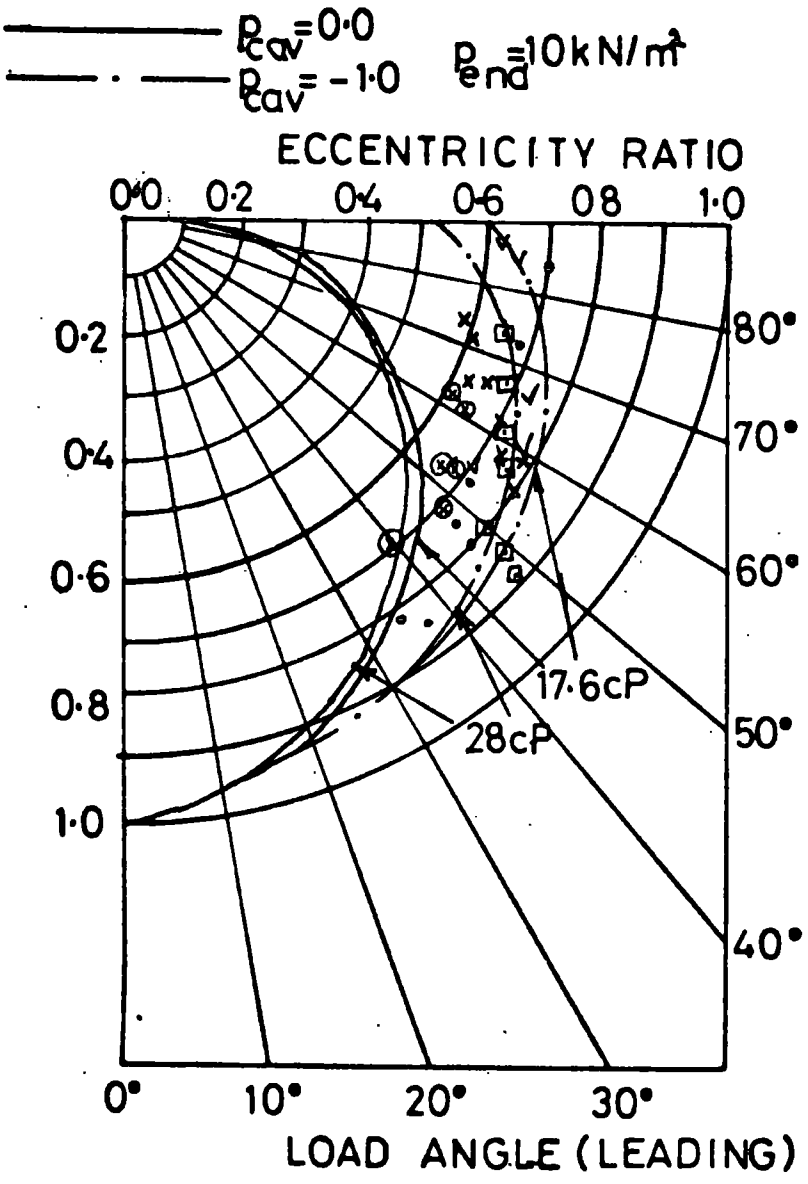

LOAD ANGLE RESULTS FOR ROTATING SHAFT ONLY

FIG 7·4

Experimental Results

Rotating load only, rotating shaft with rotating load

Symbols		Individual bearing load, W (N).
⊹		344
↑		288
◇		228
+		168
⅄	Figs 6.8, 6.16 and 6.24 only	317
⌀		257
△		198
o		154

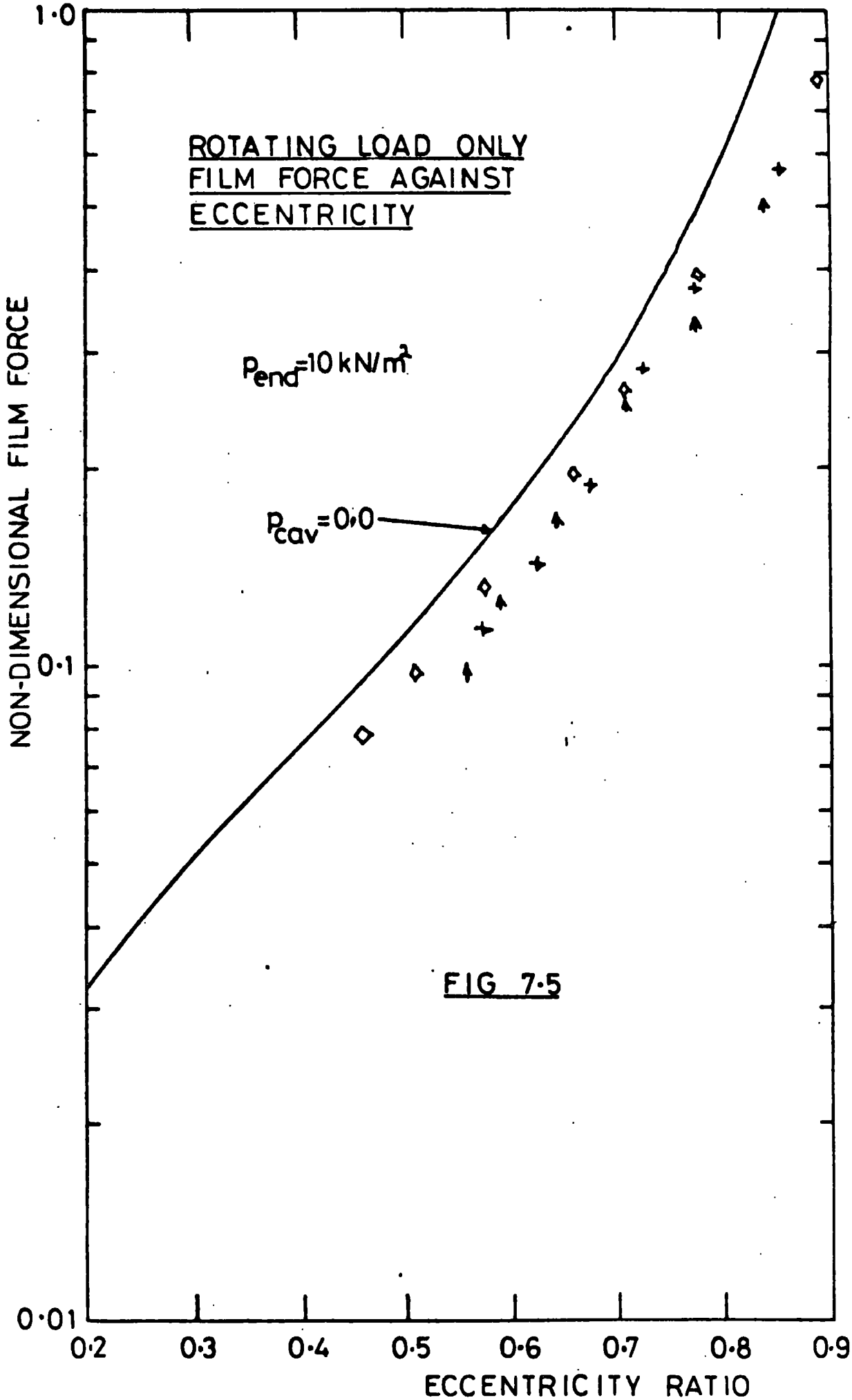
ROTATING LOAD ONLY
FILM FORCE AGAINST
ECCENTRICITY
P_{end}=10 kN/m²
P_{cav}=0·0
NON-DIMENSIONAL FILM FORCE
1·0
0·1
0·01
0·2
0·3
0·4
0·5
0·6
0·7
0·8
0·9
ECCENTRICITY RATIO

FIG 7·5

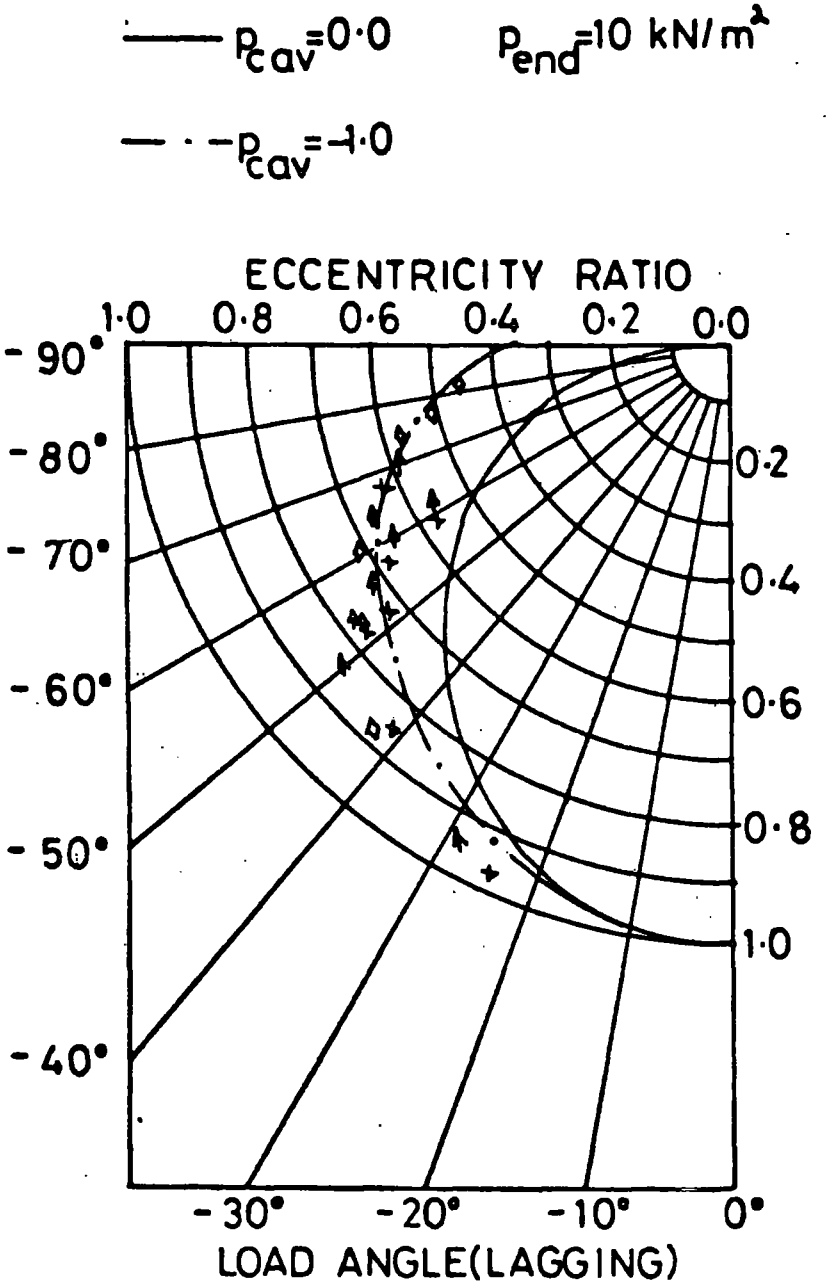

LOAD ANGLE RESULTS FOR ROTATING LOAD ONLY

FIG 7·6

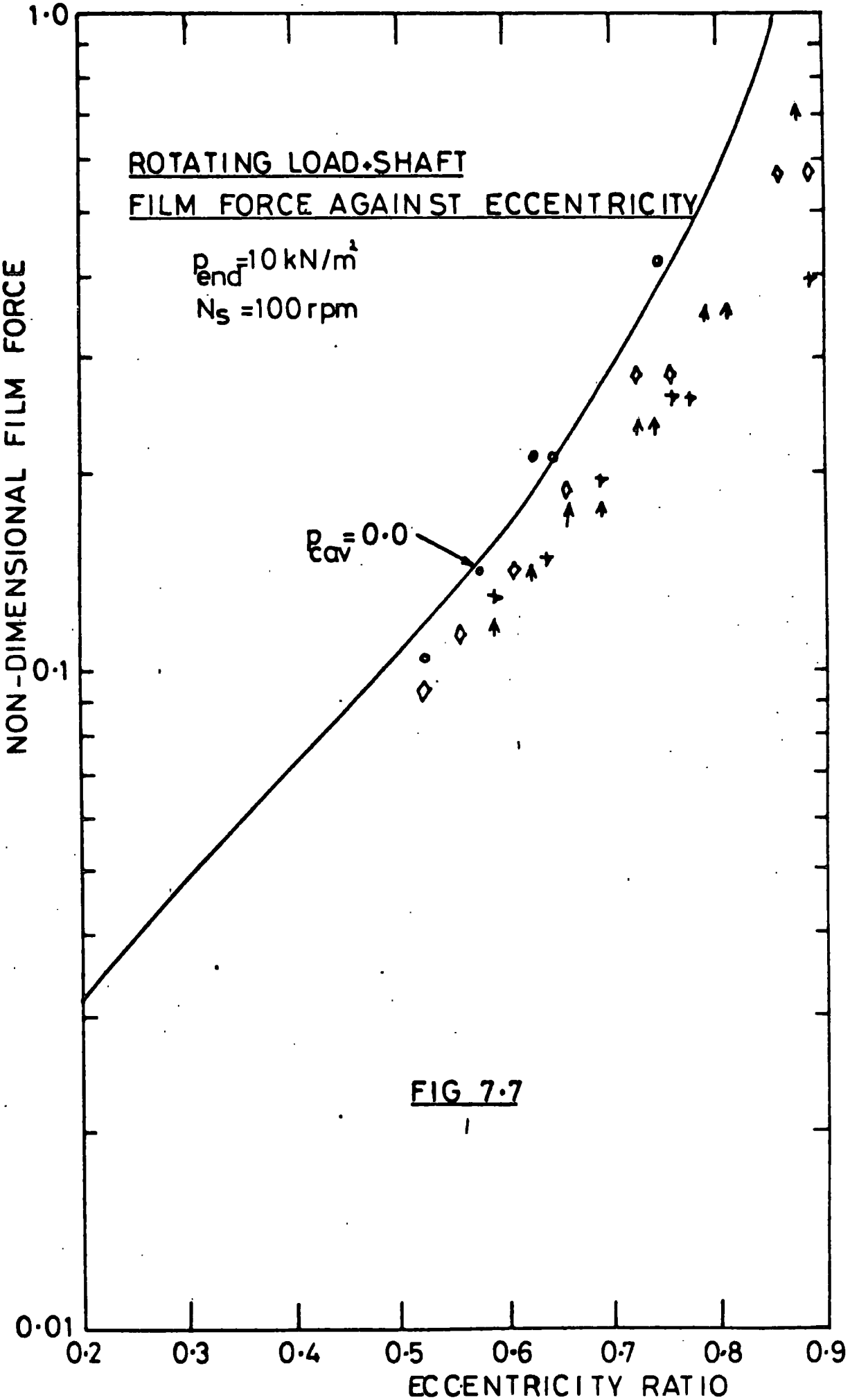
ROTATING LOAD-SHAFT
FILM FORCE AGAINST ECCENTRICITY
p_{end}=10 kN/m²
N_S =100 rpm
p_{cav}=0·0
NON-DIMENSIONAL FILM FORCE
1·0
0·1
0·01
0·2
0·3
0·4
0·5
0·6
0·7
0·8
0·9
ECCENTRICITY RATIO

FIG 7·7

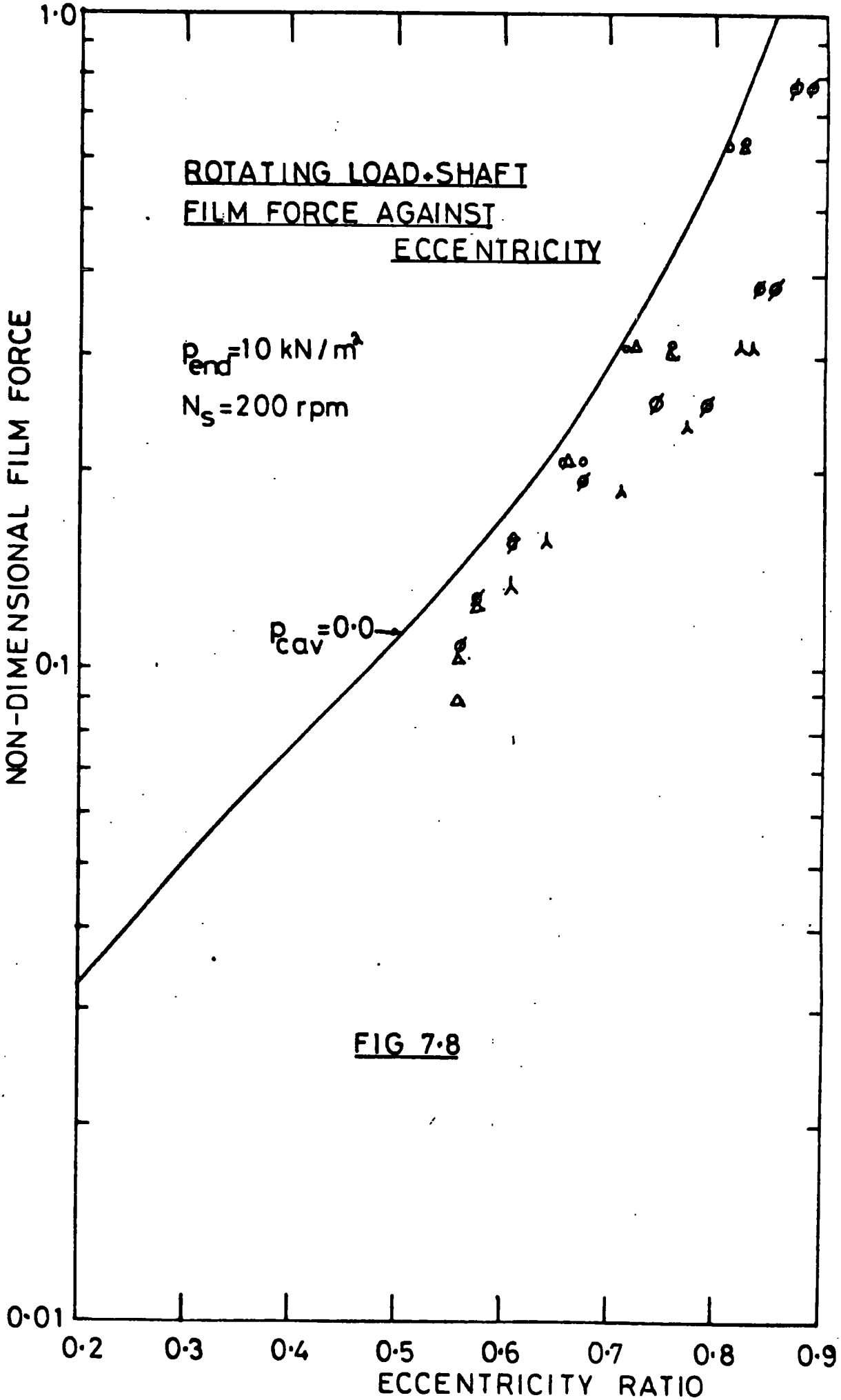
ROTATING LOAD+SHAFT
FILM FORCE AGAINST
ECCENTRICITY
P_{end}=10 kN/m²
N_s=200 rpm
P_{cav}=0·0
NON-DIMENSIONAL FILM FORCE
1·0
0·1
0·01
0·2
0·3
0·4
0·5
0·6
0·7
0·8
0·9
ECCENTRICITY RATIO

FIG 7·8

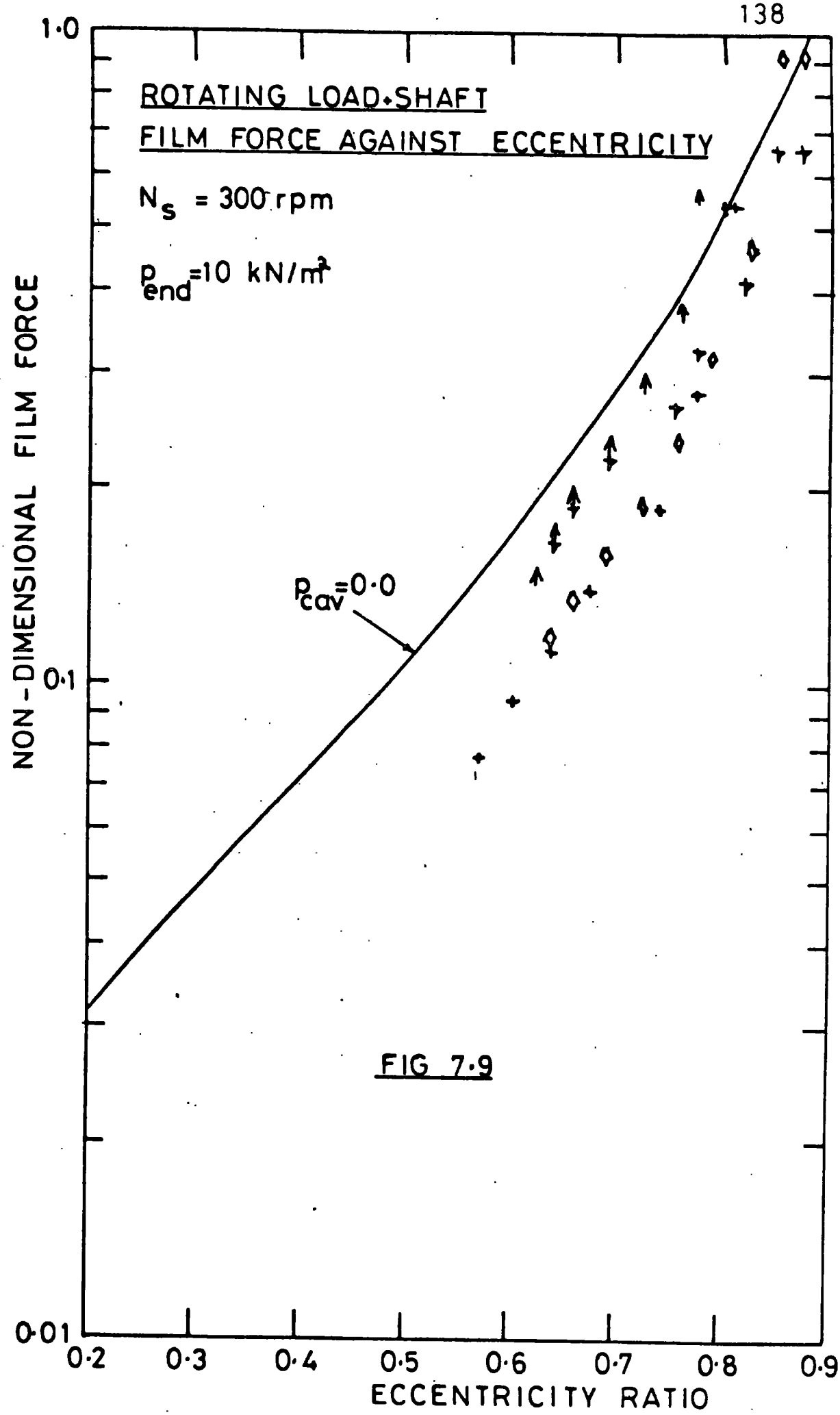
ROTATING LOAD+SHAFT
FILM FORCE AGAINST ECCENTRICITY
N_s = 300 rpm
p_{end}=10 kN/m²
P_{cav}=0·0
NON-DIMENSIONAL FILM FORCE
1·0
0·1
0·01
0·2
0·3
0·4
0·5
0·6
0·7
0·8
0·9
ECCENTRICITY RATIO

FIG 7·9

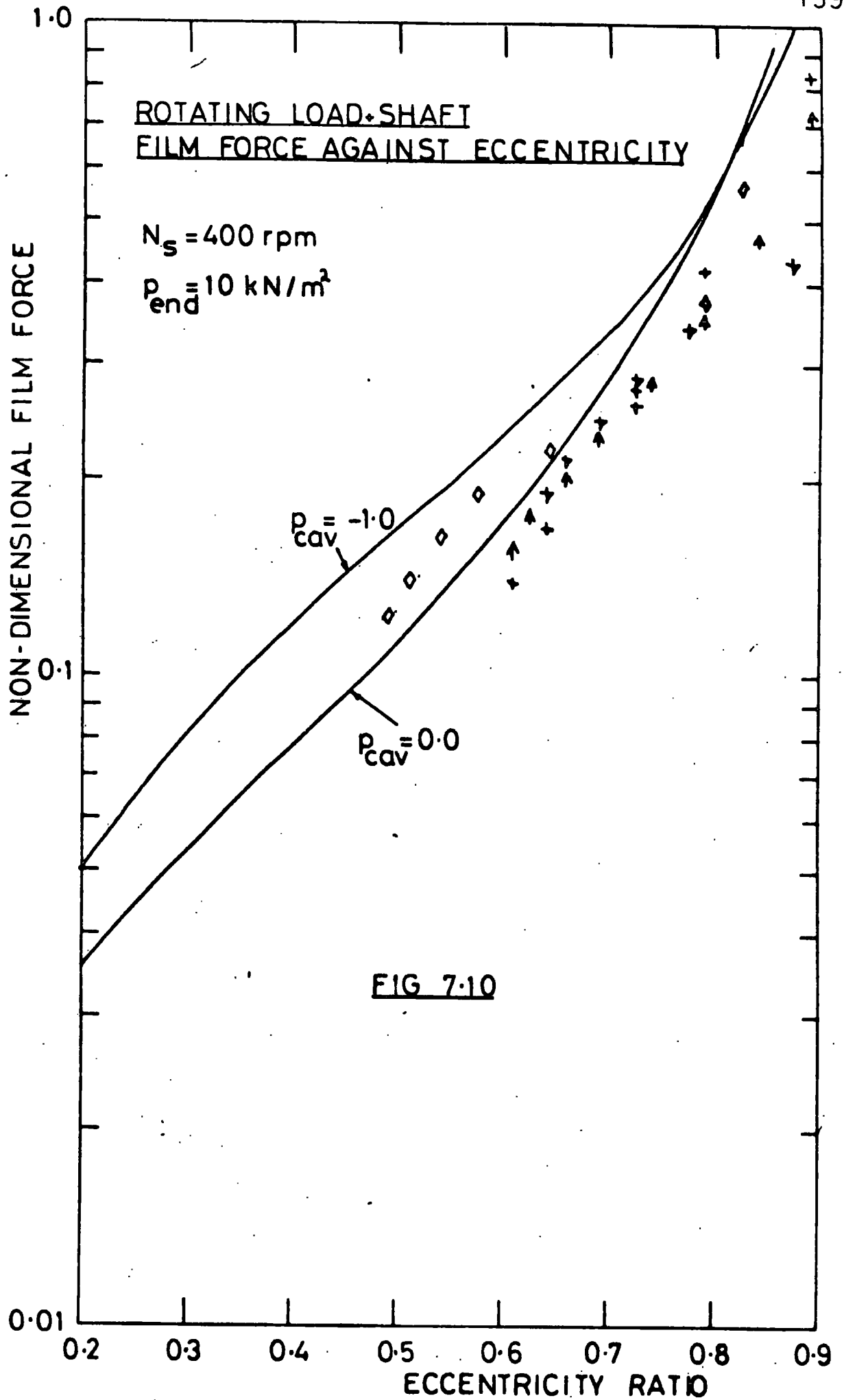
ROTATING LOAD+SHAFT
FILM FORCE AGAINST ECCENTRICITY
N_s = 400 rpm
p_{end} = 10 kN/m²
p_{cav} = -1·0
p_{cav} = 0·0
NON-DIMENSIONAL FILM FORCE
1·0
0·1
0·01
0·2
0·3
0·4
0·5
0·6
0·7
0·8
0·9
ECCENTRICITY RATIO

FIG 7·10

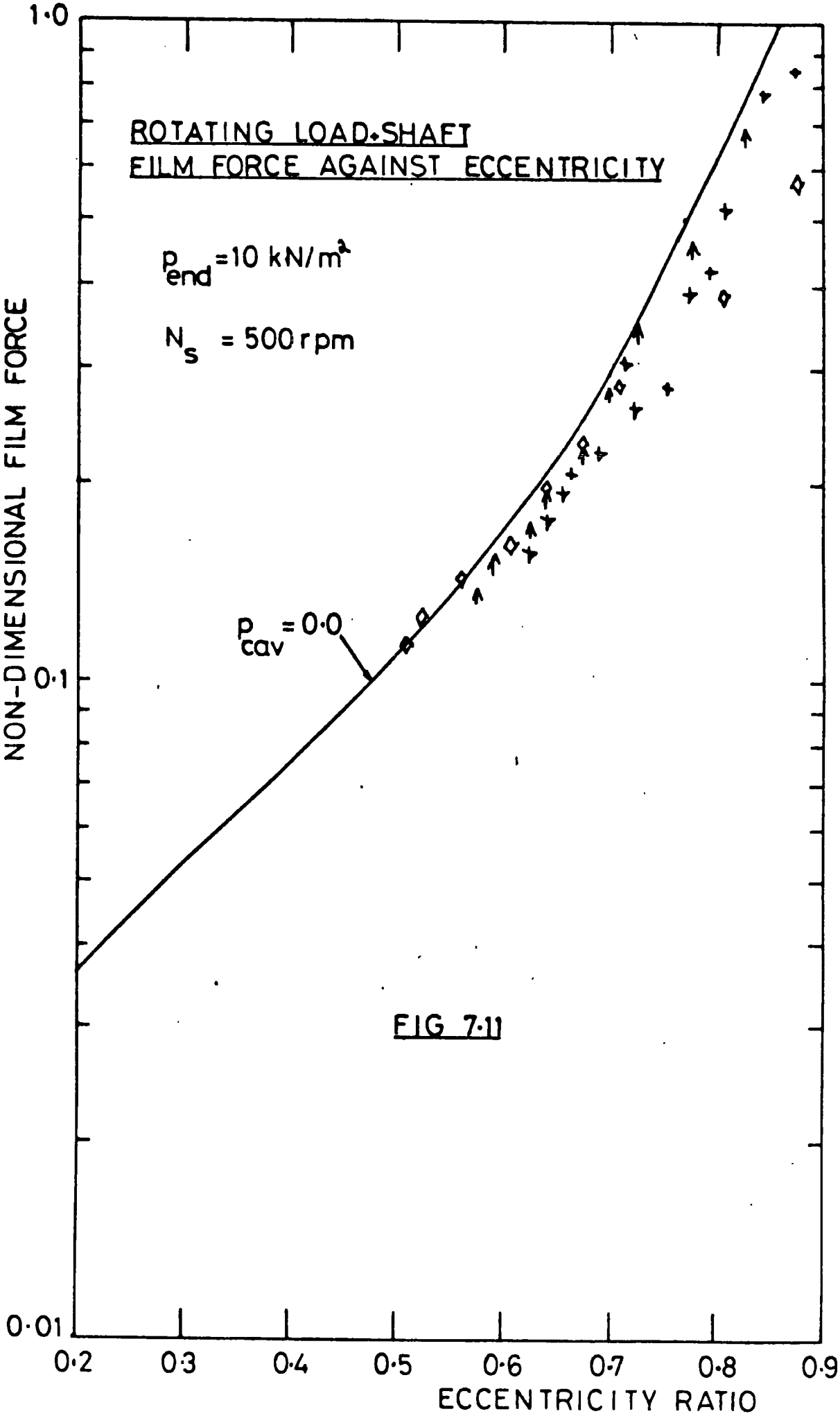
ROTATING LOAD-SHAFT
FILM FORCE AGAINST ECCENTRICITY
p_{end}=10 kN/m²
N_s = 500 rpm
p_{cav} = 0·0
NON-DIMENSIONAL FILM FORCE
1·0
0·1
0·01
0·2
0·3
0·4
0·5
0·6
0·7
0·8
0·9
ECCENTRICITY RATIO

FIG 7·11

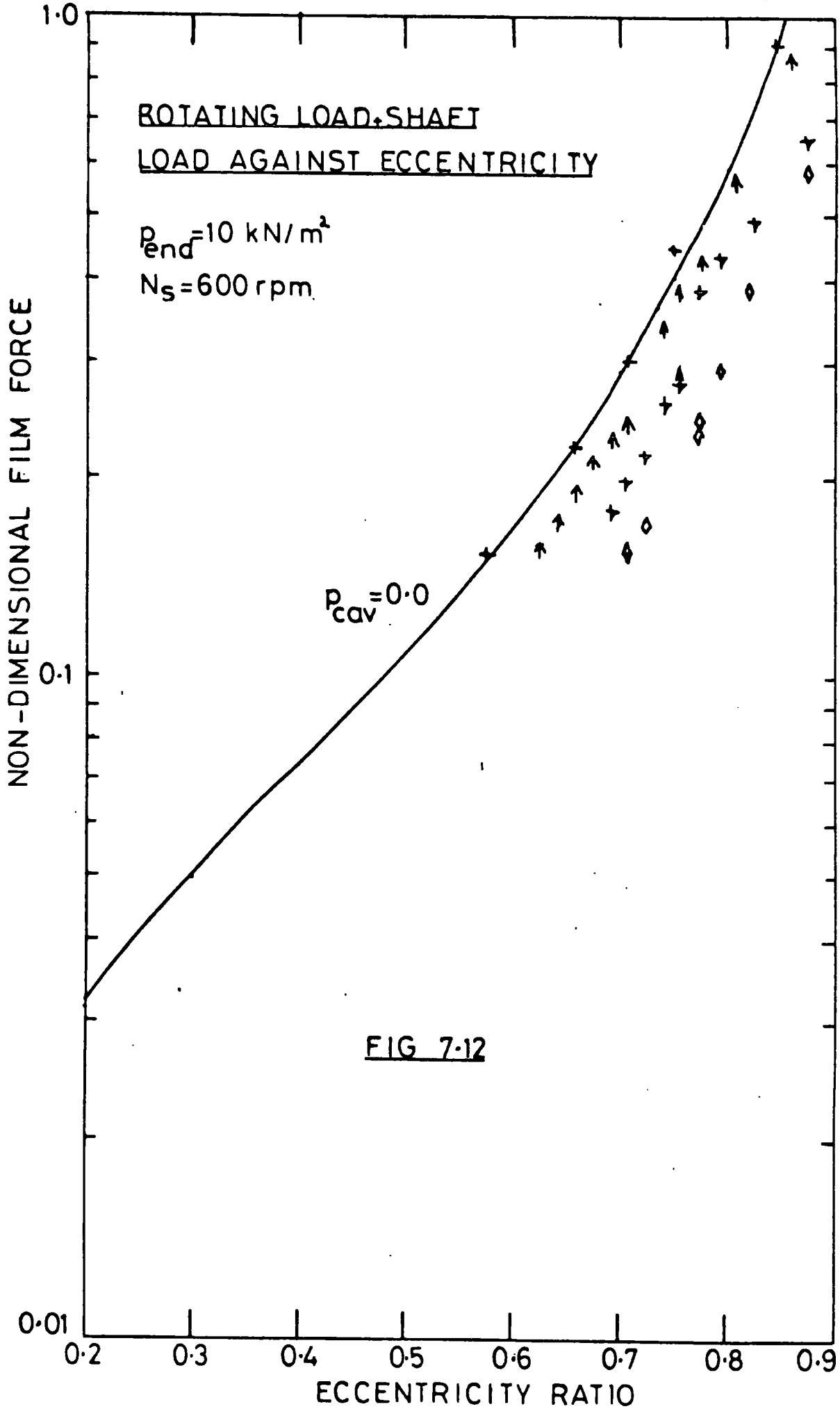
ROTATING LOAD+SHAFT
LOAD AGAINST ECCENTRICITY
p_{end}=10 kN/m²
N_S=600 rpm
p_{cav}=0·0
NON-DIMENSIONAL FILM FORCE
1·0
0·1
0·01
0·2
0·3
0·4
0·5
0·6
0·7
0·8
0·9
ECCENTRICITY RATIO

FIG 7·12

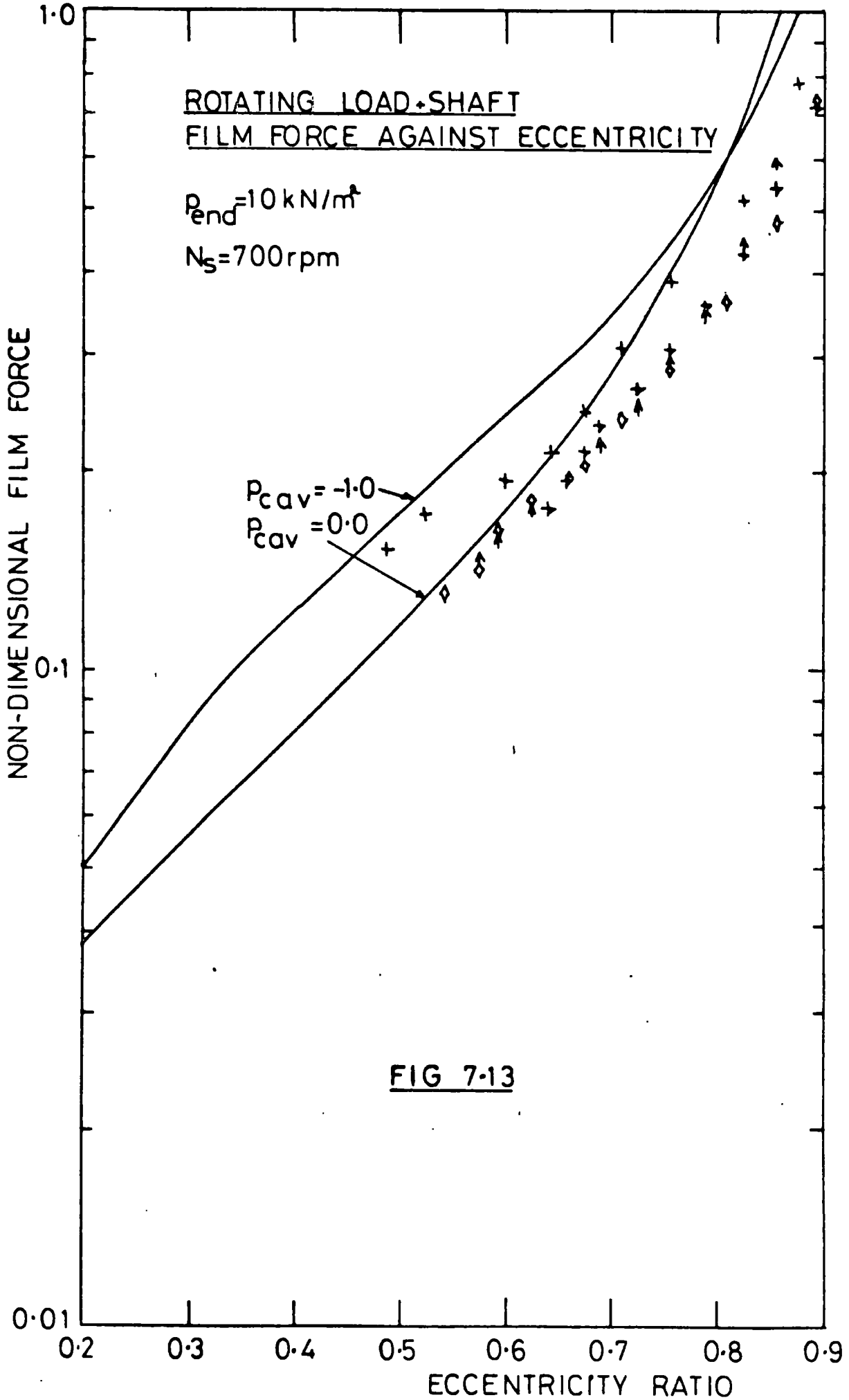
ROTATING LOAD+SHAFT
FILM FORCE AGAINST ECCENTRICITY
P_{end}=10 kN/m²
N_S=700 rpm
P_{cav}= -1·0
P_{cav} =0·0
NON-DIMENSIONAL FILM FORCE
1·0
0·1
0·01
0·2
0·3
0·4
0·5
0·6
0·7
0·8
0·9
ECCENTRICITY RATIO

FIG 7·13

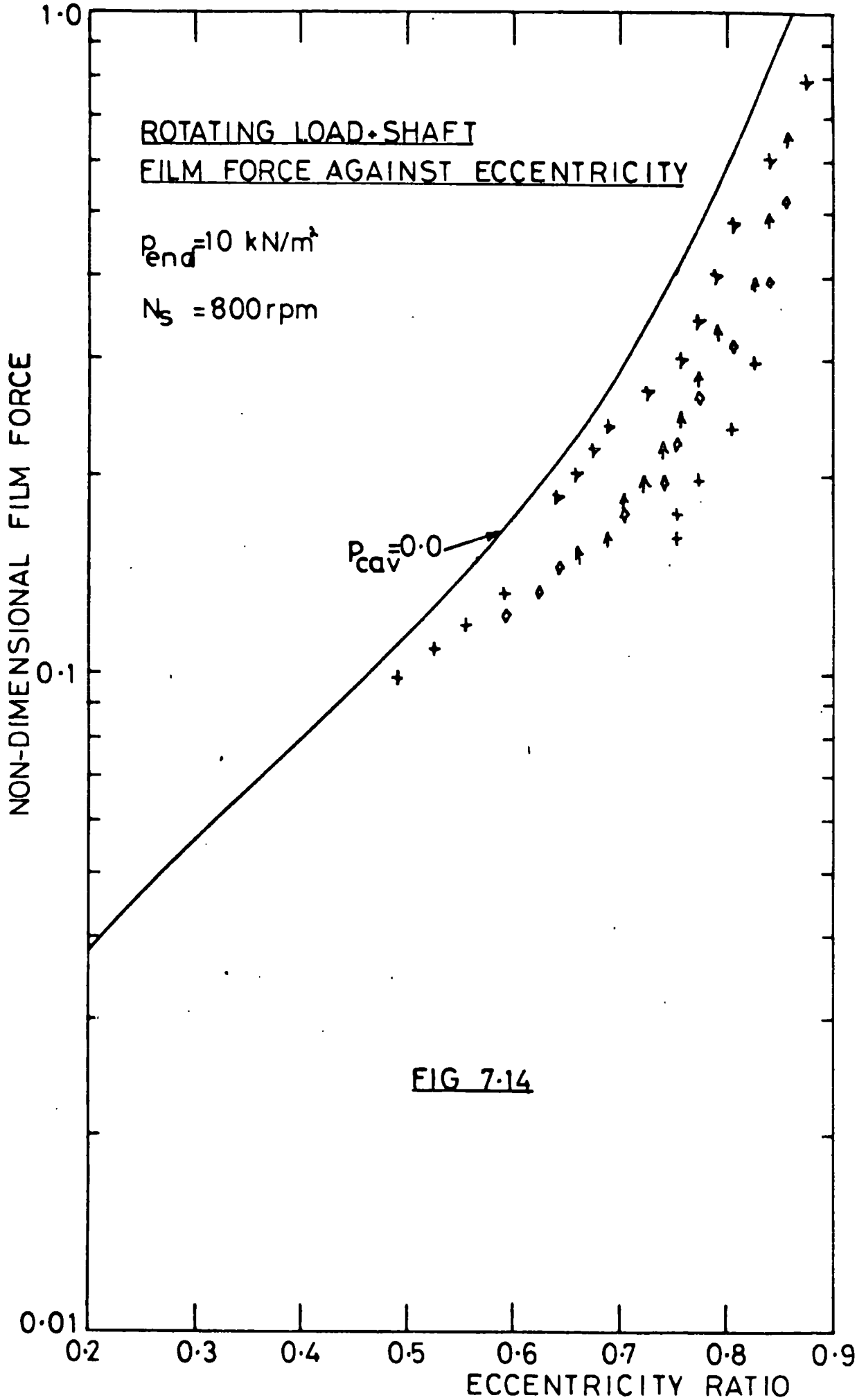
ROTATING LOAD+SHAFT
FILM FORCE AGAINST ECCENTRICITY
P_{end}=10 kN/m²
N_S =800rpm
P_{cav}=0·0
NON-DIMENSIONAL FILM FORCE
1·0
0·1
0·01
0·2
0·3
0·4
0·5
0·6
0·7
0·8
0·9
ECCENTRICITY RATIO

FIG 7·14

—— p_{cav}=0·0 p_{end}=10 kN/m²

N_s=100 rpm

—·— p_{cav}=-1·0

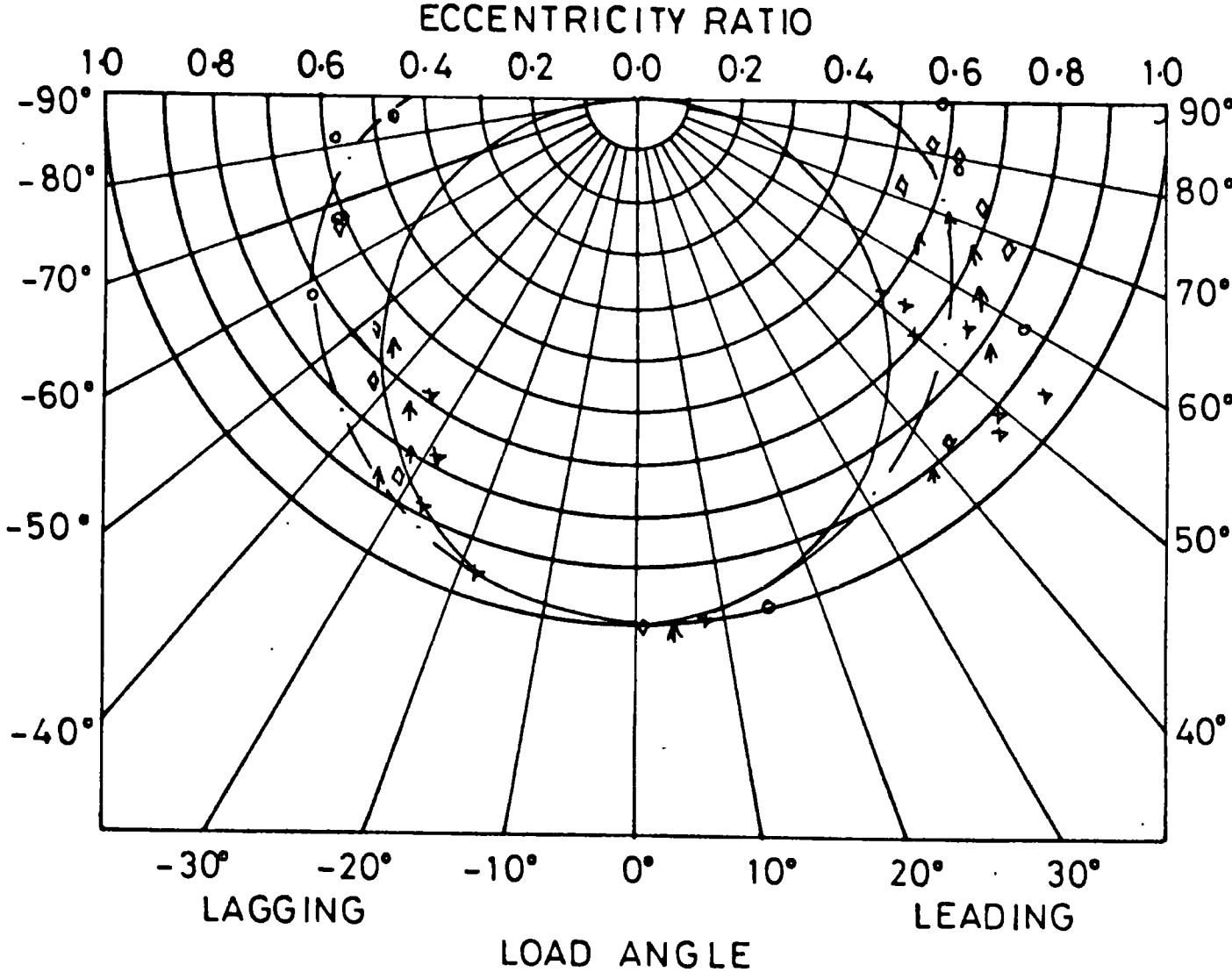

ROTATING LOAD + SHAFT
LOAD ANGLE RESULTS

FIG 7·15

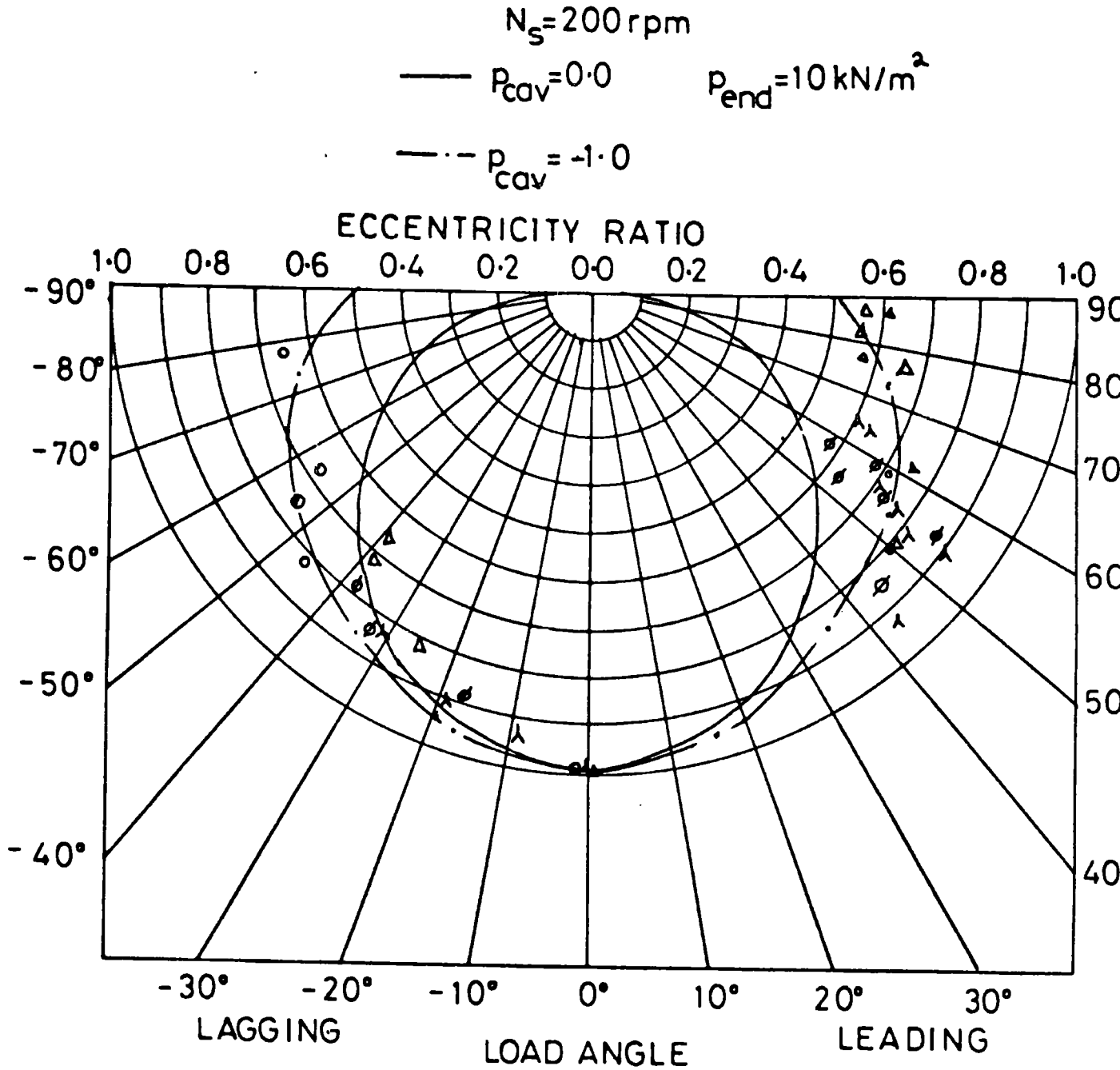

ROTATING LOAD + SHAFT
LOAD ANGLE RESULTS

FIG 7·16

N_s = 300 rpm

——— p_{cav} = 0·0 p_{end} = 10 k N/ m

—·— p_{cav} = -1·0

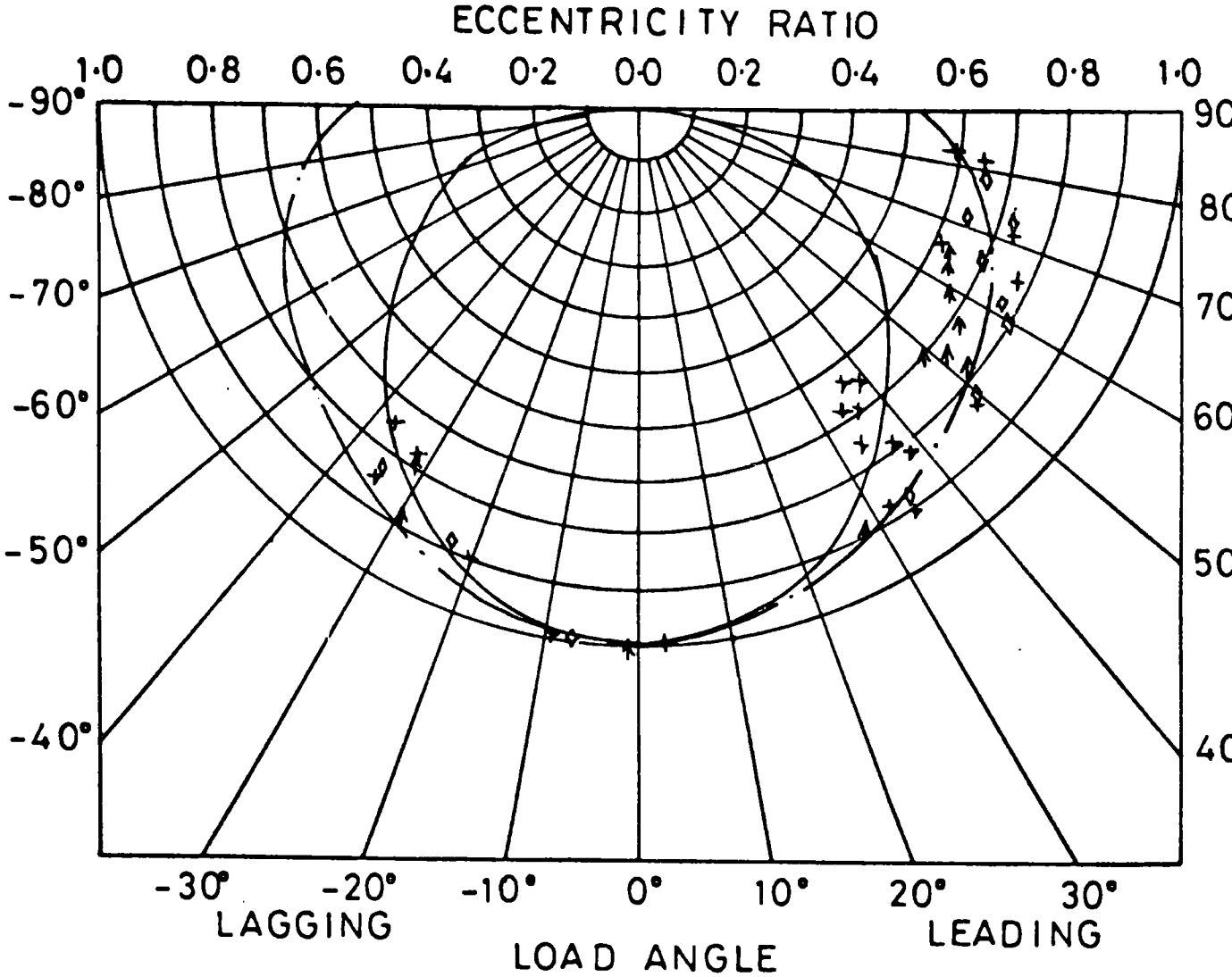

ROTATING LOAD-SHAFT
LOAD ANGLE RESULTS

FIG 7·17

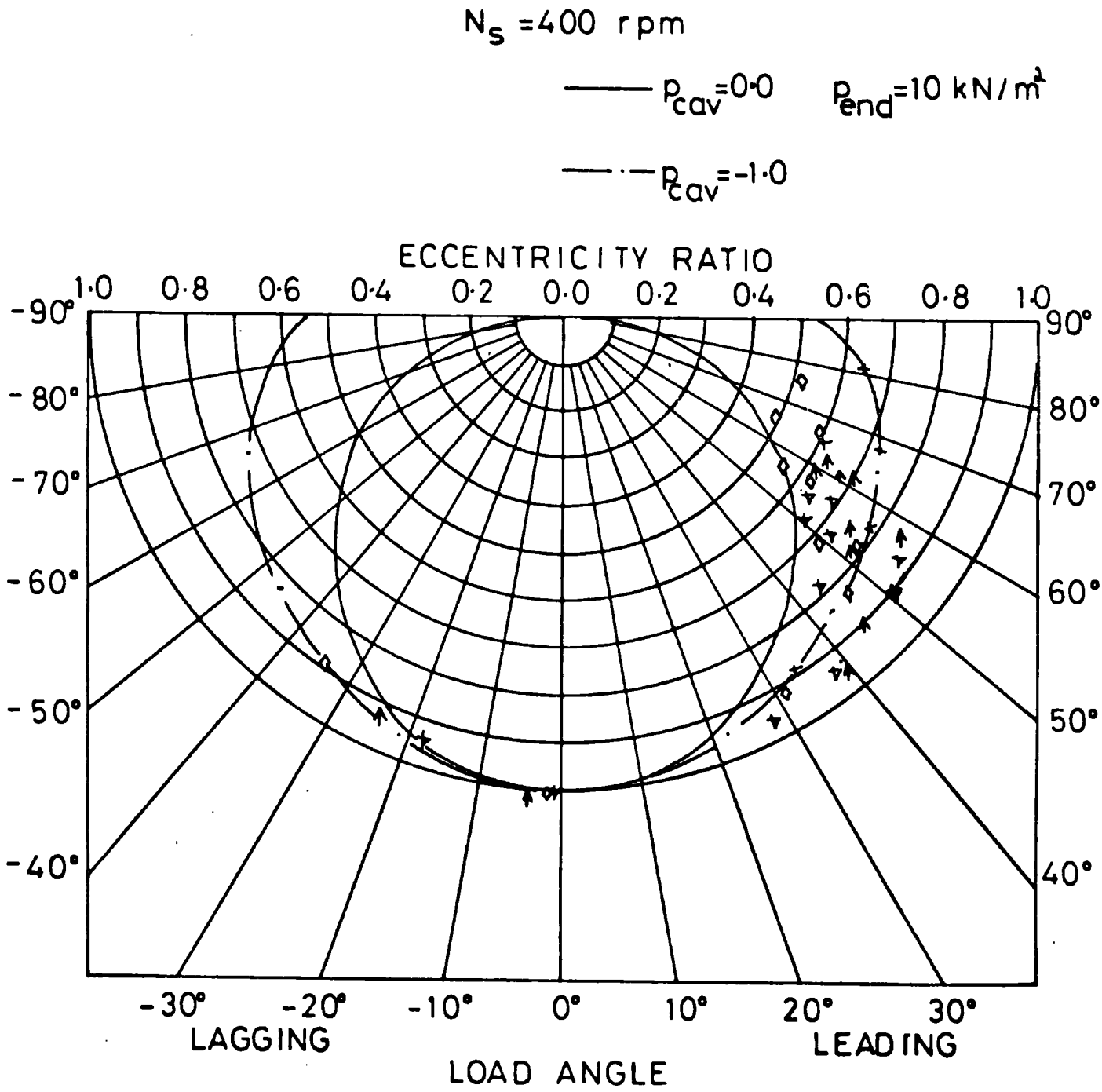

ROTATING LOAD+SHAFT
LOAD ANGLE RESULTS

FIG 7·18

N_s = 500 rpm

—— p_{cav}=0·0 p_{end}=10 kN/m²

—·— p_{cav}=-1·0

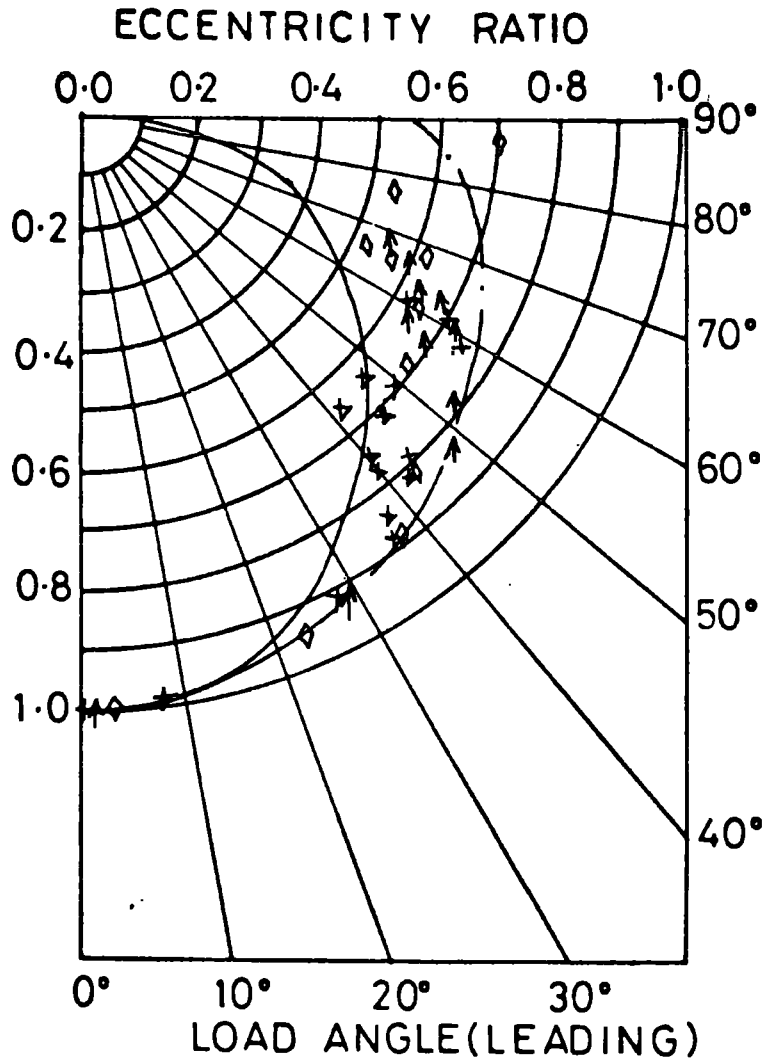

ROTATING LOAD+SHAFT
LOAD ANGLE RESULTS

FIG 7·19

$N_s = 600$ rpm

——— $p_{cav} = 0{\cdot}0$ $p_{end} = 10\ kN/m^2$

—·— $p_{cav} = -1{\cdot}0$

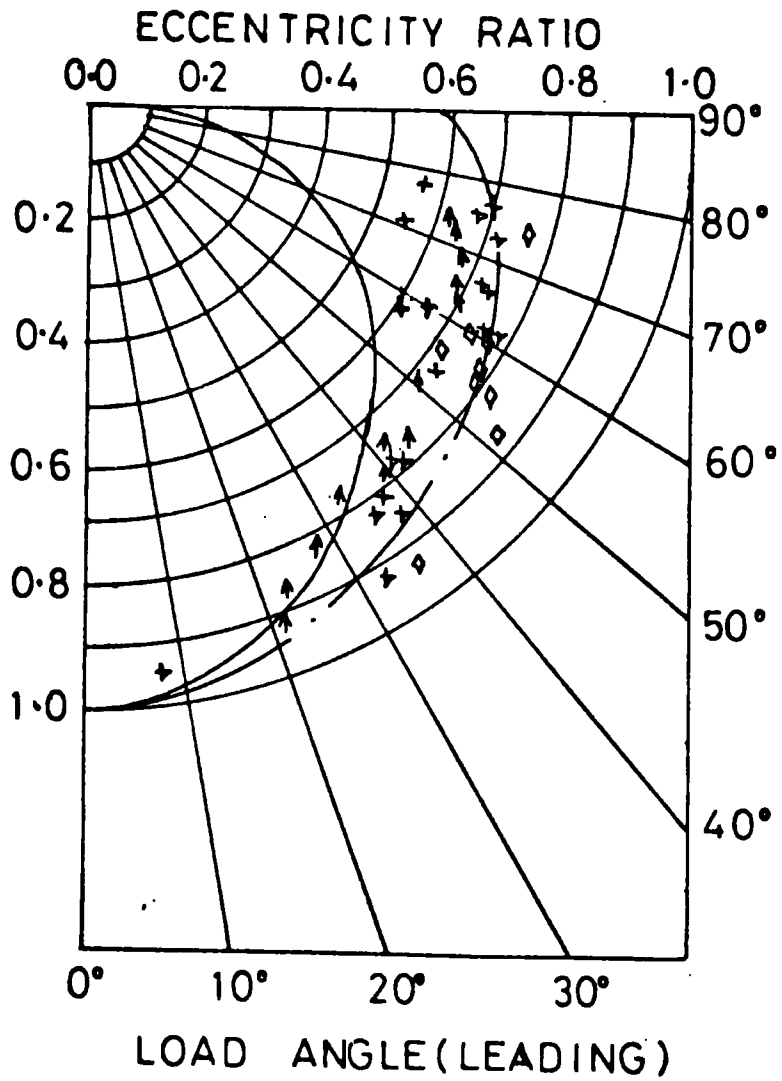

ROTATING LOAD + SHAFT
LOAD ANGLE RESULTS

FIG 7·20

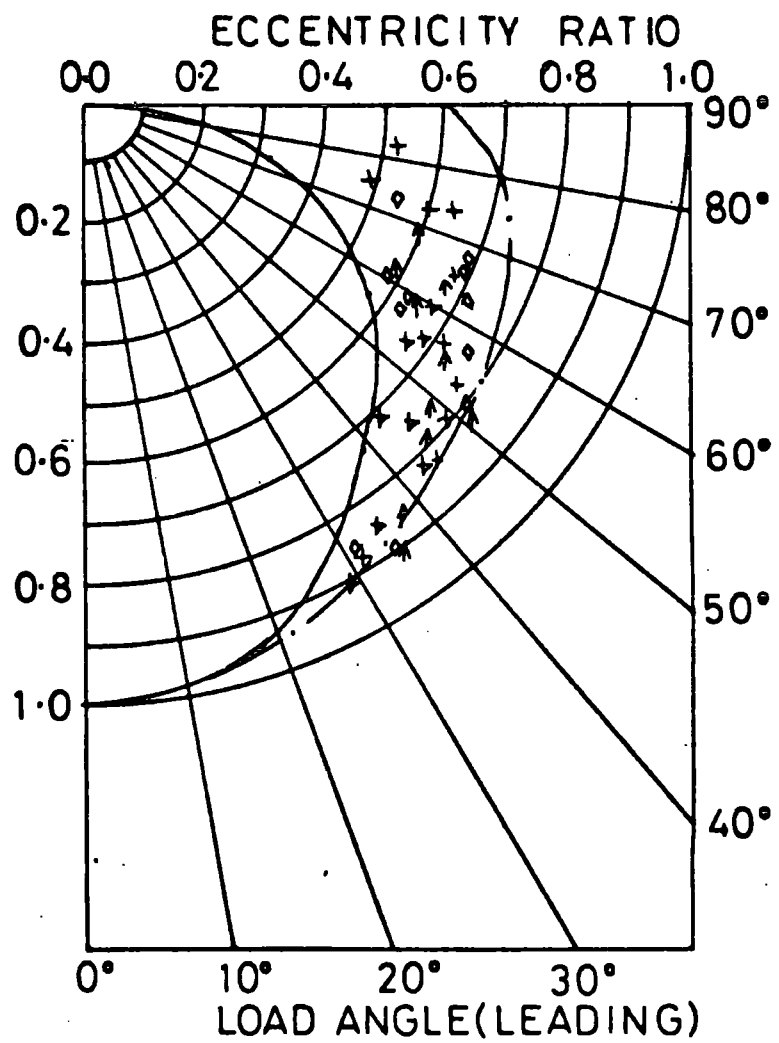

ROTATING LOAD+SHAFT
LOAD ANGLE RESULTS

FIG 7·21

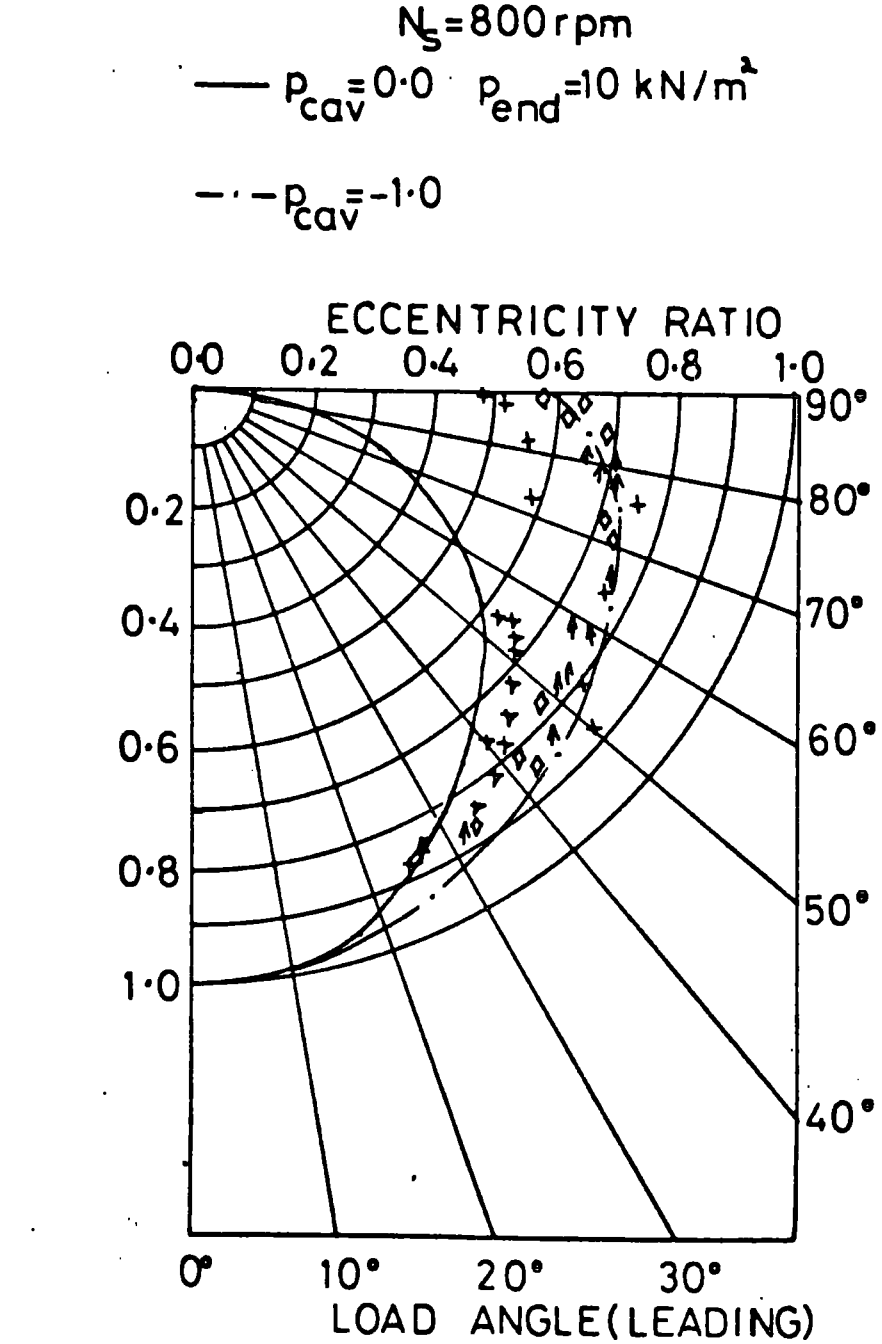

ROTATING LOAD-SHAFT
LOAD ANGLE RESULTS

FIG 7·22

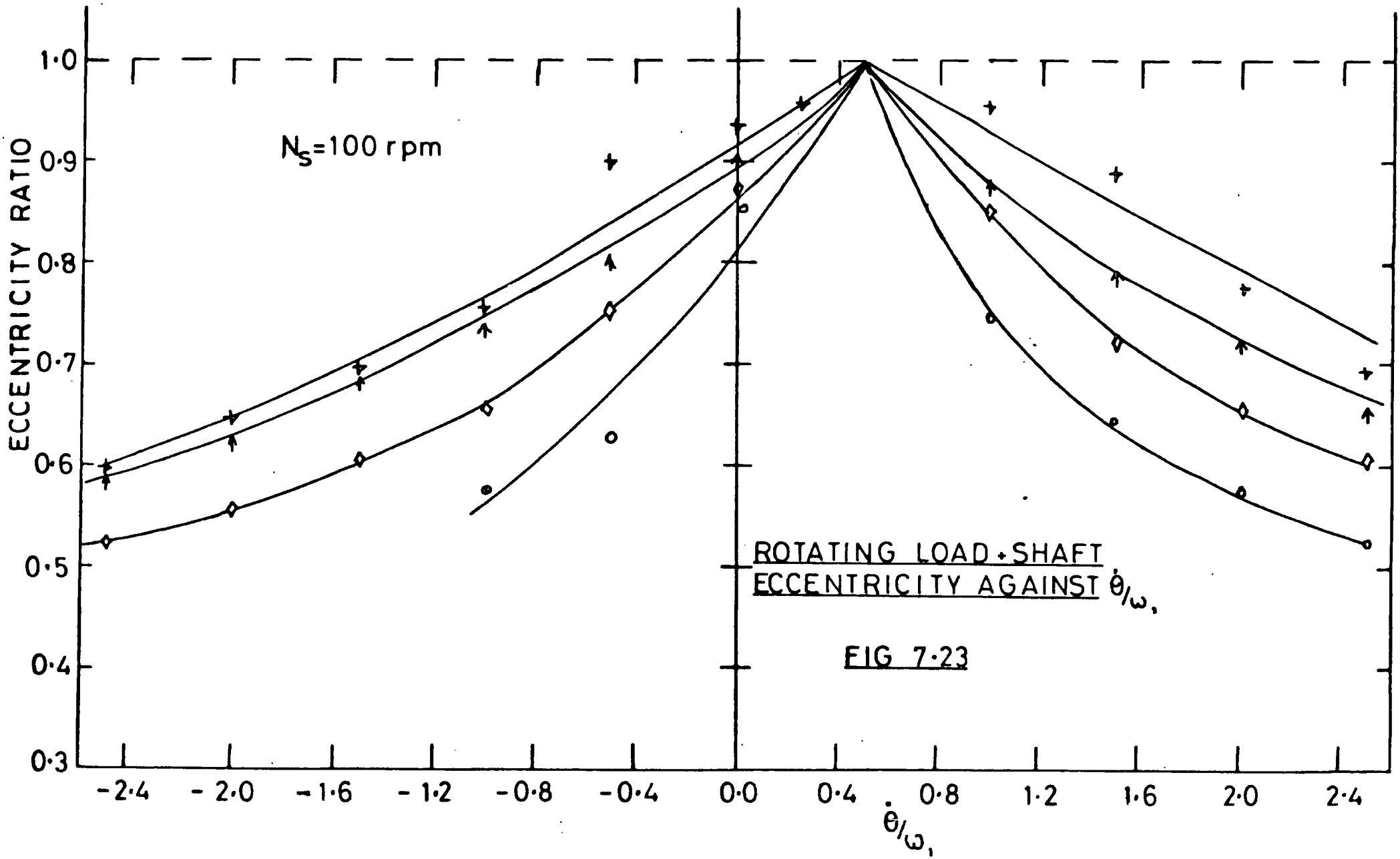

ROTATING LOAD + SHAFT ECCENTRICITY AGAINST $\dot{\theta}/\omega_1$

FIG 7·23

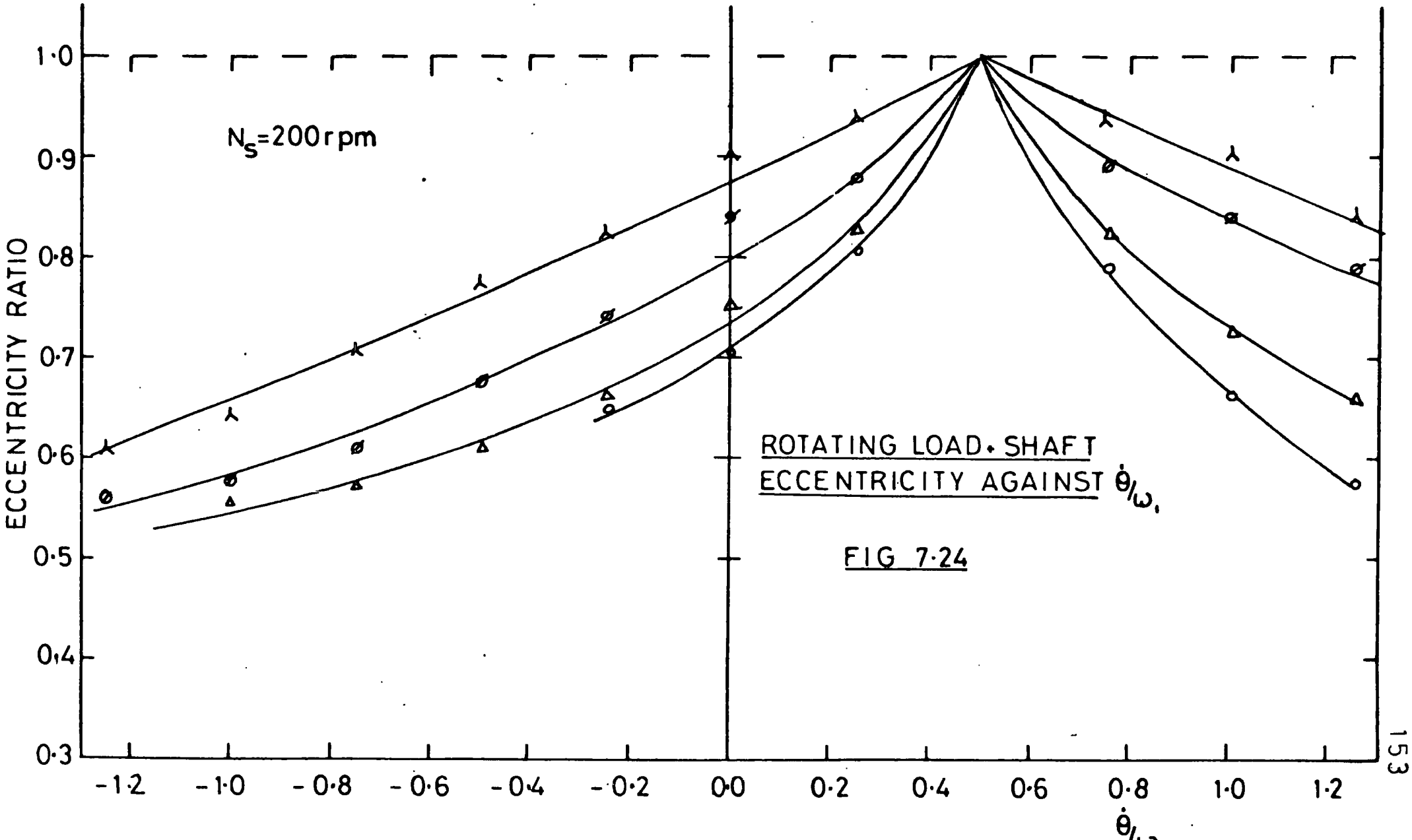

ROTATING LOAD + SHAFT
ECCENTRICITY AGAINST $\dot{\theta}/\omega_s$

FIG 7·24

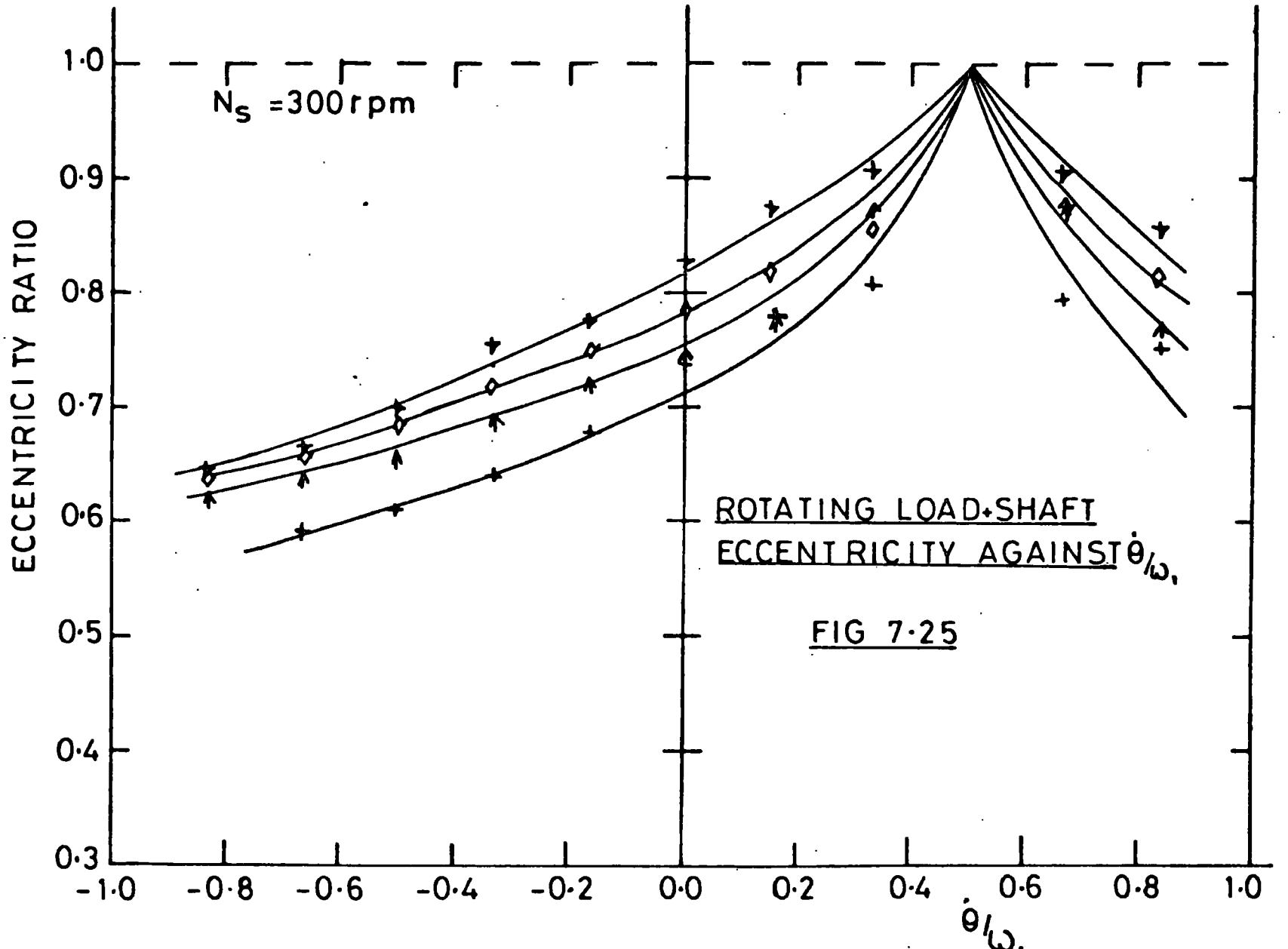

ROTATING LOAD+SHAFT ECCENTRICITY AGAINST $\dot{\theta}/\omega$.

FIG 7·25

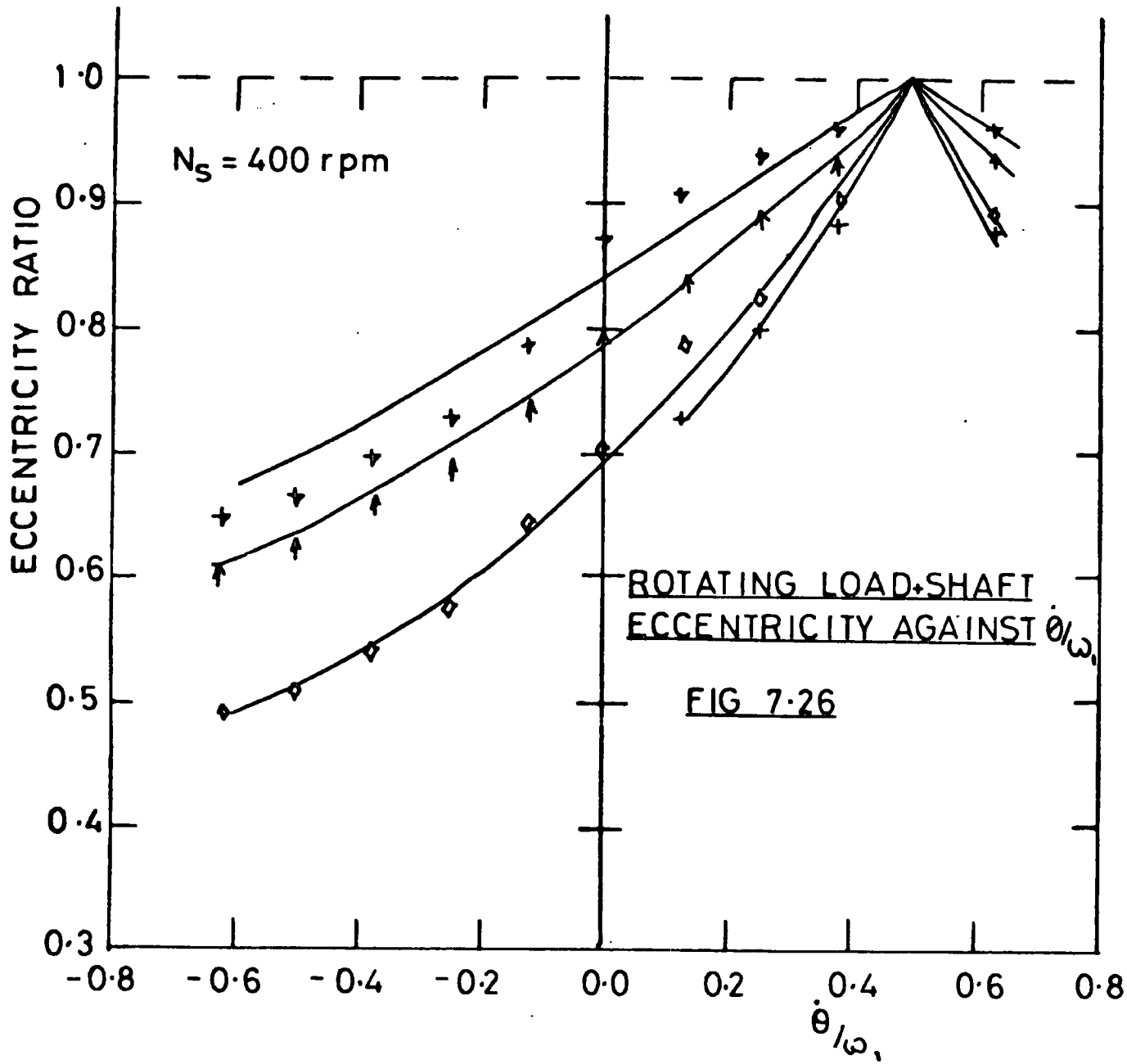
ECCENTRICITY RATIO
1·0
0·9
0·8
0·7
0·6
0·5
0·4
0·3
N_S = 400 rpm
-0·8
-0·6
-0·4
-0·2
0·0
0·2
0·4
0·6
0·8
$\dot{\theta}/\omega_s$
ROTATING LOAD+SHAFT
ECCENTRICITY AGAINST $\dot{\theta}/\omega_s$

FIG 7·26

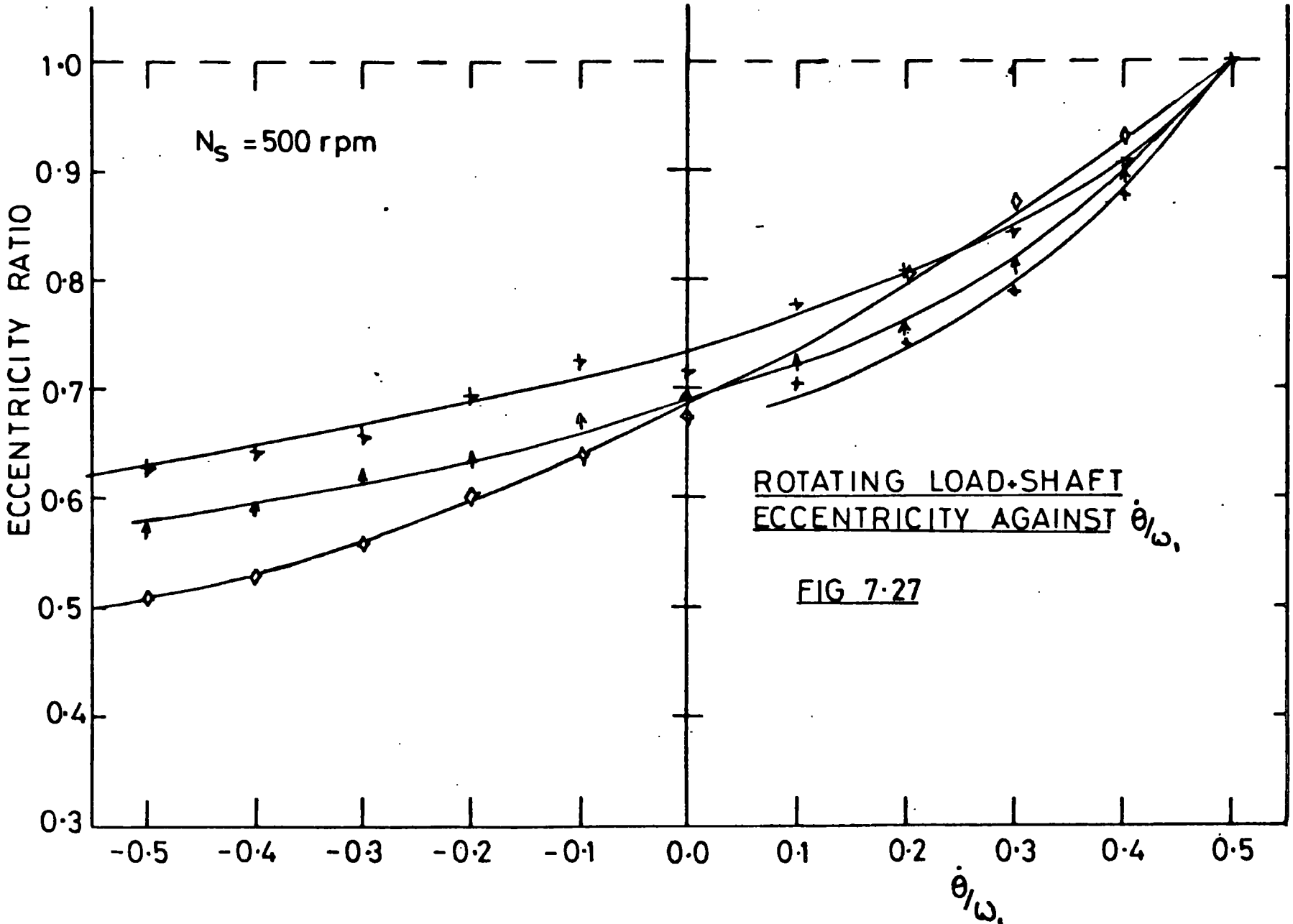

ROTATING LOAD-SHAFT ECCENTRICITY AGAINST $\dot{\theta}/\omega_s$

FIG 7·27

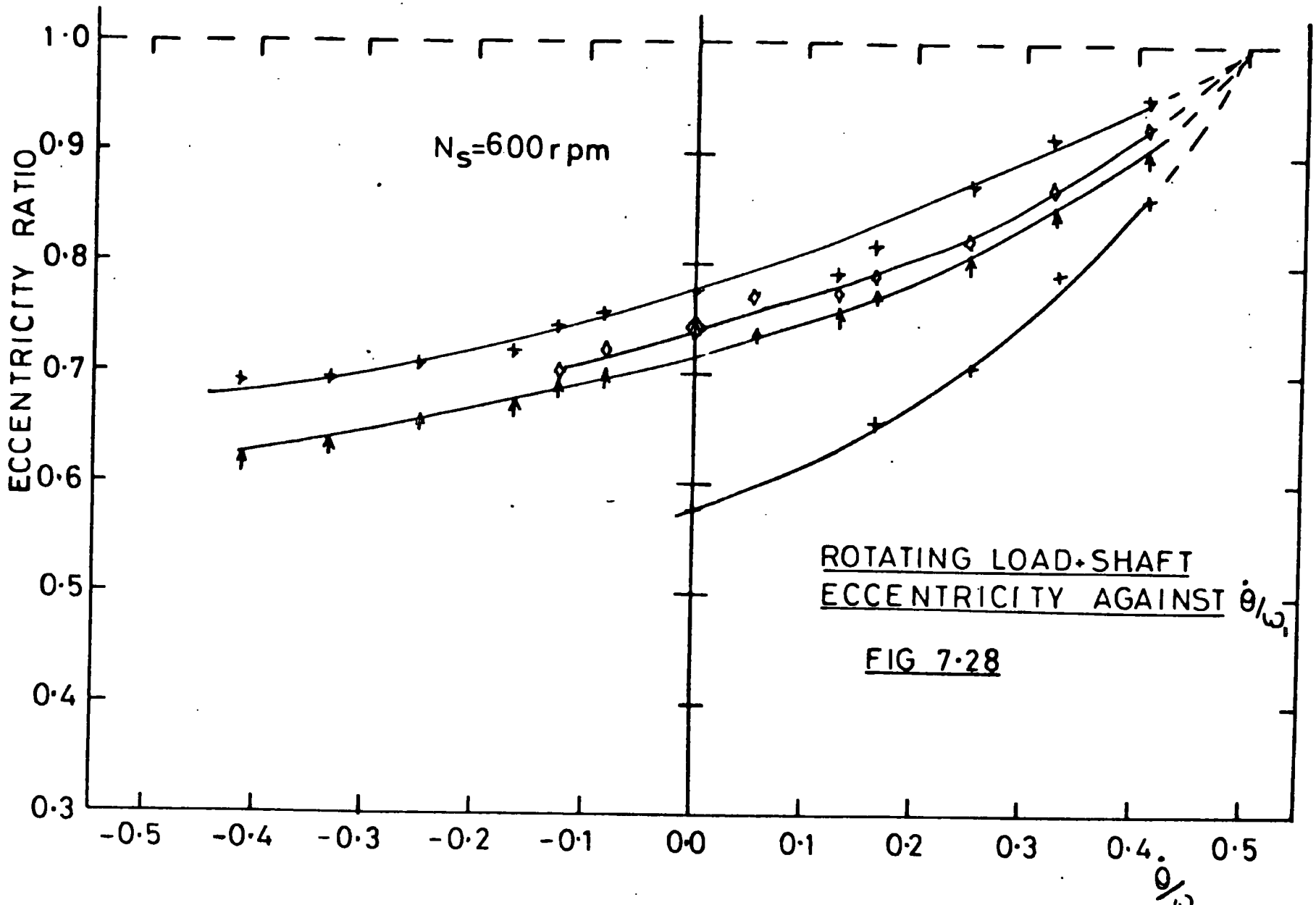

ROTATING LOAD+SHAFT ECCENTRICITY AGAINST $\dot{\theta}/\omega_1$

FIG 7·28

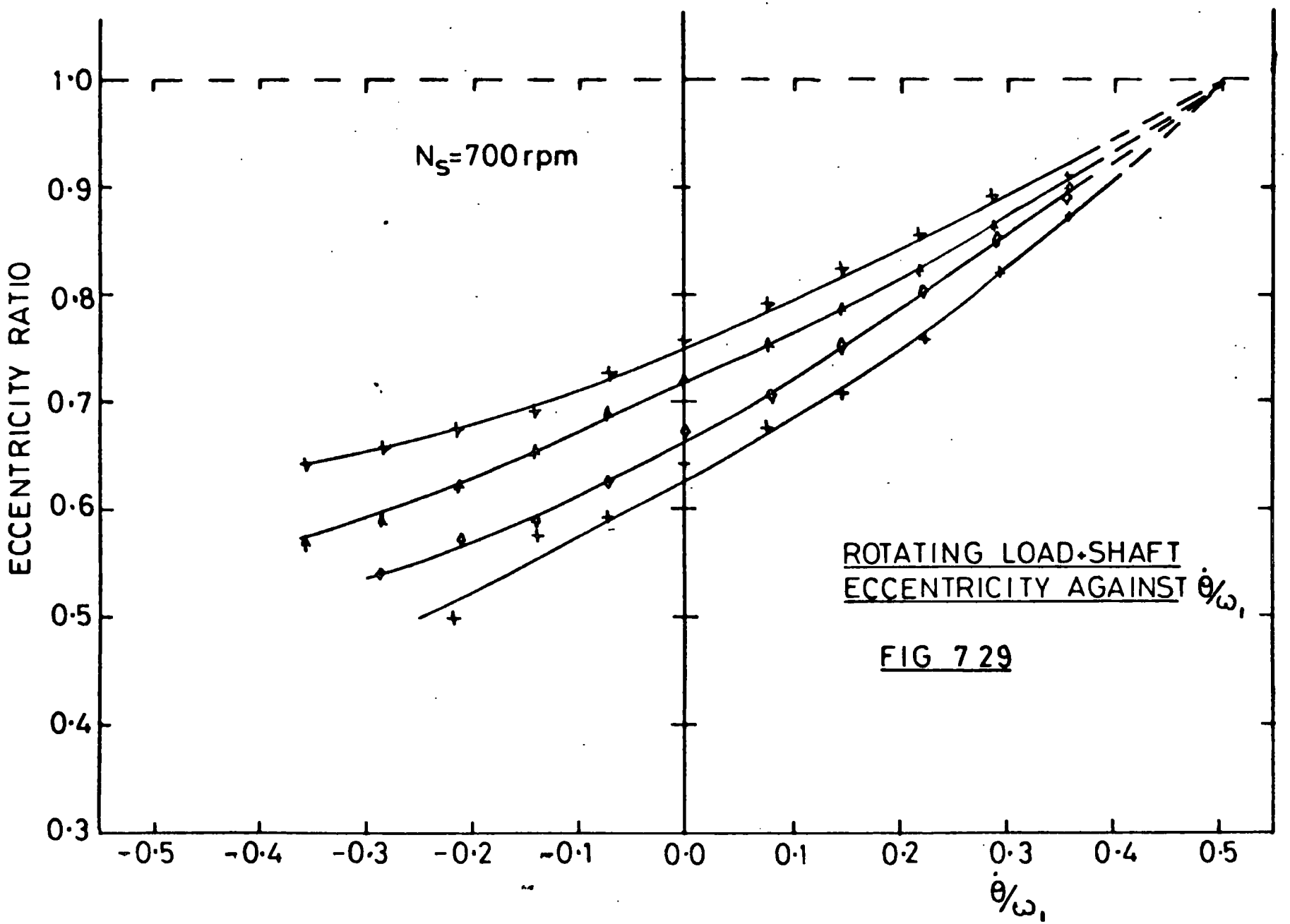

ROTATING LOAD-SHAFT
ECCENTRICITY AGAINST $\dot{\theta}/\omega_1$

FIG 7 29

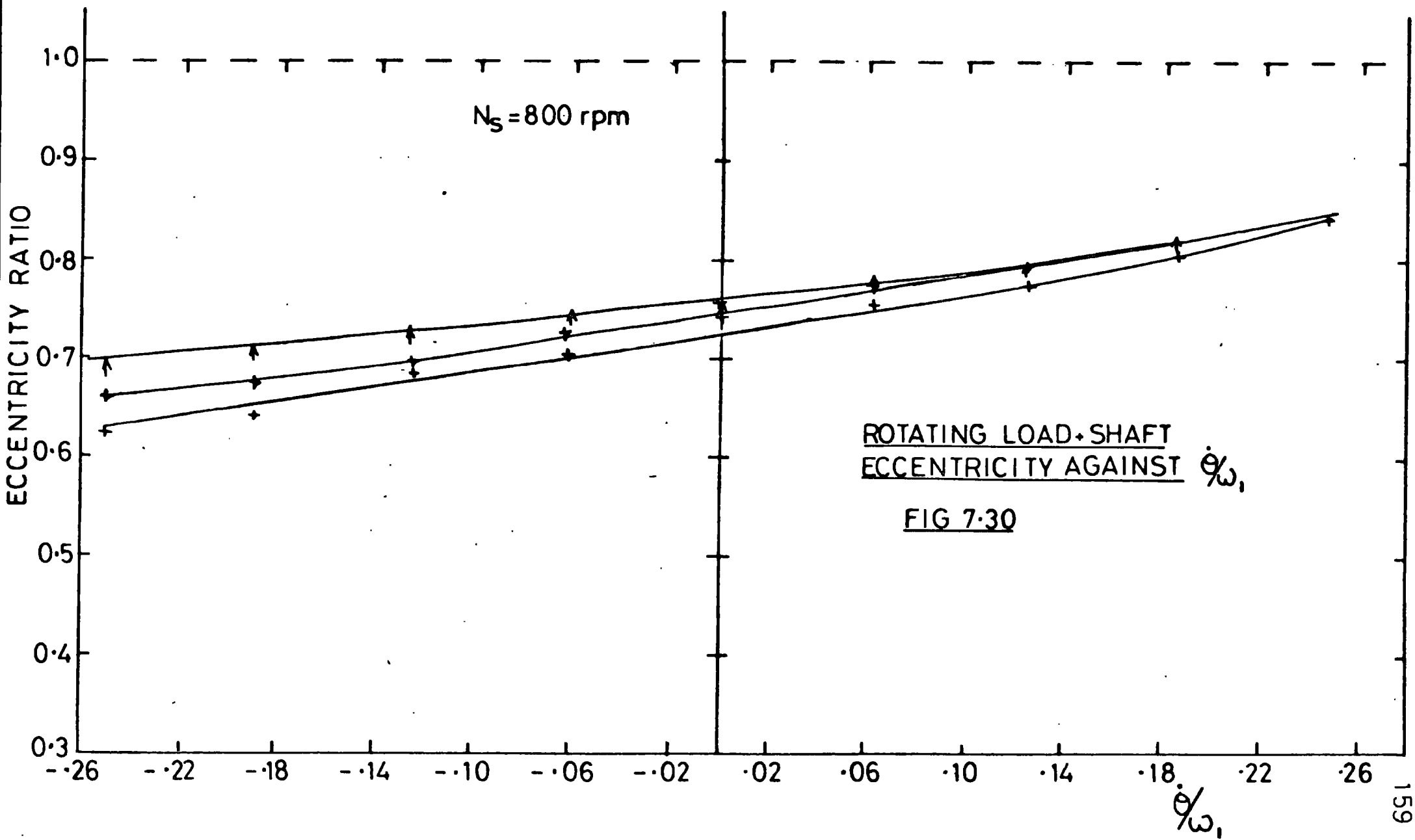

ROTATING LOAD + SHAFT
ECCENTRICITY AGAINST $\dot{\theta}/\omega_1$

FIG 7·30

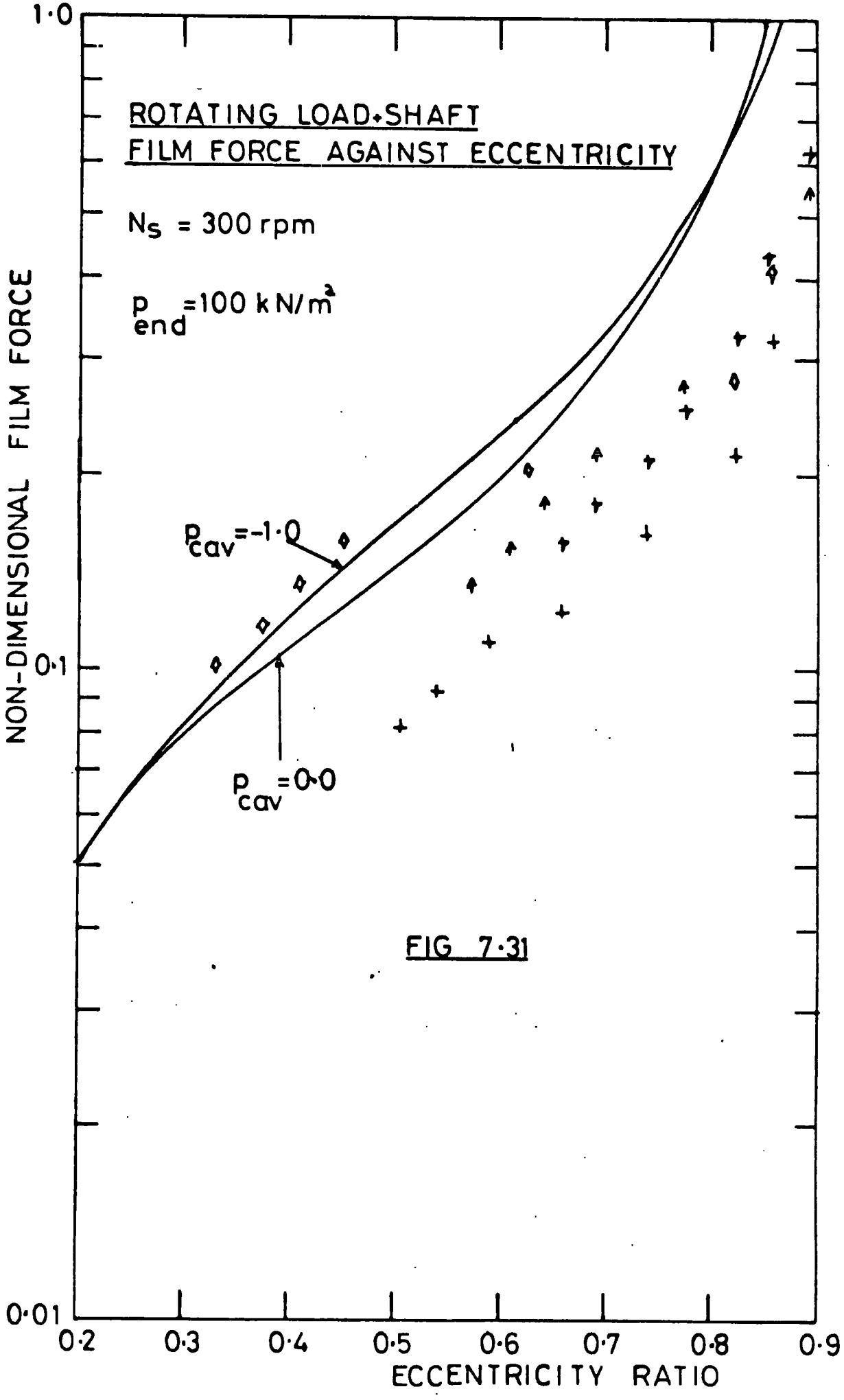
ROTATING LOAD+SHAFT
FILM FORCE AGAINST ECCENTRICITY
N_S = 300 rpm
p_{end} = 100 kN/m²
p_{cav} = -1·0
p_{cav} = 0·0
NON-DIMENSIONAL FILM FORCE
1·0
0·1
0·01
0·2
0·3
0·4
0·5
0·6
0·7
0·8
0·9
ECCENTRICITY RATIO

FIG 7·31

N_S = 300 rpm

——— p_{cav} = 0·0 p_{end} = 100 kN/m²

——·—— p_{cav} = -1·0

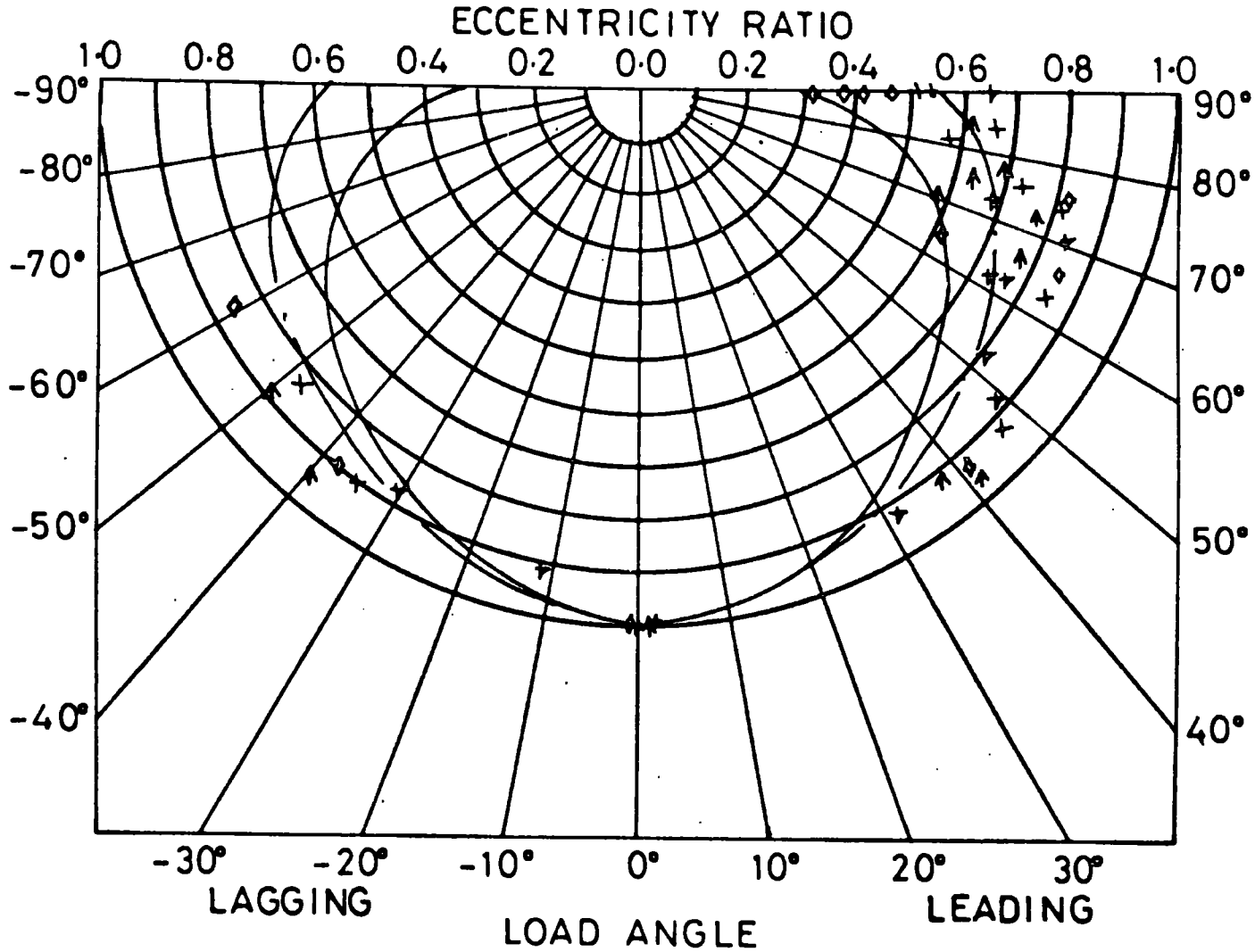

ROTATING LOAD-SHAFT
LOAD ANGLE RESULTS

FIG 7·32

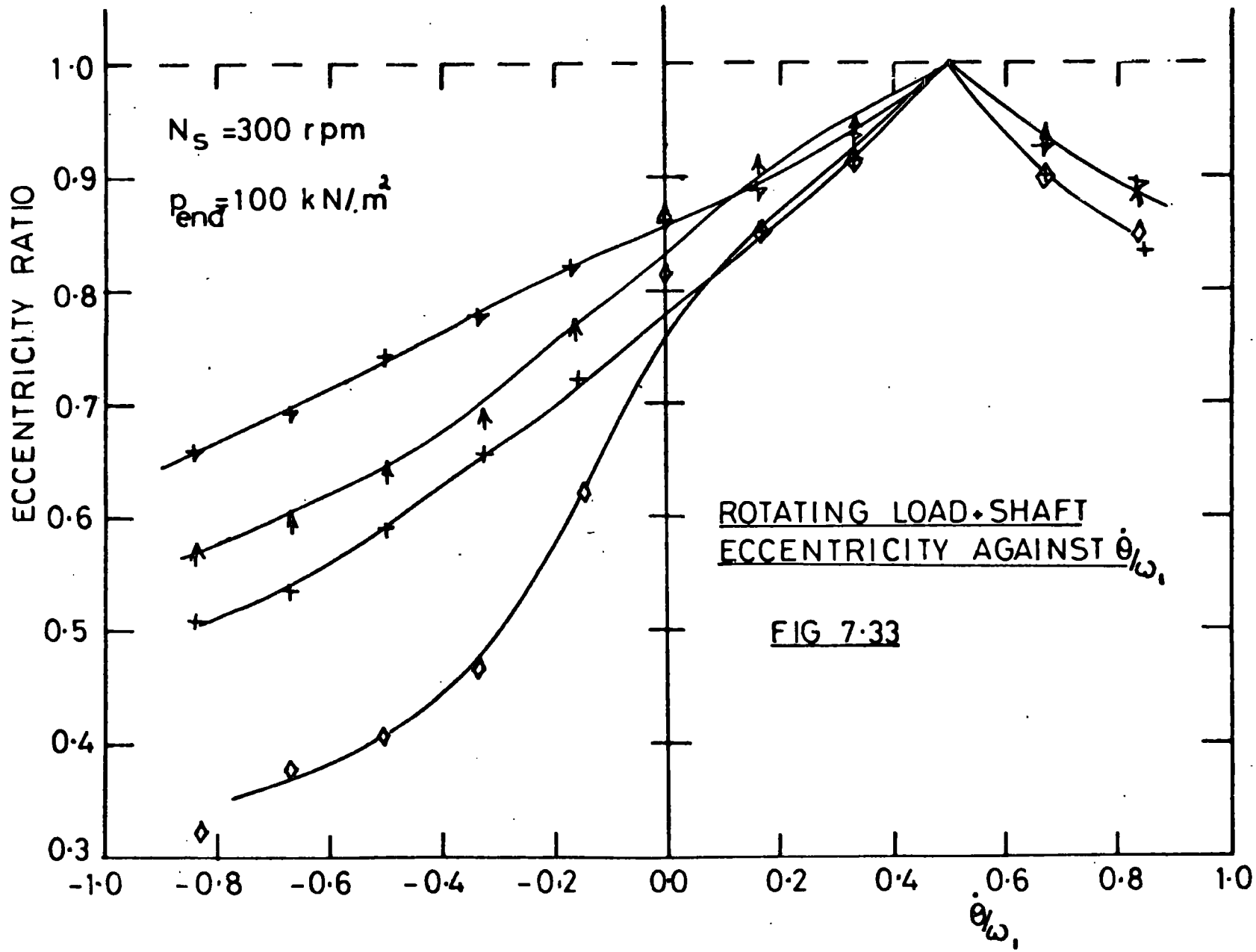
ECCENTRICITY RATIO
1·0
0·9
0·8
0·7
0·6
0·5
0·4
0·3
N_S =300 rpm
P_{end}=100 kN/m²
ROTATING LOAD+SHAFT
ECCENTRICITY AGAINST $\dot{\theta}/\omega_1$
FIG 7·33
-1·0
-0·8
-0·6
-0·4
-0·2
0·0
0·2
0·4
0·6
0·8
1·0
$\dot{\theta}/\omega_1$

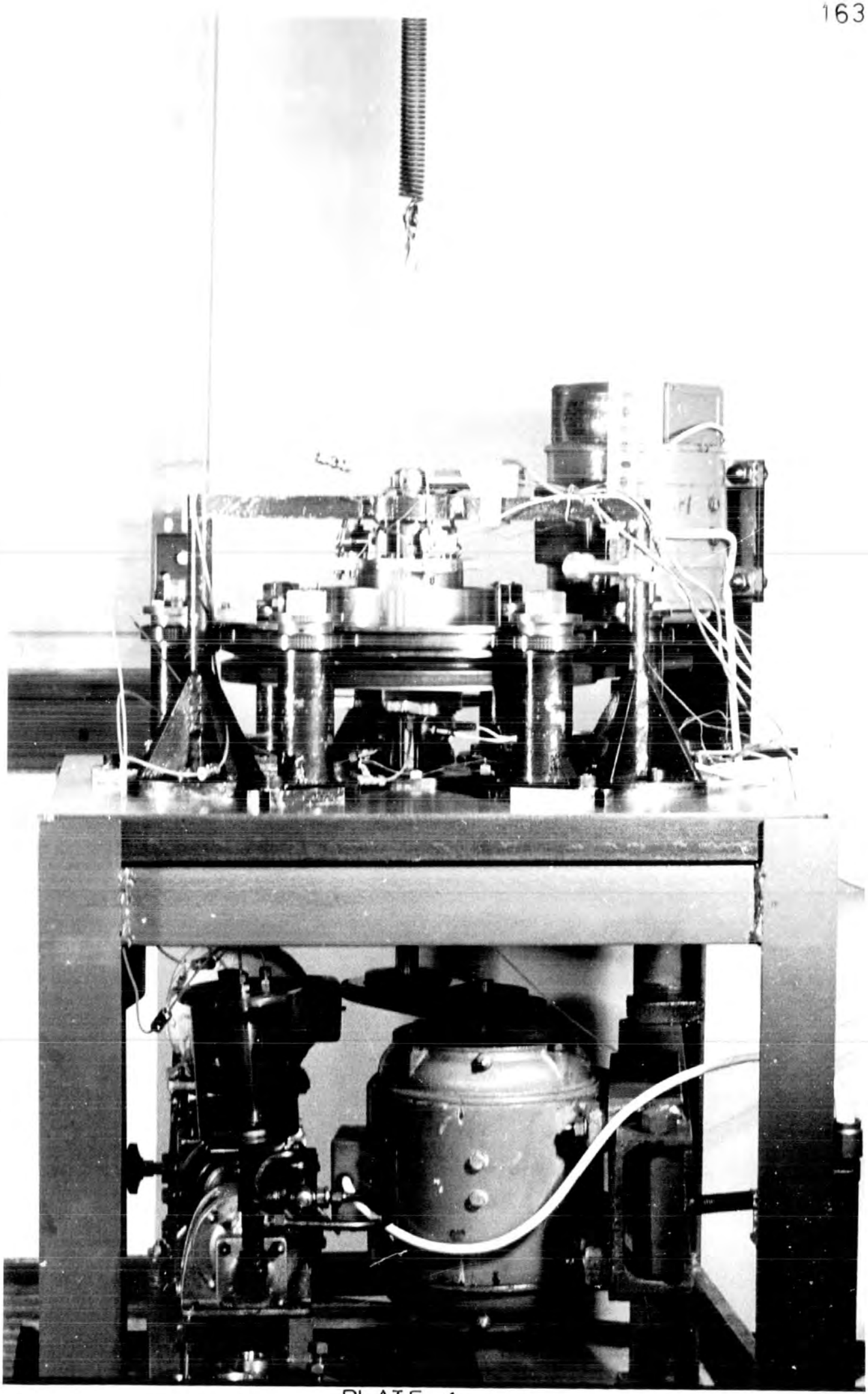

PLATE 1

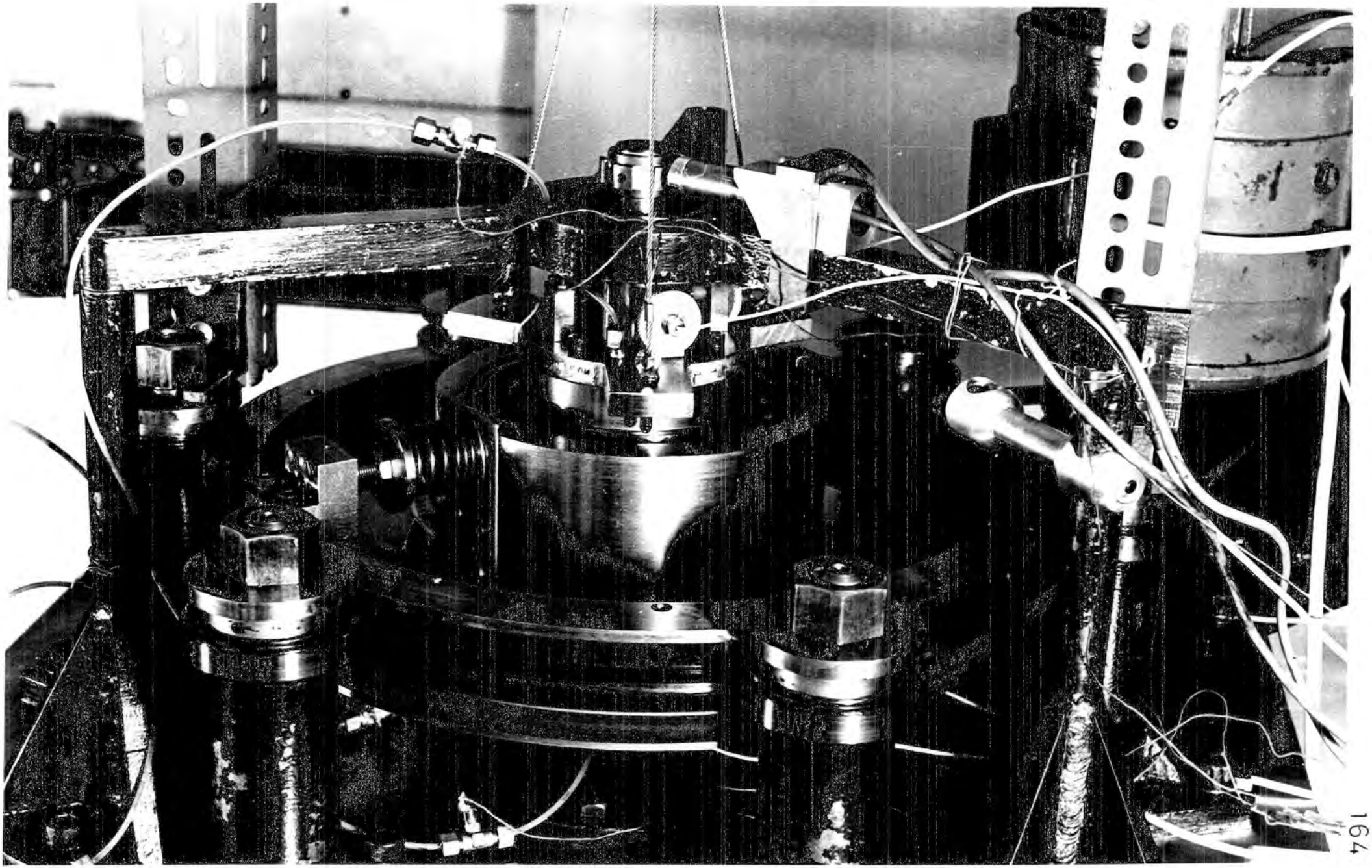

PLATE 2